NOVEL SYNTHETIC APPROACHES AND DOPING STRATEGIES FOR FACILE AND VERSATILE SYNTHESIS OF TETRAHEDRITE THERMOELECTRICS

By

Daniel Patrick Weller

A DISSERTATION

Submitted to
Michigan State University
in partial fulfillment of the requirements
for the degree of

Materials Science and Engineering — Doctor of Philosophy

2019

ABSTRACT

NOVEL SYNTHETIC APPROACHES AND DOPING STRATEGIES
FOR FACILE AND VERSATILE SYNTHESIS
OF TETRAHEDRITE THERMOELECTRICS

By

Daniel Patrick Weller

Energy consumption and utilization influence the economic prosperity, technological innovation, public health, and environmental impact of modern communities. Even with scientific advancements affording vast improvements in the efficiency with which energy is utilized, much more than half of the total energy content consumed globally is ultimately lost as rejected energy. This energy rejection manifests in the form of waste heat which is pervasive in numerous sectors of society such as transportation (e.g., warm exhaust from automobiles) and industry (e.g., hot steam from industrial cooling towers). Accordingly, if there existed a means to harvest waste heat and exploit it for a useful purpose, we could significantly ameliorate the efficiency of modern energy systems.

Thermoelectric technology may be a viable approach for generating power via waste heat recovery. These solid-state energy conversion systems comprise semiconducting materials that can transform thermal energy to electrical power by a phenomenon known as the Seebeck effect. The thermoelectric conversion efficiency is dependent on properties like the electrical conductivity, thermopower, and thermal conductivity of the materials. These properties combine to provide a figure of merit, ZT, which characterizes the thermoelectric performance of a material (i.e., higher figure of merit yields higher efficiency). Overall, solid-state energy conversion technology boasts benefits of long lifetimes and no carbon emissions.

Unfortunately, some of the best thermoelectrics to date are compounds that contain toxic elements, like lead, or low-abundance elements, like tellurium. These elemental constraints

hinder the widespread application of thermoelectric technology. In turn, there has been increased motivation to explore earth-abundant compounds for thermoelectric applications.

One such class of materials is tetrahedrites, which are extremely common minerals of copper and sulfur found all over the world. Tetrahedrites demonstrate relatively good ZT values, approximately equal to unity at a temperature of 700 K, while also consisting of low toxicity and earth-abundant elements. These ZT values rival those of other state-of-the-art thermoelectrics (e.g., lead telluride). However, one impediment to commercially employing tetrahedrite materials is the time-consuming and inconsistent synthetic method used to generate these compounds. The conventional reaction is a furnace melting procedure which requires roughly two to three weeks to fabricate a single 2 gram sample. Therefore, exploring alternative techniques for producing tetrahedrite thermoelectrics is a necessary step before these materials become feasible for large-scale applications.

This report will detail investigations of three novel approaches for synthesizing tetrahedrite materials. First, the solution-phase modified polyol process has shown success in producing nanostructured tetrahedrites with exceptionally good ZT values. Next, the mechanical alloying procedure is capable of consistently yielding high-purity tetrahedrite in about 48 hours of total reaction time. Lastly, a novel reactive spark plasma sintering method may be used to generate a broad compositional range of tetrahedrites in an expedient process requiring less than 2 hours from start to finish. The thermoelectric performance of samples fabricated by these methods is on par or better than that reported for tetrahedrites made by the traditional method. Ultimately, this work serves as a foundation for expediting tetrahedrite research and rendering these technologically important materials more amenable to commercial thermoelectric applications.

I dedicate this work to my parents, Pat and Jayne,
my grandma, Barb,
and all of my friends and family.

Without you, none of this would be possible.
I love you with all of my heart.

ACKNOWLEDGMENTS

First and foremost, I would like to thank Dr. Donald Morelli for his infinite support throughout my entire graduate school career. Ever since my first campus visit in the spring of 2014, I knew that I wanted to be a part of the Morelli group. Immediately, the groundbreaking solid-state materials science research had piqued my interest. And after seeing the camaraderie of his students and the passion with which Dr. Morelli spoke about his work, I was certain. I joined the team in January 2015 and began learning how to carry out experimental condensed matter research while also forming my professional identity. Dr. Morelli was knowledgeably capable, promptly attentive, and respectfully professional in his mentoring-style. Furthermore, I learned so much by watching him transition from a tenured research professor role to the chair of our department. Over the years, he always urged me to publish papers, attend conferences, and participate in extracurricular professional development programs. Owing to my passion for education and teaching, I participated in three graduate teaching fellowships on campus at MSU. Every time I asked for permission to work on these external projects, Dr. Morelli's humble answer would be, "If this is what you want to do, then I'm not going to stop you!" In addition to all of this massive professional support, he also demonstrated how to be an effective, patient, and understanding communicator in team-based settings. I attribute the majority of my academic accomplishments to Dr. Morelli, and I am so incredibly grateful to have had the privilege of working with him.

My doctoral committee members were instrumental in my success at MSU. Working with Dr. Wei Lai has me shown me how beneficial the synergy between modeling and empirical work can be. I learned a lot from him in thermodynamics class and our hybrid computational-empirical research collaboration, which was the basis for my idea to study paired modeling

and experimental activities in an introductory physics classroom.[1] I would like to thank Dr. Richard Lunt for helping me critically examine my data and providing insightful recommendations for future research directions. From taking his diffraction/spectroscopy class and receiving mentorship from him in the GAANN Fellowship, I learned how to respectfully supply constructive criticism and cultivate success in a learning community. In addition, Dr. Xianglin Ke was very accommodating in helping me interpret my research data from a condensed matter physics perspective. Again, I would like to thank my entire doctoral guidance committee for helping me through the process of conducting critical research and providing support throughout my journey.

I would especially like to thank Dr. Mary Anderson for the astronomically large impact that she had on my academic career. From our numerous collaborative projects, I was able to engage in scholarly science and share our results at international conferences around the world. It was an honor to spend four weeks in her lab as a visiting researcher and teach two chemistry guest lectures under her mentorship. The lessons I learned from this involvement at Hope College are still some of the most striking experiences in my odyssey to become an educator. I learned so much when mentoring two undergraduate researchers in her lab, and it seems possible that I may have learned more from them than they learned from me. Specifically, working with Andy and Grace taught me the power of patience, clear communication, and shared excitement in a scientific context. Dr. Anderson cultivated an admirable sense of community in her group with daily morning check-ins and a one of a kind sense of initiative. I am so fortunate to have been able to work with the Anderson lab, and I am looking forward to seeing where our collaboration will go next.

[1] "Investigating complementary computational and empirical activities for students learning diffusion" by D.P. Weller, K. Hinko, and V. Sawtelle in *Physics Education Research Conference Proceedings*, 2018.

I would like to acknowledge my funding sources and collaborators for enabling my research. Much of my research was supported by the National Science Foundation (NSF-CBET Award #1507789) and the U.S. Department of Education (GAANN Award P200A140215). I am grateful toward the Graduate School at MSU, PERTG of the American Association of Physics Teachers, and Gordon Research Conferences for funding my attendance at multiple conferences. Thank you to Junchao Li for our fruitful collaborations and demonstrating exceptional proficiency as a computational materials scientist. Many thanks to Cameron Holder whose wonderful transmission electron microscopy images are featured in this report. I would also like to acknowledge Drs. Ben Kopek and Jennifer Misuraca for assisting in our synthesis and characterization of tetrahedrite nanomaterials. Of course, an enormous thank you goes to Andy Ochs and Grace Kunkel for their dedication, patience, and kindness. I am humbled by the fantastic work of these collaborators.

My fellow lab members, classmates, colleagues, professors, and previous mentors provided support and inspiration throughout my graduate studies. First, Dr. Vijay Ponnambalam was a crucial resource who helped me interpret my data, gave advice on scholarship, and provided an unmatched level of expertise with lab equipment. I would also like to thank Drs. Xu Lu, Winston Carr, Jared Williams, and Spencer Waldrop for teaching me everything I know about thermoelectric research and equipment. Thanks to Corey Cooling and Spencer Mather for struggling through the thick of it and putting up with me, even when the times were hard. My professors and classmates at MSU were so helpful in my process of becoming a competent materials scientist, including Dr. Alex Zevalkink, Didier Figaro, David Smiadak, and Siddharth Rath. Furthermore, I would like to thank my colleagues from the GAANN, FAST, and SUTL fellowships. Specifically, I acknowledge Drs. Phil Duxbury, Stuart Tessmer, Rique Campa, Mark Urban-Lurain, Kendra Cheruvelil, and Caitlin Kirby. Thank you to Drs.

Matthew Vannette and Jason Pagano for training me in the art of LaTeX. And thank you to Dr. Ludovico Cademartiri, for his unbelievable ingenuity which motivated me to pursue a Ph.D. in materials science and nanomaterial research. Additionally, my involvement with Drs. Paul Irving, Katie Hinko, Vashti Sawtelle, Danny Caballero, and Daryl McPadden in the PERL lab helped me find my identity as an educator. Without your support, I would not have made it nearly this far.

My parents are my greatest role models. My mother, Jayne, has inspired me to persevere, even in the hardest of times. She is an unending reservoir of love and support. Undoubtedly, my scientific passion stems from her insight and ability to think critically from multiple perspectives. I aspire to achieve the same level of strength and knowledge that Jayne consistently demonstrates, although I know there is no one like her in the world. At the same time, my father, Pat, has granted me the social and emotional capacity to comprehend how my choices affect the community around me. My enthusiasm for public speaking and sharing knowledge with others likely originates in Pat's aptitude for uttering the truth in speech. He has a way of generating comfort and inclusivity wherever he goes. When I consider how my actions will affect others, I know that Pat's outlook will navigate me toward benevolence. To both of my parents, I am inexplicably proud to be your son.

It goes without saying that my siblings have inspired me beyond what I ever imagined was possible. I would like to thank my eldest brother, Matt, for expressing a breadth of knowledge that engages me on multitudinous levels. His intellectual adaptability and open-mindedness repeatedly motivate me to affirm my values and individuality. I am grateful toward my sister-in-law, Megan, for her altruistic compassion and patience. Her timely check-ins remind me to take care of myself and stay healthy. With regards to my brother, Nathan, it is especially laborious to label with my limited lexicon how much of an impact he

has had. As I transitioned through the various chapters of my life, he was always there to guide me. I would like to thank my sister, Rachel, for helping me feel youthful and making me laugh endlessly, especially throughout the writing of this dissertation. She is the magnet that holds our unit together with frequent check-ins for family bonding days and holiday plans. Finally, my cousin, Christian, is one of the few people that truly understands and empathizes with my research endeavors. It is so refreshing to have him as a companion who is always down for talking about science, hackey sacking, or undertaking some crazy project at Pine Lake. In my ruminations of how I became so lucky, privileged, and blessed to be in a position like this, you all were the consistent determinant.

I would also like to thank my other family members for supporting me in my struggles. My grandma, Barb, has given me so much. I am so grateful for her actions and her identity. She is the strongest woman I have ever met, and without her, I wouldn't be who I am today. Starting with simple games like Uno and graduating to more complex games like Cribbage or Rummy, Barb unfailingly imprinted a sense of determination and competitive sportsmanship in me, which I try to propagate through every aspect of my life. I am so proud to be your grandson, Barb. I would also like to thank my uncle, Steve, for giving me advice on physical health and my career. To my uncles, aunts, and cousins, I vow to continue trying to bring out the best in our community, just as you have for me.

I am unbelievably thankful for my friends, who have supported me in this academic goal, which is unlike anything I have undertaken before. To name a few, the Linden good ol' boys, the SVSU crew, the B6 squad, and the Dank Hugs fam have been so supportive. Briefly, I would also like to acknowledge running, DotA, and EDM for helping me get through the hard times. In particular, I would like to thank Eric Straley, who ventured through graduate school with me from beginning to end and helped me align my moral compass. Unfortunately,

I am unable to list everyone by name, but they know who they are. Let it be known, every single one of you is so important to me, and I would've been cashed out a long time ago, were it not for you.

Lastly, I would like to thank scientists and our society for valuing the pursuit of knowledge through rational thought and empirical determination. Science is a slow-moving glacier. And without the incessant dedication of scientists, educators, and students before us, our lives would be far more difficult than they are today. For many years, I have studied the systematic optimization of material properties that seem to be intractably contraindicated. As thermoelectric researchers, we strive to create materials that are as electrically conductive as possible, while also conducting as little heat as possible. To avoid being esoteric, it will suffice to say that this is a seemingly insurmountable task because these properties are linked in an absolutely proportional fashion. However, throughout my academic career, I have found that this conundrum is not truly intractable. In fact, the clash of oppositely intertwined forces can be exploited to synthesize technology that effectively and forthrightly pushes humanity in a positive direction. The contradictory nature of this existence is exactly what gives it such beauty and magnificence.

To close, I would like to provide a materials science metaphor that relates my actions to the immense support system of colleagues, mentors, family, and friends that influences them. In tetrahedrite materials, one may think that the individual atoms of copper, antimony, and sulfur are what enable their fascinating physical phenomena. Such elements have been studied for centuries, and in turn, the behaviors of these microscopic building blocks are well-defined. But when elements come together in distinct crystalline systems, they act much differently. There is a symbiosis between the various components that make up the interwoven, complicated system. The atoms in a crystal are dynamically bound together

with a deep underlying substructure that pushes and pulls on every other one in the system. They influence each other mechanically and electronically, magnetically and radiatively, and in many more ways beyond the scope of our comprehension. Eventually, long-range ordering effects arise, and it seems that the behavior of one atom can have far-reaching and unfathomable consequences on the macroscopic whole. This existence is an enormously complex crystalline system. And while we are the individual atoms that make up the crystal, we are also so much more than that. Thank you to everyone that has helped me reach this point. It is a true gift.

TABLE OF CONTENTS

LIST OF TABLES

LIST OF FIGURES

Chapter 1

Introduction

Improving the efficiency of current global energy systems is paramount to achieving a sustainable harmony between human civilization and the environment. As it stands today, a massive amount of energy is being wasted, and this chapter will provide an overview of motivations for utilizing thermoelectric (TE) technology for power generation applications via waste heat recovery. An in-depth background of TE effects, charge transport, and heat propagation in materials will be given to better understand the physical phenomenon of thermoelectricity. Furthermore, over five or so decades, numerous engineering techniques have proven to be successful in improving TE performance. After discussing these tactics, some state-of-the-art TE materials will be reviewed.

1.1 Energy Efficiency, Waste Heat, and Thermoelectric Technology

Energy drives technological innovation and economic prosperity in modern societies, and the manner in which energy is consumed and utilized affects a society's environmental impact and well-being. Recently, global concerns about humanity's ecological effects have surfaced. As populations grow, economic demands increase, and societies must produce more energy to meet these demands. Fossil fuels, like oil and natural gas, are the primary energy carriers

for which the world's energy needs are met. However, as increasingly greater amounts of nonrenewable fossil fuels are consumed, a consequential rise in carbon emissions has been observed.[1] These greenhouse gas emissions, which have steadily been rising since the birth of modern industry in the 1800s, are believed to be the origin global climate change.[2] In turn, improving the efficiency with which we utilize our limited resources on this planet is paramount to advancing our species in a sustainable manner.

In the process of generating electricity and other forms of usable energy, primary energy carriers undergo significant transformations that inevitably release a portion of their energy content to the environment. Part of this energy loss is a natural and inexorable consequence of the second law of thermodynamics.[3] In other words, the entropy of the universe is always increasing because no physical process can ever be truly reversible. The most common type of this energy rejection comes in the form of waste heat, where some of the total amount consumed is converted to heat that dissipates into the surrounding environment. For instance, machines that utilize hydrocarbon fuels to do mechanical work (i.e., automobiles) or produce electrical power (i.e., generators) also create heat as a byproduct. Usually, this waste heat is given off to the surroundings and never exploited for a useful purpose.

The amount of useful energy extracted from primary energy carriers is astoundingly small compared to the initial total. Figure 1.1 displays global energy flow in 2012 as reported by Forman et al.[4] On the global scale, an estimated 72% of the energy consumed from primary energy sources (e.g., fossil fuels, nuclear, and renewables) is ultimately lost as rejected energy.[4] Of that selection, 52% consisted of exhausts or effluents while 20% was attributed to other losses like friction and electrical resistance. Additionally, sources of waste heat were identified at low (< 100 °C), medium (100–299 °C), and high (≥ 300 °C) temperatures with their respective distributions approximated as 63%, 16%, and 21%.

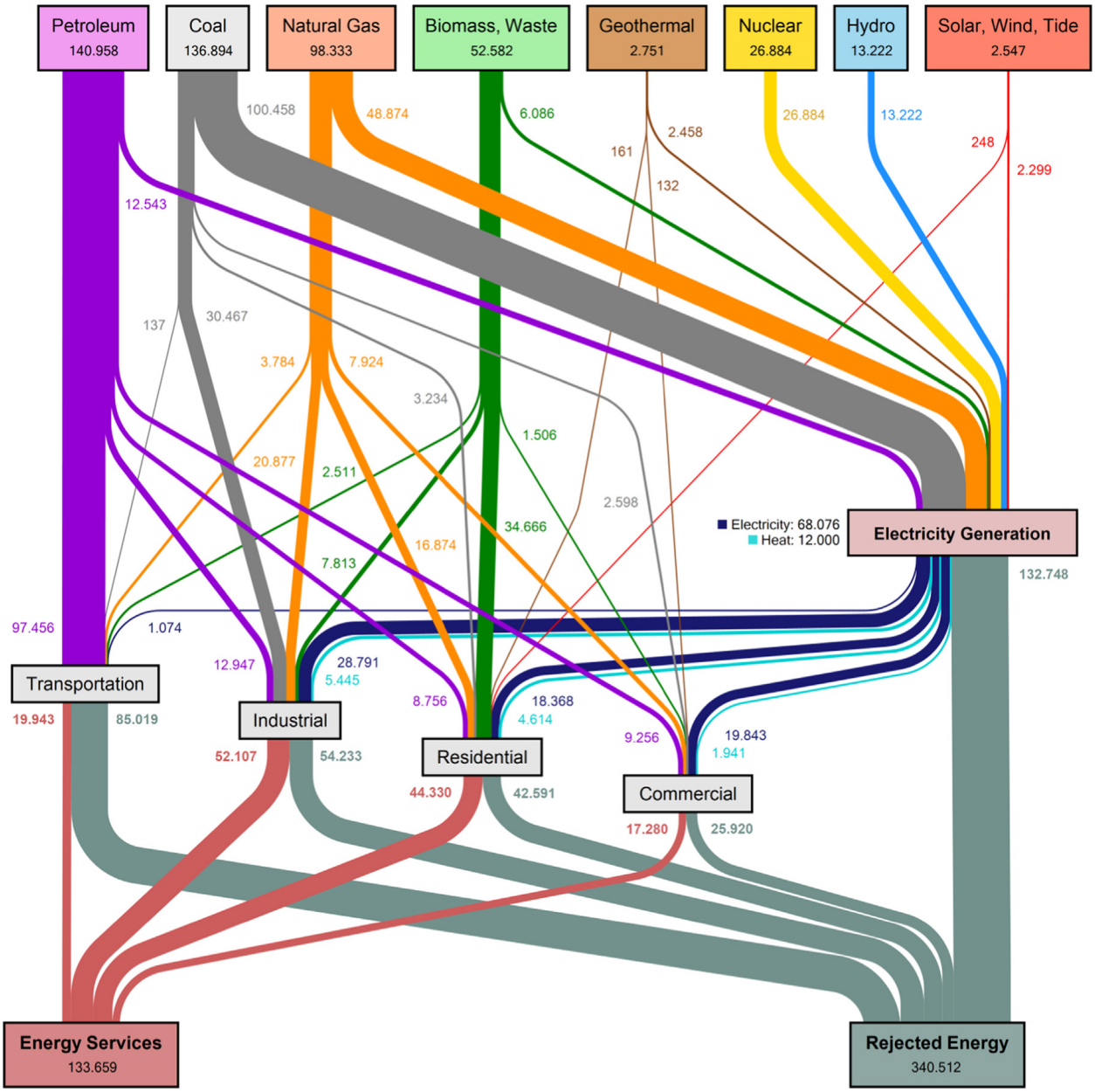

Figure 1.1: Flow diagram from Forman et al.[4] In 2012, approximately 72% of the total energy consumed from primary energy carriers was ultimately lost as rejected energy. Units are in petajoules (1 PJ = 10^{15} J), and the initial total energy from primary sources was estimated to be 474.171 PJ.

Other groups have made similar estimates as Forman and coworkers. For instance, Cullen and Allwood claim that less than 12% of primary energy sources were utilized for end-use (i.e., motion or electricity).[5] They also identified that the lowest ratio of energy produced to carbon emitted overwhelmingly came from coal and oil.[6] Industrialized and developed nations are some of the largest players in terms of this energy crisis. The United States alone consumed about 97.5 quadrillion BTU (1 quad $\approx 1.1 \times 10^{18}$ J) in 2016.[7] By these estimates, the U.S. accounted for 17% of the world's total annual consumption, while only constituting less than 5% of the global population.[8] Among all the countries in the world, this is by far the highest ratio of energy consumed to population size. In the same year, Lawrence Livermore National Laboratory estimated a net loss of more than 68% of the total energy consumed by the U.S.[9] Waste heat contributes heavily to the world's detrimental energy inefficiency conundrum. Therefore, it is widely agreed that significant improvements could be made to global energy infrastructure, policies, and practices.

Waste heat recovery could be a viable short-term solution for improving efficiency as renewable energy technology develops. Consequently, devices made from TE materials have garnered significant attention in the past two decades, owing to their ability to harvest waste heat and convert it to usable electric power.[10, 11] Accordingly, these materials can be used for solid-state power generation applications via waste heat recovery. Given the pervasive nature of waste heat, TE devices may be employed in numerous sectors of society. TE generators commonly find applications in automotive [12, 13], industrial [14, 15], and aerospace [16] settings. It is no coincidence that TEs show the most promise in sectors that are either the largest producers of waste heat (i.e., transportation and industry) or situations where performance is greatly valued over cost (i.e., space technology). Moreover, solid-state energy conversion boasts advantages like environmental friendliness (no carbon emissions),

no moving parts (less maintenance), long life times, scalability, and simple integration with current energy systems.[17] However, while TEs hold promise for alleviating constraints on modern energy networks, these materials are currently limited by relatively low efficiencies compared to other power generation technologies.

1.2 Fundamental Physics of Semiconductors

The theory of semiconducting materials is important for understanding the physical phenomena which govern TE effects. In the following subsections, the underlying principles of semiconductors, which manifest in macroscopic material properties like electrical and thermal conductivity, will be reviewed. Such a conception involves considering the various quantum mechanical subunits of crystalline systems such as atoms, electrons, and phonons. Beginning with the rules which dictate the behavior of these foundational building blocks of our universe, this section will attempt to disentangle the electronic and lattice vibrational physics of semiconductors to comprehend the spellbinding nature of thermoelectricity.

1.2.1 Crystallography and Crystal Structure

The majority of solid materials in our everyday lives are crystalline systems. This means that when atoms bond to form these bulk materials, they adopt positions in a well-ordered network of similar particles known as a crystal lattice. The crystal lattice demonstrates a repeating periodic structure which enables for mathematical simplifications based on symmetry. The unit cell is the term used to describe the smallest set of atoms that are representative of the overall crystal structure, and the lattice parameter (a) defines the distance between atoms along one axis of the unit cell. The simplest type of three dimensional crystal lattice is a

cubic system, where all atoms reside at sites perpendicular to the other atoms with the same spacing in the three Cartesian dimensions. Deviations from cubic behavior arise in a variety of other crystallographic systems mostly through distortions in either the lattice parameters or angles of a structure.

The most classical semiconducting material, silicon (Si), will serve as a foundation for explaining the science of crystals. Figure 1.2a depicts the unit cell for Si. It is a diamond cubic system that contains four atoms per unit cell. Notice that different slices of the structure can contain planes of atoms which exist throughout the whole structure. Atomic lattice planes are denoted by a set of numbers known as the Miller indices ($hk\ell$). Furthermore, the unit cell can be reduced to a primitive unit cell (Figure 1.2), which simplifies the structure by containing only one atom.

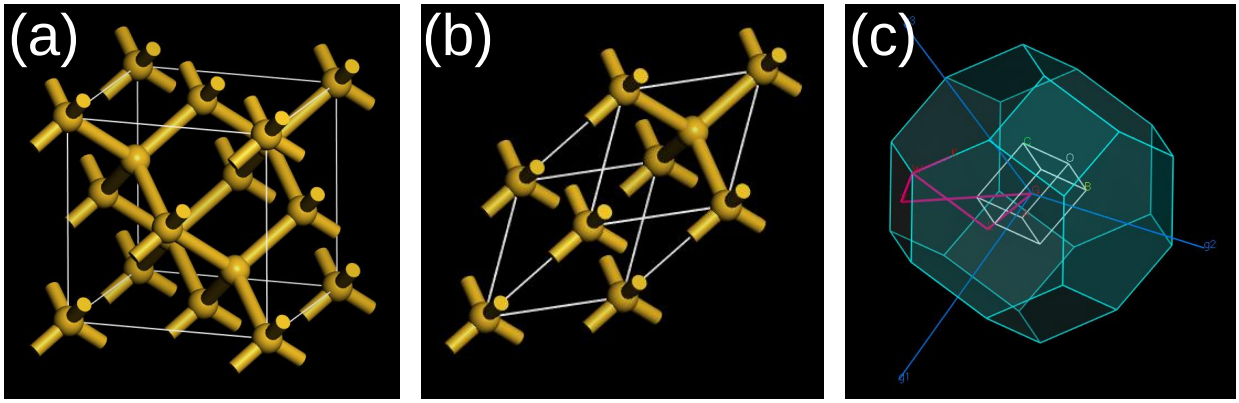

Figure 1.2: Depictions of the silicon crystallographic (a) unit cell, (b) primitive unit cell, and (c) Wigner-Seitz primitive cell modeled in Materials Studio.

While Figure 1.2a and 1.2b display the crystal lattice in real space, which is based on translational positions in space, Figure 1.2c displays the reciprocal lattice in momentum space (i.e., reciprocal space or k-space). This primitive cell in reciprocal space is known as the Wigner-Seitz cell, or the Brillouin zone, and much information can be gained regarding

the energetics of a crystalline system by considering its structure in k-space. For instance, the conduction of electricity or the diffraction of X-rays in crystals are effects that are easier to consider from a reciprocal space perspective. This is a difficult concept to fathom, but the representation will suffice for our discussion of material properties in semiconductors.

1.2.2 Charge Transport

The conduction of electricity in bulk crystalline systems relies on the transport of electrically charged quantum mechanical particles, like electrons. In quantum mechanics, the state of a particle is described by the mathematical wavefunction (Ψ), which is dependent on position (x) and time (t).[18] By applying the Hamiltonian ($\hat{H}$) operator to the wavefunction ($\hat{H}\Psi = i\hbar\frac{\partial}{\partial t}\Psi$), one may determine how the system energy evolves over time. The relation shown in Equation 1.1 (i.e., the time dependent Schrödinger equation) describes the state of a quantum mechanical system.

$$\frac{-\hbar^2}{2m}\frac{\partial^2\Psi(x,t)}{\partial x^2} + U(x)\Psi(x,t) = i\hbar\frac{\partial\Psi(x,t)}{\partial t} \tag{1.1}$$

In Equation 1.1, $\hbar$ is the reduced Planck constant ($^h/_{2\pi}$), m is the mass of the object, and i is the imaginary unit. Furthermore, the first and second terms describe the kinetic and potential energies, respectively. By separating the spatial and temporal components of this equation, one obtains the time independent Schrödinger equation, shown in Equation 1.2.

$$\frac{-\hbar^2}{2m}\frac{\partial^2\psi(x)}{\partial x^2} + U(x)\psi(x) = E\psi(x) \tag{1.2}$$

In the above, energy eigenvalues (E) are obtained which describe the discrete energy states

that arise in quantum mechanical systems. Since thermoelectricity involves the transport of charge through a material, we will consider electrons in a bulk crystal. In this case, the system's potential energy is described by the coulomb interaction between the negatively charged electron and the electric field from positively charged nuclei that make up the crystal lattice (i.e., $U(x) = V_c(x)$, where V_c is the Coulombic potential energy). Given the symmetry of the lattice, the electron wavefunction is defined by the Bloch function, shown in Equation 1.3.[19]

$$\psi(x) = u(x)e^{ikx} \tag{1.3}$$

Here, k is the wave number ($k = \frac{2\pi}{\lambda}$) and $u(x)$ is a periodic function that exhibits the same periodicity as the crystal lattice. For a quantum mechanical wave-particle with mass m and velocity v, an associated wavelength ($\lambda = \frac{h}{mv}$) is determined according to the de Broglie relation. It follows that Euler's formula, as shown in Equation 1.4, is a useful identity for manipulating Equation 1.3.

$$e^{ix} = \cos x + i \sin x \tag{1.4}$$

By applying the Bloch function (Equation 1.3) to the time independent Schrödinger equation, one is able to obtain multiple solutions for the allowed energy eigenstates of an electron in a crystal. When solving the differential equation for a nearly-free electron gas with values of $k = \frac{n\pi}{a}$ (for any integer $\pm n$, excluding 0), we obtain discontinuities in the energy solution. Accordingly, gaps exist in the electron's energy-momentum dispersion relation. By exploiting symmetry in the lattice, one may reduce all the possible solutions to a set of degenerate outputs which are each satisfied by k values within the first Brillouin zone ($\frac{-\pi}{a} \leq k \leq \frac{+\pi}{a}$), where a is the lattice parameter of the crystal. This reduced band scheme is displayed in Figure 1.3a. Overall, the electronic band structure describes allowed and

forbidden energy states for charge carriers in a crystalline material.

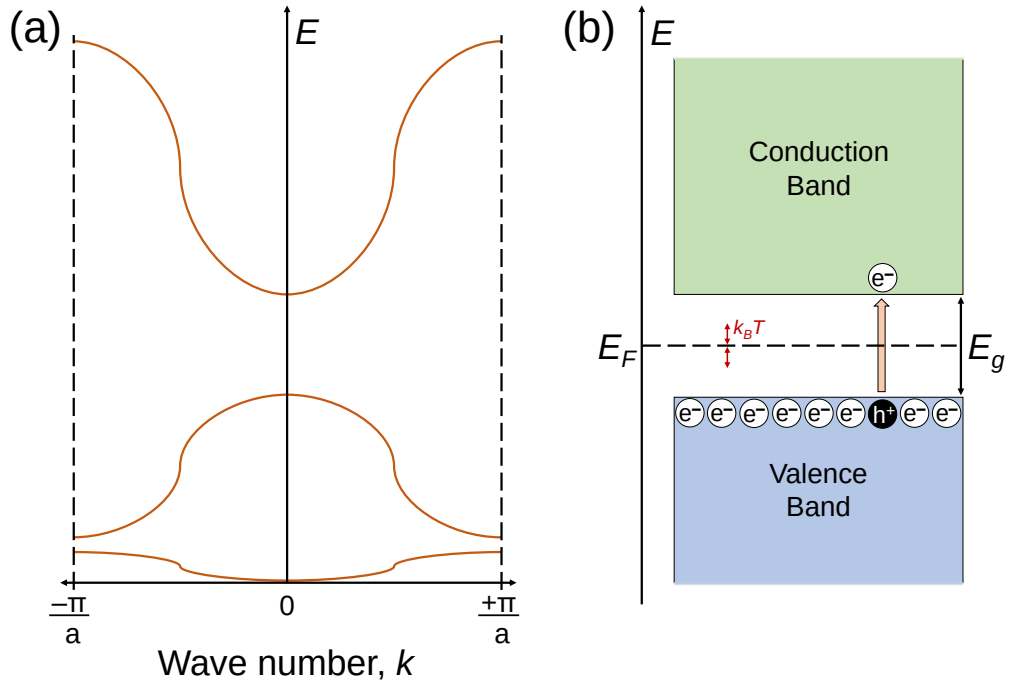

Figure 1.3: Electronic band structure diagrams for a (a) one dimensional solid and (b) three dimensional solid. Diagrams are generalized and not drawn to scale. In (a), E is the energy, k is the wavenumber, and $k = \pm\pi/a$ represents the boundary of the first Brillouin zone. In (b), E_F is the Fermi level, E_g is the band gap energy, and k_BT is a measure of the system's thermal energy. Electrons fill electronic states up E_F, and if enough thermal energy is provided to the system, an electron will be excited into the empty conduction band leaving behind a positively charged hole.

While Figure 1.3a illustrates electronic band representations for a one dimensional solid, Figure 1.3b displays the generalized band structure diagram for a bulk three dimensional material. When bulk amounts of atoms ($N_A = 10^{23}$) form a crystalline solid, the slightly differing energy levels smear together into full electronic energy bands. Electrons populate lower energy levels such that the total system energy is reduced, and at absolute zero temperature ($T = 0$ K), they will be distributed up to a defined energy known as the Fermi level (E_F). In bulk solids, molecular bonding orbitals comprise the lower energy electronic states (i.e., the valence band). Conversely, antibonding orbitals make up the levels at greater

energy (i.e., the conduction band) where electrons do not occupy the energy states. According to molecular orbital theory, the top of the valence band is termed the highest occupied molecular orbital (HOMO) and the bottom of the conduction band is defined as the lowest unoccupied molecular orbital (LUMO). The band gap (E_g) describes the energy difference between the HOMO and LUMO levels.

A material with E_F in the middle of E_g, such as the material represented in Figure 1.3b, is known as an intrinsic semiconductor. Semiconducting compounds are a unique class of electronic materials which have uniquely tunable properties owing mostly to their electronic band structure. Electrons are particles with half-integer spin values, also known as fermions, which distribute in k-space according to Fermi-Dirac statistics. When provided with energy input that exceeds E_g, an electron will be ejected from the valence band into the conduction band, leaving behind a positively charged hole. This energy input commonly comes from thermal excitation with energy k_BT, where k_B is the Boltzmann constant and T is temperature. The ratio of $\frac{E_F}{k_BT}$ is termed the reduced Fermi energy (η_F), and it determines the chemical potential of the system. This quantity effectively provides information for how carriers are excited across the gap due to thermal energy input. The excited electron-hole pair is known as an exciton, and this phenomenon is commonly exploited in transistor and solar cell applications. Under an applied field, the excited electron can translate through k-space to different energy levels and thereby conduct electricity through the material. The converse is true for the hole as well; it can move through the band to transport charge just as an electron does.

This astonishing phenomenon demonstrates material characteristics somewhere between an insulator, where no conduction of charge occurs, and a metal, where electrons are free and the carrier concentration is on the order of the number of atoms in the crystal (10^{23} cm^{-3}).

Figure 1.4 displays band diagrams for electrically insulating, semiconducting, and metallic materials. Notice that the insulator has a very large band gap (roughly $E_g \geq 5$ eV), for which excitation of electrons requires significant energy input. On the other hand, in metallic compounds, the conduction and valence bands overlap and E_F lies within the overlapping region such that infinitely many free states are available for carriers to conduct electricity. Generally, band gaps for semiconducting compounds are somewhere between 1 and 5 eV, usually giving them carrier concentrations of about 10^{16} to 10^{22} cm^3.

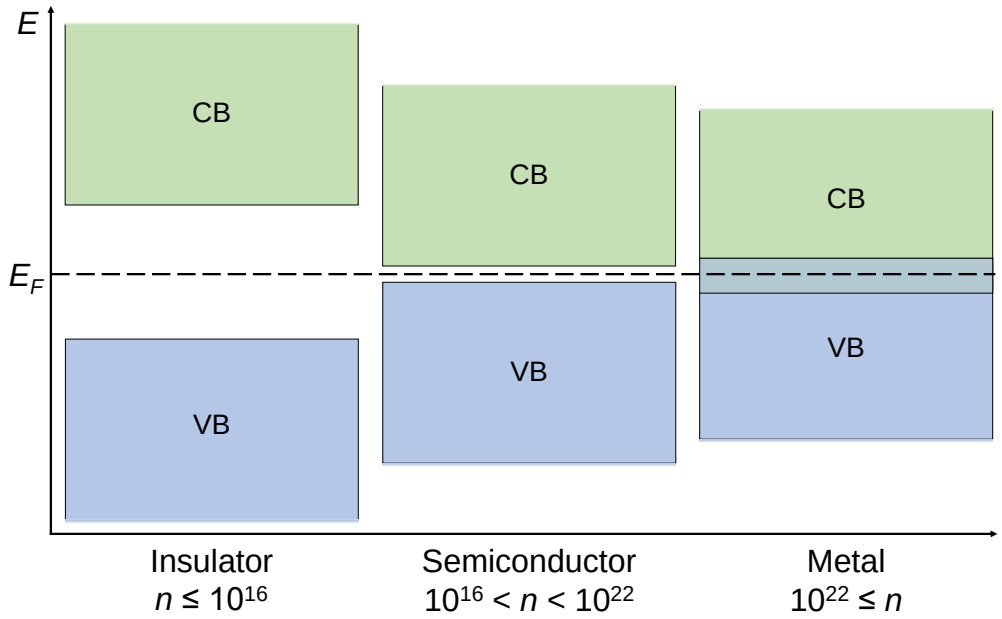

Figure 1.4: Generalized electronic band structure diagrams for three different classes of electrical materials. CB stands for conduction band, VB stands for valence band, E_F is the Fermi level, E_g is the band gap energy, and n is the charge carrier concentration. Insulators are classified by large band gaps and low carrier concentrations, whereas metals have E_F located in the band such that many carriers contribute to conduction.

The band gap is effectively a measure of how easily electrons are liberated for conduction in a material. In an intrinsic semiconductor, the concentration of carriers (n_i) that contribute to charge transport is dependent on T, E_g, and the effective mass (m^*) of charge carriers

according to Equation 1.5.[20]

$$n_i = 2\left(\frac{2\pi m^* k_B T}{h^2}\right)^{3/2} \exp(\eta_F) \tag{1.5}$$

In the above equation, the entire term preceding the exponential argument is called the effective density of states, and it describes the number of available energy states to which carriers may adopt within a given region of k-space. In semiconductors, a technique known as doping is used to modulate a materials electronic properties by introducing impurities into the lattice. These impurities act as donors or acceptors of electrons which effectively raise or lower E_F. By shifting E_F to higher energy via addition of donor impurities, the donated electrons can enter the conduction band with very little energy. When electrons outnumber holes, the material is considered an n-type (i.e., negative) semiconductor. Oppositely, incorporating acceptor ions engenders p-type (i.e., positive) conductivity in a semiconductor. Generally, these materials are known as extrinsic semiconductors. When a semiconductor is doped heavily enough, it can act like a "dirty" metal (i.e., a degenerate semiconductor) which has conductivity like other metallic compounds. The carrier concentration (n) for a metal or heavily doped (i.e., degenerate) semiconductor is approximated by Equation 1.6.[20]

$$n = \frac{8}{3\sqrt{\pi}}\left(\frac{2\pi m^* k_B T}{h^2}\right)^{3/2} \eta_F^{3/2} \tag{1.6}$$

Typically, an extrinsic semiconductor will only have one type of charge carrier, and Equation 1.6 takes the same form when either holes or electrons are dominant. Since η_F depends inversely on T, the carrier concentration is largely independent of temperature and more so dependent on the level of doping. Moreover, m^* is the effective mass of a charge carrier

when surrounded by a crystal lattice. Since electrons are influenced by the electric potential from positive ions which make up the lattice, their mass is effectively reduced from the free electron mass ($m^* < m_0$) by the electric field that surrounds them. For a charge carrier in a semiconducting material, the effective mass m^* is dependent on the electronic band structure (i.e., the dispersion of carriers with k values at some energy E), as shown by Equation 1.7.

$$m^* = \frac{\hbar^2}{\mathrm{d}^2 E/\mathrm{d}k^2} \tag{1.7}$$

In the above we observe that m^* is inversely proportional to the curvature of the electronic band structure at some momentum-energy point. Accordingly, a high effective mass is obtained for carriers in flat bands flatter bands with small curvaturve. At the same time, carriers in high curvature, sharp bands will have a low effective mass. With m^* and the charge of the carrier (e, the elementary charge), one may calculate the carrier mobility (μ) from Equation 1.8.

$$\mu = \frac{e\tau}{m^*} \tag{1.8}$$

Shown above, e takes on a positive or negative value when holes or electrons, respectively, are the dominant charge carrier. Owing to differences in effective mass and charge, electrons and holes may have vastly different mobilities in a bulk crystal. Additionally, τ is the time between scattering events which depends on the various mechanisms that impede the flow of charge carriers in a material. Numerous scattering mechanisms are possible in pure and impure materials, and the rates (τ^{-1}) at which these mechanisms scatter carriers are additive according to Matthiessen's rule (Equation 1.9).[18]

$$\tau_{total}^{-1} = \tau_{lattice}^{-1} + \tau_{ionized\ \ impurity}^{-1} + \tau_{defect}^{-1} + \tau_{electron\text{-}electron}^{-1} + \cdots \tag{1.9}$$

Here, the rates of some typical scattering mechanisms are shown to be summative. In pure materials, lattice ions act as scattering cites for charge carriers. Ionized impurities and defects in the lattice can engender a difference in the spatial potential, and in certain cases, carrier-carrier scattering may also occur.

All of the aforementioned properties of charge carriers, conducting through k-space and real space, determine the macroscopic electrical behavior of a material.The electrical conductivity (σ) of a solid material is dependent on its carrier concentration (n), the charge of the carrier (e), and the mobility (μ). According to Equation 1.10, electrons and holes contribute to the total electrical conductivity.

$$\sigma = n_e e\mu_e + n_h e\mu_h \tag{1.10}$$

In Equation 1.10, the first term accounts for conductivity from electrons, while the second term accounts for the hole contribution. As will be discussed in the next section, high σ is desirable for TE applications. Therefore, to achieve high electrical conductivity, the carrier concentration and mobility should be large. Considering Equation 1.8, materials with low effective mass for carriers are favorable for obtaining high electrical conductivity in semiconducting materials.

1.2.3 Heat Transport

The thermal behavior of materials is fundamental to TE effects in semiconductors. Heat in a solid material depends on vibrations in the lattice known as phonons. To gain a visual representation of vibrational waves propagating through a crystal lattice, it is useful to think of the atoms as a network of connected balls and springs, as illustrated in Figure 1.5. When

given some energy, ions will oscillate in the lattice such that they push or pull on the other atoms in the crystal.

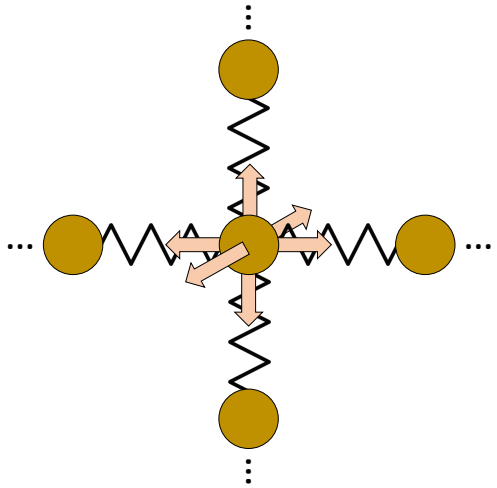

Figure 1.5: Diagram representing atoms vibrating in a crystal lattice where atoms and bonds are represented as balls and springs. Lattice atoms in the direction in and out of the page are not depicted.

Phonons in a crystal can be thought of like waves that travel through the sea. In a chain of connected atoms, waves propagate in two forms: longitudinal and transverse waves. When atoms vibrate toward and away from each other in the same direction as the wave propagation, the phonon is considered to be longitudinal. On the other hand, transverse waves involve the vibrational motion of atoms in directions perpendicular to direction of wave propagation. Accordingly, two transverse wave directions are possible, while only one direction of longitudinal wave exists. Overall, phonons carry energy which manifests in the macroscopic physical quantity of temperature. In other words, as the oscillatory motion of atoms within a system becomes more intense (i.e., as more thermal energy is contained), a greater amount of heat energy will be transmitted through the material.

To begin the discussion of phononic energetics, we will consider the a one dimensional crystal made up of atoms of the same mass which behave as harmonic oscillators. For these

classical systems, no oscillation damping occurs and the motion of atoms is periodic. In turn, the idealized angular frequency (ω_0) of a harmonic oscillator, depicted by Equation 1.11, may be used used to describe the rate at which atoms vibrate in a lattice.[18]

$$\omega_0 = \left(\frac{k_s}{m}\right)^{1/2} \tag{1.11}$$

Shown above, m is the mass of the oscillating object and k_s is a spring constant for the system that defines the stiffness or looseness of the bonds. A larger k_s value describes a system in which atoms exist in a tightly bound lattice. Furthermore, if an ion is displaced from its equilibrium position by a displacement (x) in one direction, the spring will exert a restoring force to minimize the system energy. The spring force (F_s) is calculated by Hooke's law (Equation 1.12).

$$F_s = -k_s x \tag{1.12}$$

In general, F_s is negative because the springs always resist the displacement of an atom from its lowest energy state (i.e., its equilibrium position). The spring potential energy (V_s) is obtained by integrating the F_s over the displacement range (x), as shown in Equation 1.13.

$$V_s = \int_0^x k_s x \ \mathrm{d}x = \frac{1}{2} k_s x^2 \tag{1.13}$$

Due to the law of energy conservation, the change in kinetic energy will be equivalent to the change in elastic potential energy. This means that as the vibrational motion of lattice ions increases, their displacements will also increase. At $T = 0$ K, the atoms have zero kinetic energy ($k_B T = 0$ J) and the atoms reside in their equilibrium positions ($x = 0$ m). Since the elastic potential energy of the quantum mechanical system is strictly spatially dependent

($U(x) = V_s(x)$), the time independent Schrödinger equation (Equation 1.2) may be used to determine the energy eigenstates (E) for which phonon energy modes are allowed. Equation 1.14 displays the time independent Schrödinger equation for a harmonic oscillator.

$$\frac{-\hbar^2}{2m}\frac{\partial^2\psi(x)}{\partial x^2} + \left(\frac{1}{2}kx^2\right)\psi(x) = E\psi(x) \tag{1.14}$$

Ultimately, a quantized set of discrete energy eigenstates are obtained as solutions, which describe available energy levels which phonons may adopt. Ultimately, the allowed energies of vibrations in a lattice take the form of Equation 1.15.

$$E_n = \left(n + \frac{1}{2}\right)\hbar\omega \tag{1.15}$$

In the above, E_n is the energy eigenvalue for a given quantum number ($n = 0,\ 1,\ 2,\ 3\ \cdots$). From these results, one may obtain the dispersion relation between phonon frequencies and vectors in k-space, as shown in Equation 1.16 for a lattice with lattice parameter (a).[18]

$$\omega = 2\omega_0\left|\sin\left(\frac{1}{2}ka\right)\right| \tag{1.16}$$

As was the case with electronic band structures, a dispersion relation between phonon frequency (ω) and wavenumber (k) exists in a periodic form such that all physically significant energies may be reduced to k values in the first Brillouin zone ($\frac{-\pi}{a} \leq k \leq \frac{+\pi}{a}$). Furthermore, the trigonometric term is maximized when the argument is equal to $\pi/2$ radians. This implies that a maximum frequency (ω_{max}) which is only dependent on k_s and m of the atoms involved. This maximum exists at the Brillouin zone boundaries ($k = \pm n\frac{\pi}{a}$ where n includes

all non-zero integers) according to Equation 1.17.

$$\omega_{max} = 2\omega_0 \tag{1.17}$$

Furthermore, a group velocity (v_g), which describes the speed at which an energy carrying vibrational wave propagates, may be determined. Equation 1.18 yields the group velocity by taking the derivative of ω with respect to k, as shown in Equation 1.18.

$$v_g = \frac{\mathrm{d}\omega}{\mathrm{d}k} = \omega_0 a \cos\left(\frac{1}{2}ka\right) \tag{1.18}$$

From v_g one may obtain information regarding the rate at which a vibrational wave (e.g., sound or heat) travels through space with respect to time, or the rate at which its oscillatory frequency changes with respect to momentum (k). Qualitatively, the group velocity for a material may be found by analyzing the slope in the phonon dispersion near the $k = 0$ point.

Figure 1.6a displays the reduced phonon dispersion diagram for a one dimensional solid with only one unique type of atom ($N = 1$). Owing to the periodicity of the lattice, all solutions for E may be satisfied by k values in the first reciprocal space zone. As discussed previously, lattice waves may adopt energies with corresponding frequencies from 0 to some maximum value ($0 \leq \omega \leq \omega_{max}$). The slope in the phonon dispersion near the zero-point describes the speed at which phonons propagate in a material.

We may expand this understanding by considering the phonon dispersion of a three dimensional material containing two different types of atoms. Figure 1.6b represents the phonon dispersion for a three dimensional crystal comprised of a two different types of atoms ($N = 2$). If the phonon dispersion is determined for a solid with two atoms of differing

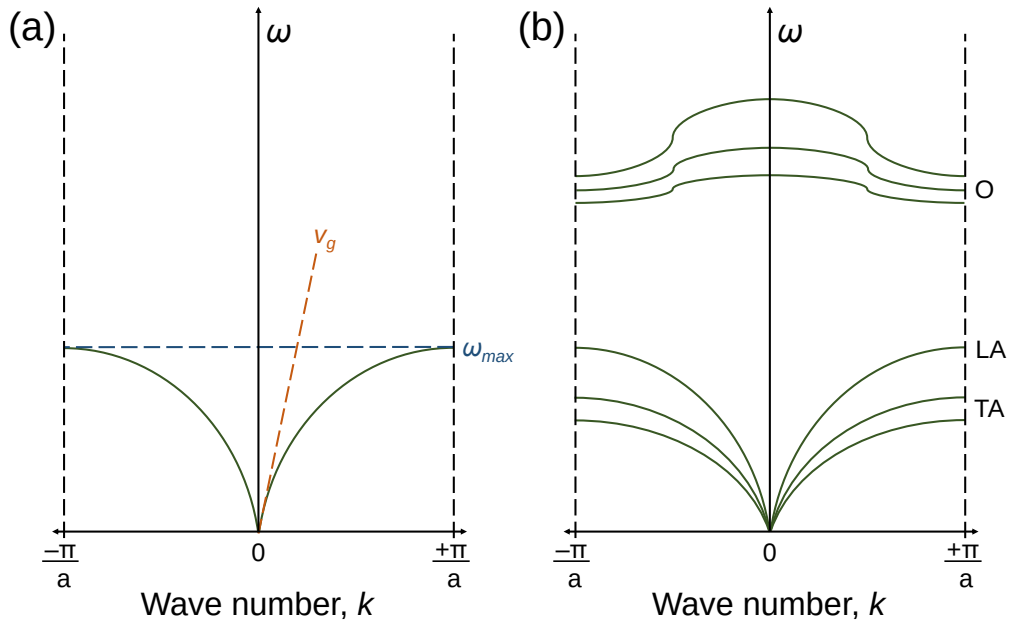

Figure 1.6: Generalized phonon dispersion diagrams for a (a) one dimensional solid comprised of one atom type and (b) three dimensional solid comprised of two different atom types. ω is the phonon frequency and k is the wavenumber. Allowed vibrational energy states exist up to a maximum frequency (ω_{max}) and the group velocity (v_g) of a specific vibrational mode is obtained from the slope of the branch as it approaches the zero k-point. In a bulk crystal, 2 transverse acoustic (TA) modes, 1 longitudinal acoustic (LA), and several optical (O) modes exist in the phonon dispersion.

masses, two degenerate solutions for E are obtained for each value of k. The vibrational energy levels split into a collection of low energy modes, termed the acoustic branch, and high energy modes, called the optical branches. While the acoustic modes correspond to in-phase motion between oscillating lattice ions, optical modes correspond to out-of-phase vibrations between atoms. Moreover, the acoustic branch is characterized by high v_g and low ω values, whereas optical branches are classified by low v_g and high ω values. In this way, acoustic phonons are on the same energy scale as sound and heat waves, while optical phonons adopt energies on the scale of infrared electromagnetic radiation.

When considering the crystal in three dimensions, acoustic phonons split into one longitudinal and two transverse waves, as is consistent with the qualitative representation discussed

at the beginning of this subsection. For a highly symmetric lattices (e.g., cubic systems), the different transverse modes converge to the same degenerate values owing to the isotropy of the crystal. To further complicate the model, when several different unique atoms ($N \geq 3$) are present in the structure, three acoustic modes will remain while the number of optical modes increases to $3(N-1)$. In other words, there is a non-zero density of states for vibrational energy modes which phonons may adopt. The physical origin for conduction of thermal energy in solids is a result of phonon dynamics in the crystal.

The mechanism by which heat propagates in a solid is ultimately through collision-like interactions where energy is inelastically transferred from one object colliding with another. It follows that a kinetic gas model may be used to describe the flow of heat in a crystalline system. Phonons can be thought of as the quantum mechanical objects which relate the total internal energy of a system to its thermal state. According to the equipartition theorem, each vibrational degree of freedom in a system will add $\frac{1}{2}k_BT$ of thermal energy to the total internal energy. The internal energy (U) based on the number of atoms (N_A) and the temperature (T) of a system with f degrees of freedom is shown in Equation 1.19.[18]

$$U = \frac{f}{2}N_A k_B T \tag{1.19}$$

Here, a common simplification is made by substituting the gas constant ($R = N_A k_B$) into Equation 1.19. According to the classical kinetic gas model, each atom in a crystal vibrates with six degrees of freedom (i.e., kinetic and potential energy components in x, y, and z directions). Accordingly, a term known as the heat capacity (C), which defines the change in the internal energy of a system as temperature varies, may be calculated by deriving

Equation 1.19 with respect to temperature (see Equation 1.20).

$$C = \frac{\mathrm{d}U}{\mathrm{d}T} \tag{1.20}$$

The heat capacity is a measure of how much energy is required to change the temperature of a defined amount of material by 1 °C. Classically, values of C in solid materials converge to $3R$ (i.e., Dulong-Petit heat capacity). In general, a Dulong-Petit approximation may be used to describe the heat capacity of most materials at high temperatures. However, a more encompassing model is the Debye model for heat capacity, where U of a system may be described based on phonon dispersion behavior in a material. The Debye model considers the frequency dependent phonon energy ($E(\omega)$), vibrational density of states ($g(\omega)$), and the probability distribution function ($f(\omega)$) to estimate U for a solid system (see Equation 1.21).[18]

$$U = \int_0^{\omega_{max}} E(\omega)g(\omega)f(\omega)\ \mathrm{d}\omega \tag{1.21}$$

By this model, only frequencies up to the maximum phonon frequency (ω_{max}) must be considered. For phonons which behave as Einstein oscillators, the energy is discretized solely based on ω (i.e., $E(\omega) = \hbar\omega$). Phonons are a type of quantum mechanical wave that differs from fermions, called bosons. These wave-particles assume integer spin values which enables them to occupy the same quantum state as other bosons. Accordingly, the function shown in Equation 1.22 may be used to approximate the phonon density of states ($g(\omega)$) from the phonon frequency (ω), average group velocity ($\bar{v}_g$), and system volume (V).

$$g(\omega) = \frac{3V\omega^2}{2\pi^2\bar{v}_g^3} \tag{1.22}$$

Moreover, these quantum mechanical systems adopt energy levels according to Bose-Einstein statistics. Equation 1.23 shows the phonon probability distribution function as it relates to ω and T.[18]

$$f(\omega) = \frac{1}{\exp\left(\frac{\hbar\omega}{k_B T}\right) - 1} \tag{1.23}$$

Putting all of these factors together allows one to calculate the internal energy for a system based on its phonon dispersion properties. Upon integration of the U in Equation 1.21, one obtains the expression for heat capacity (C) shown in Equation 1.24.[18] To simplify the integration and improve visual clarity, an integration constant of $x = \frac{\hbar\omega}{k_B T}$ is introduced and e is used for Euler's number.

$$C = 9R\left(\frac{T}{\theta_D}\right)^3 \int_0^{\theta_D/T} \frac{x^4 e^x}{(e^x - 1)^2}\ \mathrm{d}x \tag{1.24}$$

Shown above, θ_D is a characteristic value known as the Debye temperature. This material-specific feature describes the thermal energy equivalent of a crystal's highest energy vibrational mode. In Equation 1.24, the upper integration bound is based on a term known as the Debye frequency (ω_D). Similar to θ_D, the highest vibrational frequency achievable by phonons in a distinct crystalline system is defined by ω_D. Equation 1.25 calculates ω_D as it relates to the phonon velocity (v_g), the Debye temperature (θ_D), and the number density ($\frac{N_A}{V}$) of atoms in three dimensional crystalline system.

$$\omega_D = v_g (6\pi^2 N_A)^{1/3} \tag{1.25}$$

All in all, the Debye model is an appropriate model for determining the heat capacity of a broad range of crystalline materials. At high temperatures, values from the Debye model

converge to the Dulong-Petit value ($C = 3R$).

By utilizing Debye heat capacity model, we are now able to discuss the macroscopic material phenomenon of thermal conduction. In general, thermal conductivity (κ) is a measure of the rate of heat transfer ($\dot{Q}$) in a material under a thermal gradient (∇T), as shown in Equation 1.26.

$$\dot{Q} = -\kappa \nabla T \tag{1.26}$$

Thermal conductivity (κ) is defined by Equation 1.27 where D is the density of the material, C_p is the heat capacity at constant pressure, and α is a property known as the thermal diffusivity.

$$\kappa = \alpha D C_p \tag{1.27}$$

Thermal transfer by phonons is known as the lattice thermal conductivity (κ_L), while thermal conduction from charge carriers is termed the electronic thermal conductivity (κ_e). The total thermal conductivity (κ_{total}) of a semiconducting material is obtained by summing the contributions from κ_L and κ_e, as displayed by Equation 1.28.

$$\kappa_{total} = \kappa_L + \kappa_e \tag{1.28}$$

In the case of a material where both electrons and holes are present, a third contribution called the bipolar thermal conductivity exists. However, an understanding of this phenomenon is not necessary in the scope of this report. Equation 1.29 may be used to calculate the lattice thermal conductivity (κ_L) contribution.

$$\kappa_L = \frac{1}{3} C_v v_g \ell_{ph} \tag{1.29}$$

In the above equation, C_v is the heat capacity at constant volume, v_g is the phonon group velocity, and ℓ_{ph} is the phonon mean free path which describes the average distance traveled by a phonon before undergoing a scattering event. Phonon velocity is related to the mean free path by $v_g = \frac{\ell_{ph}}{\tau}$, where τ is the time between scattering events. Following Matthiessen's rule, phonon scattering rates (τ^{-1}) are summative, as shown in Equation 1.30.

$$\tau_{total}^{-1} = \tau_{phonon\text{-}phonon}^{-1} + \tau_{mass\text{-}difference}^{-1} + \tau_{boundary}^{-1} + \cdots \tag{1.30}$$

Some of the most common forms of phonon scattering involve phonon-phonon scattering, mass-difference scattering from impurities or defects, and grain boundary scattering at dislocations in the crystal lattice. Other less prominent scattering mechanisms (e.g., phonon-carrier interactions) exist as well. At low temperatures, less phonons are produced, and phonon-phonon scattering occurs less frequently. Therefore, at temperatures much lower than the Debye temperature, the mean free path of phonons approaches the grain size of the bulk material.

While much of our discussion has assumed that phonons behave as idealized quantum oscillators, this is not the case in reality. Deviations from harmonic behavior arise because the bonding between atoms in a lattice changes as temperature increases or decreases (i.e., the lattice loosens or stiffens). On a macroscopic scale, these effects manifest in the thermal expansion of solids, and a property known as the Grïeisen parameter (γ) quantifies the degree of anharmonicity in a material. Greater values of γ indicate more significant anharmonic behavior, which generally leads to lower values of κ_L.Phonons interact by two different scattering processes: normal interactions and Umklapp interactions. Overall, Umklapp scattering is the physical origin for thermal resistance in well-ordered crystals at high

temperatures. As temperature increases up to and beyond the Debye temperature, Umklapp scattering becomes more significant because the greater quantity of phonons leads to an exponential decrease in ℓ_{ph} with increasing T. This manifests in a reduction of κ_L as T increases.

Whereas κ_L pertains to the transfer of heat by phonons, the electronic thermal conductivity (κ_e) describes heat transfer from charge carriers. The Wiedemann-Franz law relates κ_e to the electrical conductivity (σ) and temperature (T) according to Equation 1.31.

$$\kappa_e = L\sigma T \tag{1.31}$$

As displayed above, the Lorenz number (L) acts as a proportionality constant which, for a conductive material (e.g., metal or degenerate semiconductor), is equal to roughly 2.4×10^{-8} WΩK^{-2}. As T approaches 0 K, κ_e is the dominant component of the total thermal conductivity because significantly less phonons are being produced, thereby leaving electrons and holes as the sole carriers of heat. Overall, materials that demonstrate low κ are favorable for TE applications. Accordingly, poor electrical conductors are useful in achieving low κ_e values. Similarly, materials with significant lattice anharmonicity, low heat capacity, slow phonon velocities, and a minimal mean free path are desirable for their low κ_L. Materials engineering tactics, as well as some fundamental contradictions, for achieving these results will be addressed in the next subsection.

1.2.4 Thermoelectric Phenomena

Thermoelectricity describes the physical phenomenon where a voltage difference is induced by a temperature gradient across a material.[21] This spectacle was discovered by Thomas

Johann Seebeck in the 1820s, when he observed an electromotive force after heating a current loop consisting of two dissimilar conductors.[22, 23] The Seebeck effect is the underlying physical origin for thermal to electrical energy conversion capabilities of these unique physical systems. A similar discovery was realized by Jean Charles Athanase Peltier in 1834, where an electric current passed along the junction of two different metals led to an absorption or liberation of heat at the junction.[24] By reversing the direction of electric current, Peltier noticed a concomitant shift in the direction of the heat flow. Converse to the Seebeck's discovery, the Peltier effect allows for TE cooling effects by providing electricity to a material. Starting in the 1960s, TE materials were heavily researched for power generation and solid-state cooling applications.[20, 25] Since then, the efficiency of TE materials has increased more than twofold, primarily from advancements made within the last two decades.

To better understand how electricity is generated from a heat input on one side of a material, one must consider the interplay between charge transport and thermal conduction in solids. Figure 1.7 illustrates the basic underlying principle of the Seebeck effect. In the case of a material where electrons are the primary charge carriers (i.e., an n-type semiconductor), the carriers will possess a kinetic energy that scales with T (see Equation 1.19). It follows that electrons on the hot side of the material will be moving with greater velocity (i.e., a greater kinetic energy) than the electrons on the cold side. The random thermal motion of carriers causes electrons to diffuse in such a way that they all collect on the cold end of the material. In other words, hot electrons travel fast and far, while cold electrons move slowly over smaller distances. This spatial imbalance of charge carriers induces a difference in electric potential (i.e., a voltage drop) across the material, and the electrical bias generated by a material under a thermal gradient is a consequence the Seebeck effect.

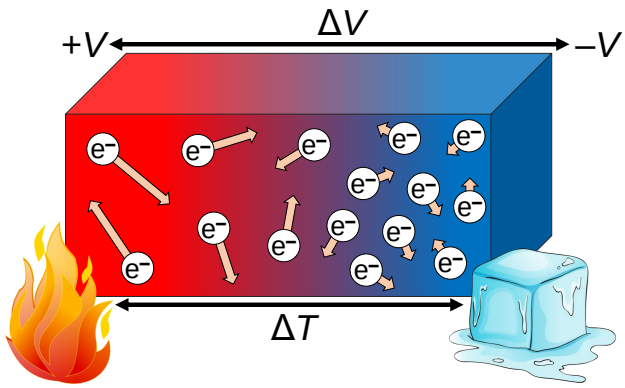

Figure 1.7: Diagram illustrating the underlying principle of the Seebeck effect. When a temperature gradient exists across a material, charge carriers on the hot end will move with greater kinetic energies and velocities (depicted by beige arrows with sizes qualitatively representing the magnitudes of velocities). In turn, a voltage difference is generated across the material.

The Seebeck effect is quantified in materials by a property known as the thermopower (S). In general, S is a proportionality constant that relates the voltage (ΔV) generated to the temperature difference (ΔT) across a material (see Equation 1.32).

$$S = \frac{\Delta V}{\Delta T} \tag{1.32}$$

Since the accumulation of charge carriers depends on their motion and scattering, it follows that a simple scattering law for covalent crystals may be used to approximate S in semiconducting materials.[20] Equations 1.33 and 1.34 are used to determine the thermopower of non-degenerate (i.e., intrinsic) and degenerate (i.e., strongly extrinsic) semiconductors, respectively.

$$S = \frac{k_B}{\pm e}\left(5/2 + \lambda + \eta_F\right) \qquad \text{Non-degenerate} \tag{1.33}$$

$$S = \left(\frac{\pi^2}{3}\right)\frac{k_B}{\pm e}\frac{\left(3/2 + \lambda\right)}{\eta_F} \qquad \text{Degenerate} \tag{1.34}$$

In the previous equations, value of e will be either positive or negative when holes or electrons, respectively, are the dominant charge carrier. In other words, a p-type material will have positive S values, while an n-type material will have negative S values. The scattering constant (λ) describes the dominant scattering mechanism in a material. Some common values assumed by λ are $^{-1}/_{2}$ for high-temperature phonon-phonon scattering, $^{1}/_{2}$ for scattering in ionic crystals at high temperatures, or $^{3}/_{2}$ for ionized impurity scattering.[20] Of course, these expressions are only approximations, and in real systems, a mixture of scattering may be present at certain temperatures. By an energy-independent scattering approximation, the thermopower (S) of a degenerate semiconductor relates to temperature (T) and the carrier concentration (n) according to Equation 1.35.[26]

$$S = \frac{8\pi^2 k_B^2}{3eh^2} m^* T \left(\frac{\pi}{3n}\right)^{2/3} \tag{1.35}$$

In general, the magnitude of the thermopower is expected to rise with temperature because as temperature increases, the greater thermal energy of the system provides more energy for charge carriers to migrate across the material. Therefore, the Seebeck effect is the physical origin for thermoelectricity in semiconducting materials. The overall effect involves an imbalance of charge carriers between opposite ends. In this respect, the thermopower may be thought of as a measurement of the system entropy. Whereas particles would adopt their equilibrium position in an ordered crystal at $T = 0$, the addition of temperature causes the system to adopt a less probabilistic state. To maximize the voltage from a heat input, TE applications benefit from using compounds with high S. In turn, to obtain the greatest thermopower, a semiconducting material should have low carrier concentrations and heavy carrier effective mass.

1.3 Materials Engineering of Thermoelectrics

While the phenomenon of thermoelectricity has been known of for quite some time, significant research efforts have been made over the last twenty years to improve TE performance of semiconducting materials. With increased pressure from energy and environmental concern, TE research gained momentum, especially owing to the onset of nanotechnology and modern scientific equipment. This section will detail what materials serve as good candidates for TE applications and how they can be engineered to improve their performance. Lastly, a discussion of device manufacturing and some state-of-the-art TEs will transpire.

1.3.1 Conversion Efficiency and the Figure of Merit

Macroscopic electrical and thermal material properties determine the effectiveness at which semiconducting materials can convert thermal energy to electrical power. In general, TE materials behave as heat engines with charge carriers as the working fluid.[27] Heat engines function by taking thermal energy from a heat source and transferring it to a heat sink, while also converting some of the thermal energy into work.[28] Accordingly, for any heat engine, one must identify the temperature of the heat source (T_H) and the temperature of the heat sink (T_C). TE technology seeks to generate the greatest power output from as little heat input as possible. Accordingly, a dimensionless figure of merit (Z), determined by Equation 1.36, is often used to describe the TE performance of a material.

$$Z = \frac{S^2\sigma}{\kappa} \tag{1.36}$$

In the above equation, S is the thermopower, σ is the electrical conductivity, and κ is

the thermal conductivity (κ). The numerator of Z is called the power factor (PF), which describes the capability of a material to produce electrical power. When discussing TE behavior of materials, it is often convenient to refer to the product of Z and T since the material properties that comprise Z are temperature dependent. In addition, ZT is explicitly used in the calculation of a material's thermoelectric conversion efficiency (ε) as shown in Equation 1.37.[26]

$$\varepsilon = \left(\frac{T_H - T_C}{T_H}\right)\frac{(1+ZT)^{1/2}-1}{(1+ZT)^{1/2}+\frac{T_C}{T_H}} \tag{1.37}$$

Shown above are T_H for the hot-side temperature and T_C for the cold-side temperature. It is immediately apparent that ε will increase as the difference between T_H and T_C increases (i.e., as ΔT increases). Additionally, the first term in parentheses is the Carnot efficiency ($\varepsilon_{carnot} = {}^{(T_H - T_C)}/_{T_H}$) which describes the maximum theoretical efficiency of a heat engine.[29]

A tangible situation for applying TE technology is in extracting heat from the exhaust of an automobile.[30] Commonly, ZT values of 1 (i.e., unity) typify decent TE materials, with more recent advancements achieving ZT data well above 2.[31] As a rough calculation, we will assume that the byproduct gas from an internal combustion engine is at a temperature of 700 K, and a TE material with a ZT = 1 is used to convert the heat to electricity. If the thermoelectric is cooled to room temperature (about 300 K) on the cold-side, then an efficiency of about 13% is attainable for this system. While these conditions are somewhat idealized, this determination illustrates the potential that TE technology offers for power generation applications.

According to Equation 1.37, a material's conversion efficiency is also related to ZT, such that higher values of ZT will result in higher ε. At this point, some assertions may be made

about which materials will be good TEs. First, a high-performing material should be able to withstand a large thermal gradient across the material such that it maintains a large ΔT. Next, higher values of ZT will result in higher values of ε. With this knowledge, it follows from Equation 1.36 that good TE materials should demonstrate high thermopower, high electrical conductivity, and low thermal conductivity.

1.3.2 Contraindicated Material Properties

Unfortunately, the fundamental parameters which control the electrical and thermal materials properties are not mutually exclusive. This means that thermopower, electrical conductivity, and thermal conductivity are contraindicated in a way that causes a concomitant benefit and detriment to ZT. For example, the carrier concentration of a semiconducting material influences the thermopower and electrical conductivity in an inverse fashion. For instance, to obtain a large thermopower, a low carrier concentration and high effective mass is desirable. Yet, at the same time, a high carrier concentration and low effective mass would be favorable for improving the electrical conductivity. Another canonical example is the relationship between high electrical conductivity and high thermal conductivity. Due to the contribution from the electronic thermal conductivity, a simultaneous rise in thermal conductivity will be observed with an increase in electrical conductivity. To get around these problems, several materials engineering techniques have prominently been used to provide significant enhancements to ZT. Regardless, the contraindication of TE properties presents a challenge for achieving high efficiencies in these devices.

Semiconductors are preferable for TE applications because their properties are highly tunable via doping. It is possible to engineer a semiconductor with the optimal carrier concentration to allow for all the material properties to combine to maximal ZT value.[26]

Indeed, doping has been shown to provide significant enhancements in ZT over the years.[32] This tactic allows for modification fo material properties, by effectively raising or lowering the Fermi level through the addition or removal of charge carriers from the lattice. Qualitatively, the thermopower is maximized when the Fermi level is located near the edge of the valence or conduction band where the sharpest drop-off in the density of states exists. Hence, doping is a viable engineering technique for improving performance in TE semiconductors particularly through modulation of the electrical properties.

Significant efforts have been made to find low thermal conductivity materials that are still able to conduct electricity relatively easily. One approach that has demonstrated success in reducing lattice thermal conductivity is the phonon-glass electron-crystal (PGEC) approach.[33] This is a concept where materials exhibit heat transport characteristics of an amorphous glass while charge transport resembles that of a well-ordered crystalline material. Essentially, the goal in these solids is to engineer them such that the phonons are scattered very effectively without significantly scattering electrons. With great enough phonon scattering, the lattice thermal conductivity can reach values near a theoretical minimum when the phonon mean free path is on the order of the interatomic spacing of the lattice.[34] In other words, when phonons are scattered as frequently as they encounter an atom in the crystal, a minimum lattice thermal conductivity will be achieved.

In particular, the PGEC approach has been shown to be successful through the use of rattler atoms. In materials where the crystal lattice resembles an over-sized atomic cage, dopant atoms can be incorporated into the lattice such that they are loosely bound, suppressing acoustic phonon modes.[35] Rattlers vibrate at frequencies on the same energy scale as acoustic phonons in a way that allows for interactions (i.e., scattering) between the atom and phonons. In this case, an additional contribution to the heat capacity (C_E), described

by Equation 1.38, may arise in the form of an Einstein-like vibrational mode.[36]

$$C_E = 3R\left(\frac{\theta_E}{T}\right)^2 \frac{e^{\theta_E/T}}{\left(e^{\theta_E/T}-1\right)^2} \tag{1.38}$$

In the above, θ_E is a characteristic temperature of the mode, known as the Einstein temperature, which is related to the mode's vibrational frequency ($\theta_E = \frac{\hbar\omega}{k_B}$). Hence, This technique is particularly useful for skutterudite and clathrate compounds.[37, 38] Localized rattling contributes to phonon scattering, and it has been shown that these materials demonstrate significant reductions in thermal conductivity.

Advancements in nanotechnology enable a whole new realm of possibilities for materials science and TE research.[39, 40] Two of the primary phonon scattering mechanisms, mass difference impurity scattering and interfacial scattering, may be emphasized in materials through the exploitation of doping and low-dimensionality. A greater density of grain boundaries are present in nanostructured materials. The increased presence of grain boundaries leads to significantly enhanced phonon scattering. This is especially true in the case of hierarchically structured materials which utilize defect scattering sites on several different length scales (i.e., mesoscopic, microscopic, or nanoscopic regimes) to encourage scattering processes on multiple energy scales. Such materials purposefully employ grain boundaries, precipitated secondary phases, nanoscale inclusions, and point defects to scatter phonons.[41] Therefore, materials engineering techniques like doping, nanotechnology, and rattler atom incorporation have led to massive improvements in ZT over the past two decades.

1.3.3 Thermoelectric Devices and State-of-the-art Materials

In practical applications, TE devices consist of semiconducting materials which are carefully arranged in a specific orientation to maximize power output. A thermoelectric unicouple is comprised of one n-type semiconducting leg and one p-type leg. Figure 1.8a displays a generalized schematic of a TE unicouple. Overall, the temperature gradient motivates charge carriers to drift from the hot side to the cold side, establishing a voltage drop across the unicouple. This electric potential can be used to provide electrical power to a resistive load just as a battery, solar cell, or engine could. To provide enough voltage for large-scale applications, many unicouples are connected according to the arrangement depicted in Figure 1.8b. The semiconducting legs of the unicouples are linked electrically in series and thermally in parallel. Modules typically have a ceramic substrate which allows for maximal heat absorption and spreading owing to a large surface area and high thermal stability.[42] In TE generators, heat sinks are commonly employed to establish and maintain the lowest possible temperature on the cold-side.

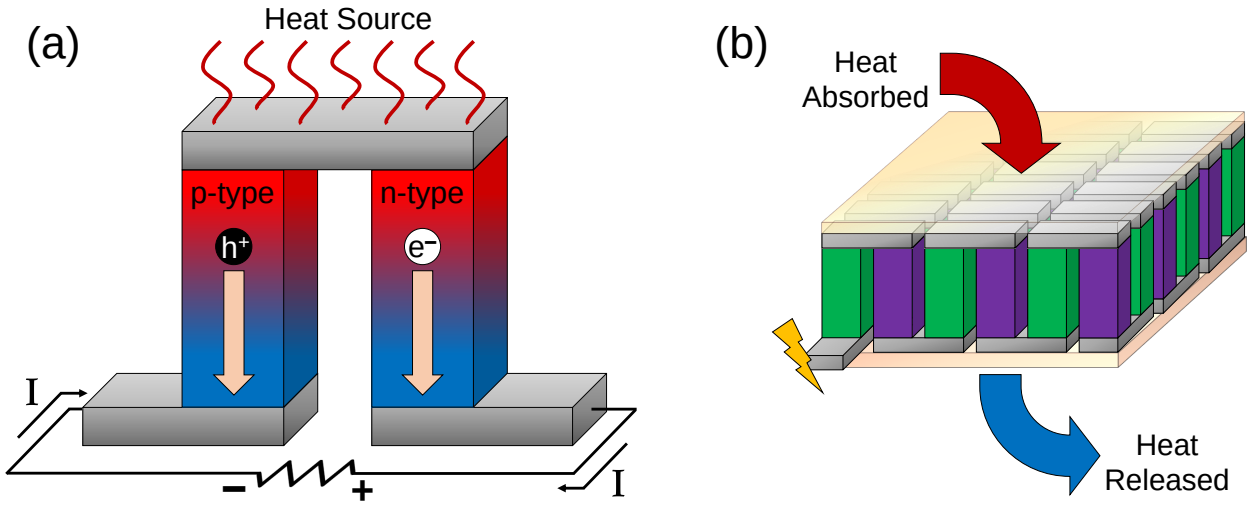

Figure 1.8: Diagram illustrating a (a) thermoelectric unicouple and (b) device of multiple unicouples connected electrically in series and thermally in parallel. In (a), I represents electrical current, and in (b), purple and green prisms represent p-type and n-type materials.

Several quintessential materials have demonstrated properties which make them viable for TE applications. Figure 1.9 displays optimized ZT values obtained for multiple promising compounds. At low temperatures, bismuth telluride (Bi_2Te_3) demonstrates superior TE properties over other materials. Lead telluride (PbTe) is one the most well-known TE materials owing to its high ZT at intermediate temperatures. Similar lead chalcogenides (e.g., PbSe and PbS) have demonstrated good TE properties as well. As for high temperature TE materials, silicon germanium (SiGe) is commonly used, especially in radioisotope thermoelectric generators for deep-space applications.

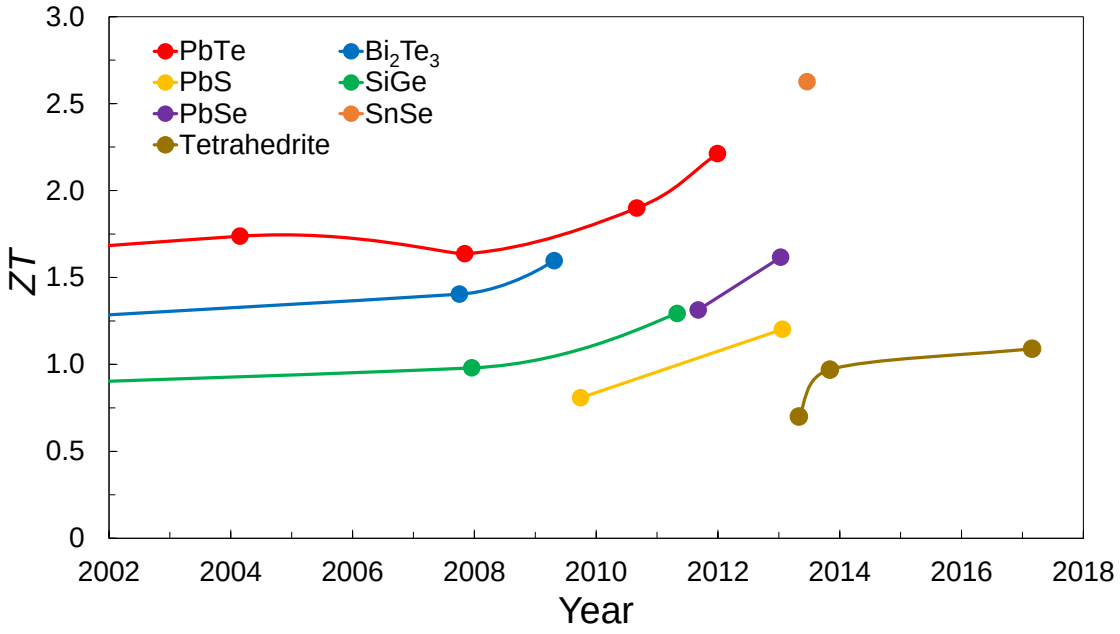

Figure 1.9: Peak ZT values obtained for several canonical thermoelectric materials. Lines serve as guides for the eye, and data was adapted from Zhang and Zhao.[32]

Unfortunately, all of the aforementioned compounds consist of toxic elements, such as Pb, or low-abundance elements, such as Te or Ge. For these reasons, materials scientists have begun exploring earth-abundant compounds for their TE properties. For example, tin selenide (SnSe) recently demonstrated an exceptionally high ZT of about 2.6 at 923 K.

However, this data was only obtained in one direction for a single crystal sample, and such a material would be difficult to manufacture for widespread applications. Therefore, although ZT values in state-of-the-art TE materials have been steadily improving for quite some time, many of these materials are not amenable to large-scale applications because they require the use of toxic elements, low abundance materials, and more involved syntheses.

Chapter 2

Tetrahedrite Materials

State-of-the-art TE materials often comprise environmentally harmful elements, such as Pb, or elements that exist in low abundance on earth, such as Te.[43] Hence, materials containing nontoxic and earth-abundant elements are worthy of investigation. These materials are amenable to large-scale applications because they are typically environmentally-friendly and inexpensive. Tetrahedrite compounds, of nominal composition $Cu_{12}Sb_4S_{13}$, are one class of materials that meet these criteria. Tetrahedrites occur naturally as a highly-abundant mineral around the world and are a common byproduct of the copper and silver mining industry.[44–46] Furthermore, tetrahedrites demonstrate relatively good electrical conductivity and thermopower, while also exhibiting exceptionally low thermal conductivity.[47–49] All in all, these materials consistently yield a ZT near unity around 700 K.[50] Tetrahedrite is an exemplary material for TE applications because of its low toxicity and high abundance, while still showing good TE properties for intermediate-temperature applications.

2.1 Fundamental Properties

The following subsections will focus on the crystallography and physical phenomena that govern the material properties of tetrahedrite. Henceforth, "Cu-based tetrahedrite" will be used in reference to $Cu_{12}Sb_4S_{13}$, which has also been termed the "undoped" or "parent form" in the past. Contrastingly, tetrahedrites that contain different substituent atoms will

be referred to as "doped" or "substituted" tetrahedrites. This section will primarily discuss Cu-based tetrahedrite because it is the most basic and fundamental variant.

2.1.1 Crystal Structure

The favorable TE properties of tetrahedrite are mostly a consequence of its complex crystal structure. The $Cu_{12}Sb_4S_{13}$ unit cell, shown in Figure 2.1 (produced via VESTA), is a body-centered cubic system with $I\bar{4}3m$ symmetry.[51–53] There are 58 atoms per unit cell with two unique Cu sites (12d and 12e), one Sb site (8c), and two S sites (24g and 2a).[54] Each Cu12d atom is tetrahedrally coordinated to four S24g atoms, whereas each Cu12e atom is trigonally coordinated to two S24g atoms and one S2a atom. In the trigonal coordination, the Cu12e atom is sandwiched between two Sb atoms such that the Sb lone pairs are oriented towards the Cu12e atom; this bonding effectively yields a trigonal bipyramidal arrangement for the Cu12e atom with two Sb atoms on the axial sites. Every S24g is tetrahedrally coordinated to two Cu12d atoms, one Cu12e atom, and one Sb atom. On the other hand, each S2a atom is in an octahedral coordination with six Cu12e atoms. Lastly, each Sb atom is tetrahedrally coordinated with three S24g atoms and a protruding lone pair, such that the Sb lone pair creates a void-like pocket in the structure. Therefore, the crystal structure of tetrahedrite is quite intricate and displays an array of distinct atomic bonding coordinations.

Each $Cu_{12}Sb_4S_{13}$ formula unit (f.u.) has a molar mass of 1666.45 g mol^{-1}, and the unit cell (u.c.) has a lattice parameter $a = 10.3908$ Å and a volume $V = 1.12{\times}10^{-21}$ cm^3.[51] Accordingly, Equation 2.1 calculates the theoretical density ($D_{Theo} = m/V$) of tetrahedrite from mass (m) of atoms in the unit cell and unit cell volume (V).

$$D_{Theo} = \frac{1666.45 \text{ g mol}^{-1}}{\text{f.u.}} \times \frac{1 \text{ mol}}{6.022 \times 10^{23}} \times \frac{2 \text{ f.u.}}{\text{u.c.}} \times \frac{\text{u.c.}}{1.12 \times 10^{-21} \text{ cm}^3} = 4.93 \text{ g cm}^{-3} \quad (2.1)$$

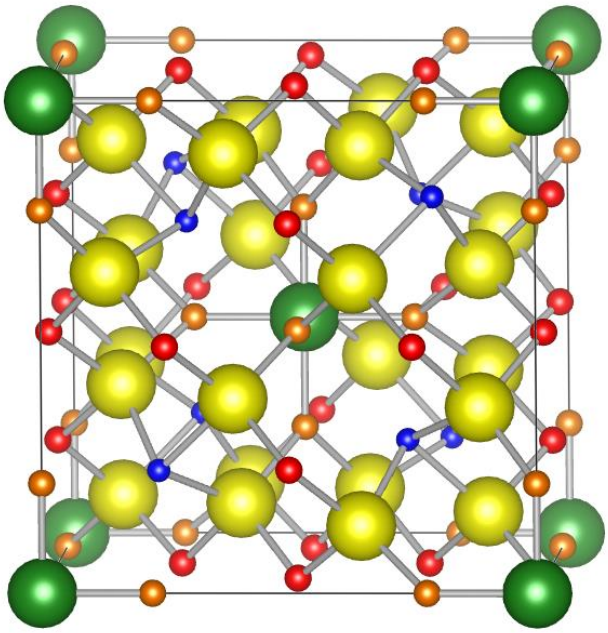

Figure 2.1: Unit cell of $Cu_{12}Sb_4S_{13}$ tetrahedrite where atoms are represented by spheres colored red for Cu12d, orange for Cu12e, blue for Sb, green for S2a, and yellow for S24g.

Although tetrahedrite exists as a body-centered cubic system at room temperature, it also demonstrates a structural phase transition at low-temperature. For many years, various groups recognized through electrical conductivity, heat capacity, and magnetic susceptibility measurements that a metal-semiconductor transition (MST) existed in $Cu_{12}Sb_4S_{13}$ around 85 K.[55–59] Several mechanisms were proposed to explain the physical origin of this MST, including Jahn-Teller distortion or an antiferromagnetic-paramagnetic transformation. However, two recent studies suggested that a cubic-tetragonal phase transition also occurs near 85 K. May et al. utilized temperature-dependent powder X-ray diffraction (XRD) to study the first-order crystallographic transformation.[60] Around the same time, Tanaka et al. rigorously analyzed the relationship between physical properties and structure above and below the transition temperature.[61] Additionally, numerous studies have shown that the phase transition is suppressed by the addition of dopants or isovalent substitutions.[60–62] These findings support the claim that chemical mutations effectively stabilize the cubic tetrahedrite

phase. In this way, the interesting low-temperature behavior of tetrahedrite materials could provide important fundamental information for understanding this class of materials and related systems.

2.1.2 Electronic Behavior

The valence states of different atoms in the tetrahedrite structure are not well-understood by the community, and several models have been proposed over the past 50 years. From a crystal chemistry perspective, a distribution of two Cu^{2+} and ten Cu^{1+} atoms would satisfy charge-balance ($Cu_{10}^{1+}Cu_{2}^{2+}Sb_{4}^{3+}S_{13}^{2-}$).[51] This model assumes ionic bonding character and predicts that the two Cu^{2+} atoms strictly occupy tetrahedral 12d sites. However, Cu-based tetrahedrites are stable over a large compositional range up to the $Cu_{14}Sb_4S_{13}$ and $Cu_{12}Sb_{4.67}S_{13}$ end-members, and in turn, a Brillouin-zone (BZ) model of valence electron counting was proposed. In BZ model, a window of stability is allowed for tetrahedrite compositions with 204 to 208 valence electrons.[63,64] Pattrick et al. supported the BZ model by using X-ray absorption spectroscopy to show that the ratio of Cu^{1+} to Cu^{2+} is dependent on chemical composition.[65] Contrary to both of these models, density-functional theory (DFT) calculations, complemented by experimental data, have provided evidence to suggest that all of the Cu atoms could maintain a monovalent state.[66] This claim is also justified by high ionic conductivity and mixed ionic/covalent bonding observed in tetrahedrites.[54] Thus, modern computational tools have enabled a novel framework for understanding atomic valence states in tetrahedrites, but there is still much more to be learned.

Cu-based tetrahedrite behaves like a metal with p-type conductivity. In 2013, Lu et al. calculated the electronic band structure and density of states of tetrahedrite via DFT (see Figure 2.2).[66] Since then, multiple other groups have made similar calculations.[67–69] In

$Cu_{12}Sb_4S_{13}$ (Figure 2.2a), the valence band is primarily a result of hybridization between Cu 3d and S 3p orbitals, whereas all elements contribute equally to the conduction band. The indirect band gap is approximately 1.1 eV, and the Fermi level (η_F) resides in the valence band near the band edge. By replacing Cu^{1+} with Zn^{2+} (Figure 2.2b), η_F rises and the sample becomes a true semiconductor with η_F in the gap. One can think of $Cu_{12}Sb_4S_{13}$ as a dirty metal, whereas $Cu_{10}Zn_2Sb_4S_{13}$ is the true semiconducting composition. In both cases, Hall measurements provide only a small signal, making determination of hole concentration and mobility difficult.[66, 70] Regardless, doping and substituting different atoms into the tetrahedrite structure may be used to manipulate its properties in a favorable way.

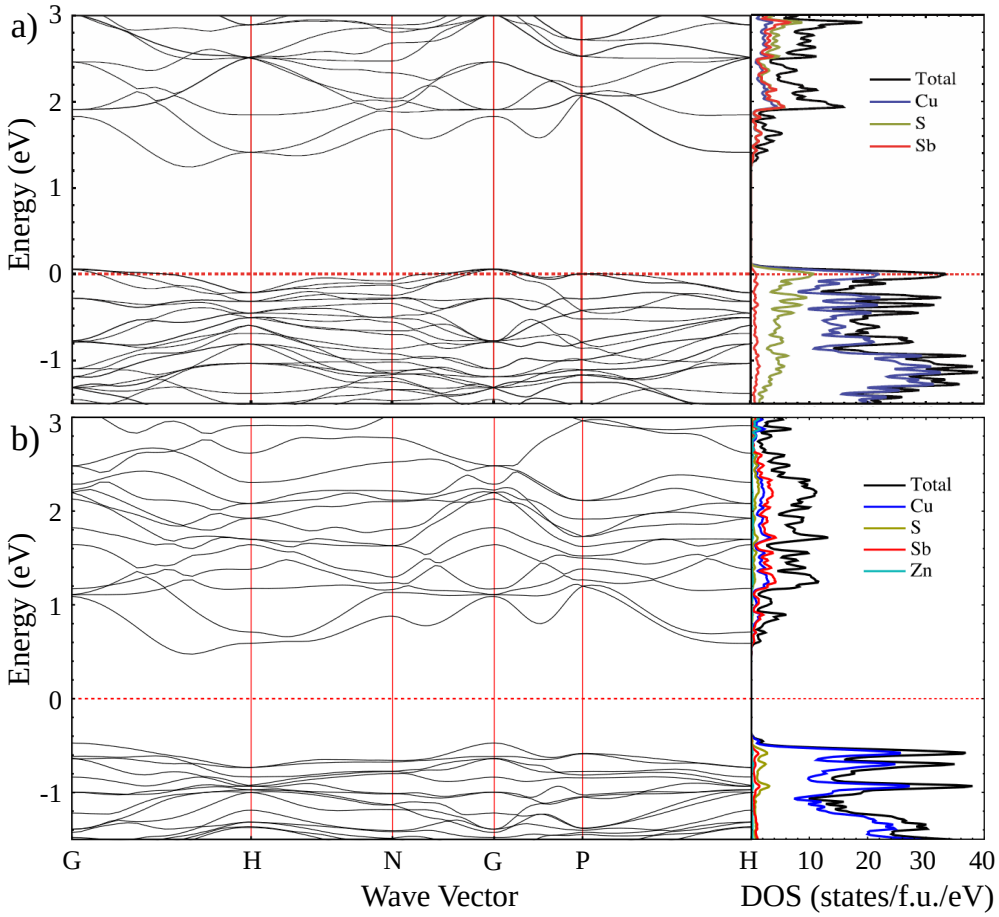

Figure 2.2: Electronic band structure and density of states (DOS) for (a) $Cu_{12}Sb_4S_{13}$ and (b) $Cu_{10}Zn_2Sb_4S_{13}$ calculated via density-functional theory.[66]

2.1.3 Lattice Dynamics

Tetrahedrite is desirable as a TE material, particularly due to its exceptionally low lattice thermal conductivity (κ_L), which approaches the minimum value predicted by theory.[34] This is partially a consequence of the large $Cu_{12}Sb_4S_{13}$ primitive unit cell volume, which causes a low κ_L via low specific heat, and the large number of atoms within the primitive unit cell gives rise to additional optical phonon modes.[71] Figure 2.3 shows the phonon dispersion of $Cu_{12}Sb_4S_{13}$ as calculated by Lu et al.[66] The transverse acoustic branches yield a high Grüneisen parameter ($\gamma > 10$) at the zone boundaries, and the three harmonically unstable optical phonon branches are associated with out-of-plane motions of Cu12e atoms. The significant lattice anharmonicity and rattler-like motion of the Cu12e atoms give rise to strong phonon-phonon scattering.

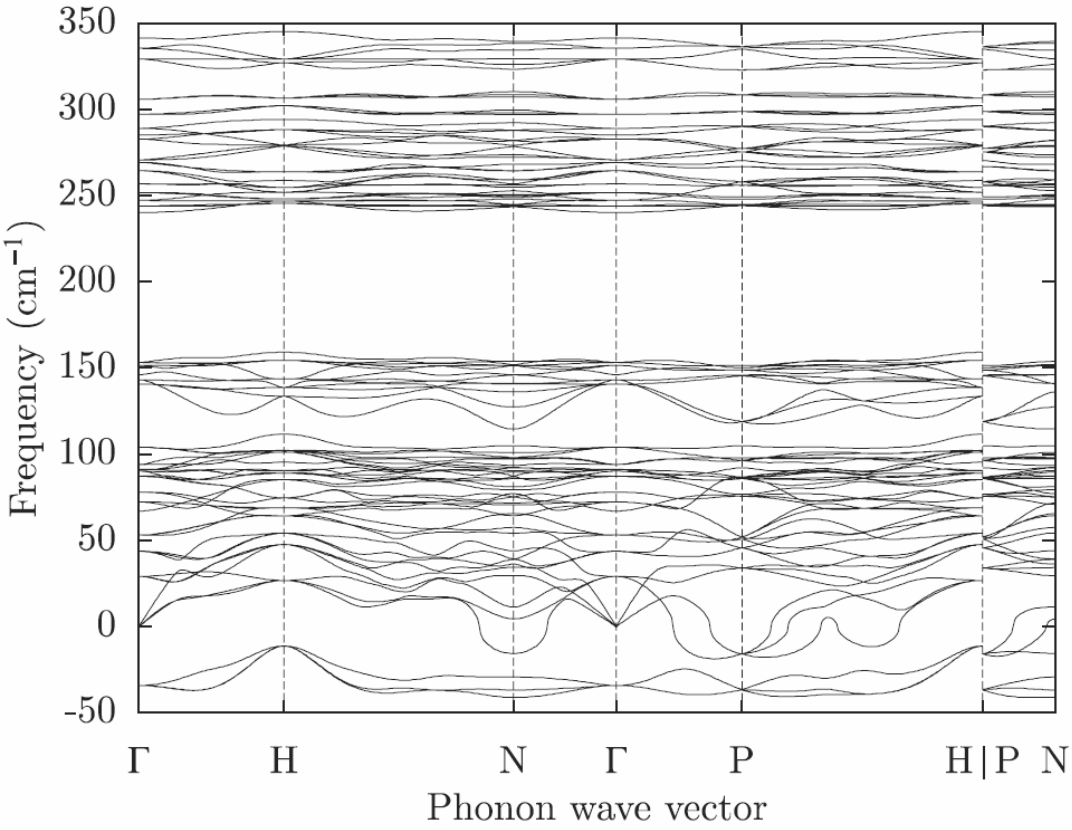

Figure 2.3: Phonon dispersion of $Cu_{12}Sb_4S_{13}$ calculated via density-functional theory.[66]

The motion of the three-fold coordinated Cu atom is a key feature of the vibrational density of states in tetrahedrites. The Cu12e has been shown to vibrate with a significantly larger atomic displacement parameter relative to the other atoms.[52, 54, 66, 72, 73] Bonding asymmetry leads to a double-well potential minima where the trigonal Cu atom energetically prefers a slightly out-of-plane position. With a recent fervor, the energetics of the rattling Cu12e atom have been explored by both computational and experimental means.[36, 60, 74–80] The calculated VDOS for the different atoms in $Cu_{12}Sb_4S_{13}$ is depicted in Figure 2.4.[54] Notice the marked low-energy, large-amplitude vibrational mode of the Cu12e atom around 4 meV. This vibrational mode acts as a site that strongly interacts with acoustic phonons, which are the primary heat carriers in the material. Hence, the significant intrinsic phonon scattering seen in tetrahedrites is closely related to the out-of-plane motion of the Cu12e atom.

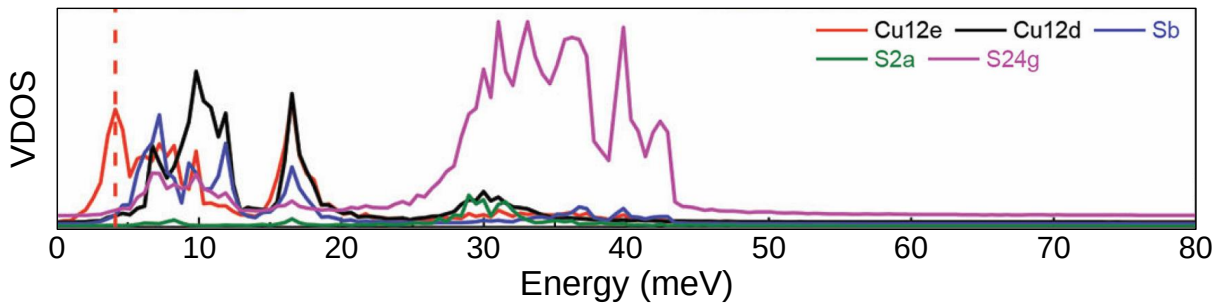

Figure 2.4: Vibrational density of states (VDOS), given in relative units at 300 K, of $Cu_{12}Sb_4S_{13}$ calculated by Lai et al. via first principles molecular dynamics. The dashed line represents vibrational modes associated with the out-of-plane vibrations of trigonally coordinated Cu atoms.[54]

The origin of the lattice anharmonicity and bonding asymmetry in tetrahedrites is linked to chemically active Sb lone pairs in the crystal structure. Since the concept of lone pair effects on lattice thermal conductivity was introduced by Skoug and Morelli in 2012, a variety of compounds, including many ternary and quaternary Cu chalogenides, have been studied

to examine the influence of lone pairs in reducing κ_L.[81–88] In 2015, Lai et al. demonstrated the importance of Sb lone pairs in engendering low κ_L in tetrahedrite.[54] It is as if lone pairs push the Cu12e atom off-center such that it exists in two equally probable locations, and the distorted coordination resembles an off-center trigonal bipyramid (denoted by the space group 48h). To further justify this visualization, a recent study show that lone pairs stress the lattice through nearest-neighbor interactions, and the Cu rattling is a way that the structure "retreats" from stress.[80] Again, computational tools have unlocked new possibilities for understanding the lattice dynamics of tetrahedrite materials. Therefore, the Sb lone pairs are an essential characteristic that cause tetrahedrites to have high thermal resistance.

2.2 Thermoelectric Properties

In general, this section will recapitulate previous TE studies involving tetrahedrite compounds. Within the past few years, TE research has gained significant momentum with respect to tetrahedrite and its many variants. Figure 2.5 summarizes the optimized ZT values obtained for tetrahedrite TEs previously. To the best of the author's knowledge, 38 studies thus far have reported ZT data for tetrahedrites, with almost all the high-temperature studies achieving values above 0.6 from 673 to 723 K. Moreover, several of these materials reached ZT beyond unity above 673 K. The 2 outlier data points, which exhibit low figures of merit even at high temperatures, are natural mineral tetrahedrite specimens. In turn, impurities in these samples lead to low TE performance. Conversely, some previous studies have achieved ZT near unity by mixing natural mineral tetrahedrites with a purely synthetic seed phase. Overall, tetrahedrites have been researched for their TE properties steadily since 2012, with even more studies focusing on other interesting phenomena in these fascinating materials.

Most of the compounds in Figure 2.5 will be mentioned in the following subsections. First, the typical Cu-based compositions will be discussed, along with Cu-enriched samples. Then, doped and substituted compounds will be summarized.

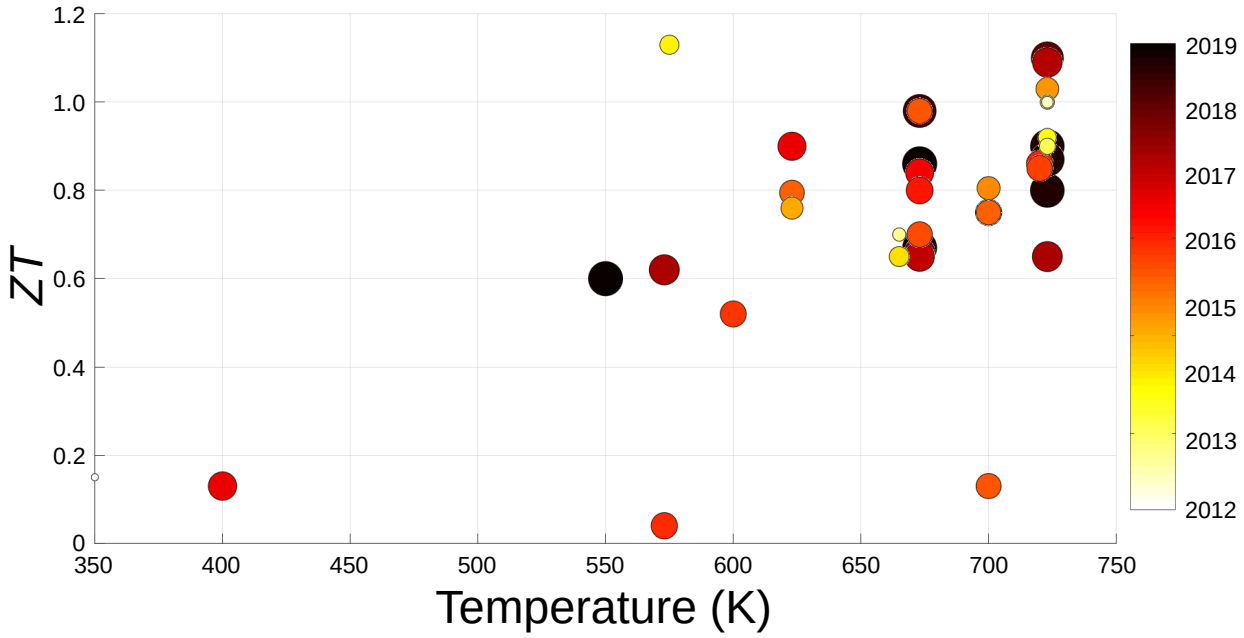

Figure 2.5: Scatter plot summarizing TE data, obtained from 38 primary research reports since 2012, for tetrahedrite compounds. The data include optimized figures of merit (ZT), the temperatures at which they were optimized, and the study's acceptance date. To enhance visual clarity, data markers are color coded and scaled by size according to date (i.e., darker/larger markers are data from more recent studies).

2.2.1 Cu-based Tetrahedrites

Cu-based tetrahedrites were some of the first compositions to be examined for TE applications, and they served as a foundational model system for future studies. In 2012, Suekuni et al. was the first to report TE properties of $Cu_{12}Sb_4S_{13}$.[55] Not long after, numerous investigations obtained ZT values up to 0.5 at 673 K for the unsubstituted composition.[66,72,73,89] More recent studies reported even higher ZT values as the process optimization for this system became more well-understood.[70, 90–94] Unfortunately, the majority of these studies

present data from samples containing impurity phases of famatinite (Cu_3SbS_4), skinnerite (Cu_3SbS_3), chalcostibite ($CuSbS_2$), copper sulfides ($Cu_{2-x}S$), or elemental Sb. Specifically, famatinite is a very common secondary phase that easily forms when synthesizing Cu-based tetrahedrites, and more often than not, TE studies of $Cu_{12}Sb_4S_{13}$ report data for samples that contain Cu_3SbS_4. Accordingly, while Cu-based tetrahedrite demonstrates good TE properties, it also has a propensity for forming impurity phases.

Cu-rich tetrahedrites have garnered significant attention in the last year or so. Although the nominal composition of tetrahedrite is denoted by $Cu_{12}Sb_4S_{13}$, the precise elemental composition and atomic distribution can vary to a large degree. For instance, Cu-based tetrahedrite stoichiometries can range from Cu-poor ($Cu_{12}Sb_4S_{13}$) to Cu-rich ($Cu_{14}Sb_4S_{13}$). The compositional variations in Cu-based tetrahedrites were studied by mineralogists and geologists well before the material was ever tried for TE applications.[95–99] In Cu-rich tetrahedrites, Cu12d sites are partially vacated and extra Cu ions reside in interstices of the lattice, creating a network of vacant tetrahedral and interstitial sites.[98] It is believed that this network enables high Cu ion mobility in tetrahedrites, but electromigration effects in tetrahedrites will be discussed further in Chapter 7 of this report. The enhanced ionic conductivity of Cu ions leads to an exsolution of two immiscible tetrahedrite phases (Cu-poor and Cu-rich). Only recently were Cu-rich tetrahedrites investigated for their TE capabilities. In 2017, Vaqueiro et al. measured the properties of $Cu_{12+x}Sb_4S_{13}$ ($0 \leq x \leq 2$) and examined the onset of Cu ion mobility as a function of temperature. It was also shown that the phase segregation in Cu-rich samples significantly reduced κ_L. Most recently, Yan et al. analyzed the properties of Cu-rich tetrahedrites, obtaining $\kappa_L = 0.25$ $Wm^{-1}K^{-1}$ and $ZT = 1$ at 723 K for $Cu_{13.5}Sb_4S_{13}$.[100] In the end, both studies demonstrated that Cu-enrichment can lead to greater ZT values, primarily through a reduction in κ_L.

2.2.2 Doped and Substituted Tetrahedrites

The massive compositional variation allowed by the crystal structure of tetrahedrite has enabled a multitude of TE investigations of various doped and substituted samples. To begin with, a wide variety of transition metals may replace Cu atoms in the structure, and such replacements have been observed in natural mineral tetrahedrites.[101] Initially, Suekuni et al. measured TE properties of transition metal (M = Mn, Fe, Co, Ni, Cu, and Zn) substituted tetrahedrites ($Cu_{10}M_xSb_4S_{13}$) up to the substitutional limit ($x = 2$).[55] In the end, $Cu_{10}Ni_2Sb_4S_{13}$ demonstrated the best ZT of all the samples reaching a max value of 0.15 at 340 K. Soon after, another group reported TE properties for fully-substituted tetrahedrites at higher temperatures.[89,102] At this point, many of the studies were guided by modern computational simulations that investigated the electronic properties of doped tetrahedrites.[67,76,77] As discussed previously, η_F lies at the valence band edge for the Cu-based composition, and adding Zn atoms, which strictly adopt a divalent state, effectively raises η_F into the gap. Accordingly, Zn acts as a dopant by contributing extra electrons to the lattice, effectively filling the holes native to the undoped composition. By leveraging this knowledge, Lu et al. demonstrated the first ZT near unity for Zn-doped tetrahedrite ($Cu_{11.5}Zn_{0.5}Sb_4S_{13}$) at 723 K.[66] Therefore, simple replacements of Cu with 3d transition metals laid the groundwork for future TE studies with tetrahedrites.

Since the early TE investigations of doping in tetrahedrite, a plethora of studies have been published for tetrahedrites doped with 3d transition metals.[70] Structural, magnetic, and TE research analyzed dopants like Mn [73], Fe [66,103–106], Co [107,108], Ni [72,109–112], Zn [36,112,113], and Cd [92] in synthetic tetrahedrites. One of the highest ZT values reported to date is that of Lu et al., which reached $ZT = 1$ at 720 K for Ni and Zn co-doped

tetrahedrite ($Cu_{10.5}NiZn_{0.5}Sb_4S_{13}$).[90] Aside from enhancements in ZT, these studies seem to indicate that dopants mitigate the formation of impurities. In fact, two studies showed explicitly that the tetrahedrite phase preferentially forms over other secondary phases when small amounts of dopant are present in the structure.[113, 114] Over the years, numerous studies have echoed a similar observation.[96, 115, 116] Thus, a vast collection of studies have shown that ZT can be significantly improved, while also stabilizing the primary tetrahedrite phase and suppressing Cu ion mobility, via doping and substituting with 3d transiton metals.

Although many studies have examined transition metal substitution in tetrahedrites, the complexity of the crystal structure allows for more exotic dopants, aside from 3d transition metals. For instance, Ge and Sn doping were recently explored, exhibiting a compositional limit of about $x = 0.6$ in $Cu_{12-x}(Ge,Sn)_xSb_4S_{13}$.[62] On another note, Ag [117] and Au [104] substitution has been shown to be possible in synthetic tetrahedrites, and Pb doping ($Cu_{11}PbSb_4S_{13}$) demonstrated ZT enhancements of about 40% at 723 K when compared to Cu-based compositions.[118] Regardless of the cost-effectiveness and toxicity of these tetrahedrites, these studies are evidence that multitudinous elemental substitutions have yet to be explored. Hence, a copious variety of elements, in addition to 3d transition metals, may be used as dopants on the Cu site in tetrahedrite, and there are many such compositions that have not been reported in the literature.

The inclusion of dopants on Sb sites has also been studied, and in certain cases, significant improvements to TE performance were observed. To begin with, Lu and Morelli synthesized $Cu_{12}Sb_{4-x}Te_xS_{13}$ ($0 \leq x \leq 1.5$), and a peak ZT value of 0.92 was obtained at 723 K for $x = 1$.[119] Following this study, Bouyrie and coworkers explored Te substitution and multi-site doping with transition metals (Cu site) and Te (Sb site).[68, 75, 108, 112, 120] In addition, doping the Sb site with Bi has been shown to yield ZT of 0.84 at 673 K in

$Cu_{12}Sb_{3.8}Bi_{0.2}S_{13}$.[121] Finally, As substitution for Sb is also possible in synthetic tetrahedrites.[104] Arsenic substitution occurs quite often in natural minerals, and indeed the mineral tennantite is simply tetrahedrite in which most or all of the Sb has been replaced by As.[122, 123] Accordingly, some compositional variation exists on the Sb site, which has been utilized to improve ZT in certain tetrahedrites.

Lastly, S site modifications in tetrahedrite materials have been researched within the last year or so. Tetrahedrite compositions with Se and Te as anions were examined in early mineralogical studies, and more recently, computational simulations predicted stable phases of the tetrahedrite structure with Se as the chalcogenide.[124, 125] In 2016, a solid-solution of $Cu_{12}Sb_4S_{13-x}Se_x$ ($0 \leq x \leq 2$) was synthesized, and a maximum ZT of 0.84 was obtained at 720 K for the $x = 1$ composition.[126] For these Se substituted compounds, researchers attribute improvements in ZT to reduced κ_L, due to increased alloy scattering of phonons. Subsequently, Cu-enrichment in $Cu_{12+x}Sb_4S_{12}Se_1$ provided even greater boosts to TE performance, obtaining ZT of approximately 1.1 at 723 K for the $Cu_{13.5}Sb_4S_{12}Se_x$ composition.[100] To the author's knowledge, this is the highest ZT reported to date for all tetrahedrite compounds. Finally, a recent study involving multi-site doping with Zn and Se in tetrahedrites was conducted investigate TE properties, and an optimized ZT of 0.86 was demonstrated at 673 K for $Cu_{11}ZnSb_4S_{12.75}Se_{0.25}$.[127] In the end, isovalent Se substitution in tetrahedrites has been shown to benefit TE properties, especially in combination with other chemical modifications.

2.3 Conventional Synthetic Approaches

Since the major focus of this work was exploring novel synthetic methods for producing tetrahedrite materials, this section will review the conventional approaches and their draw-

backs. The first subsection decsribes the traditional solid-state melt-recrystallization approach, which is employed most frequently. Tetrahedrites synthesized from natural mineral specimens will briefly be addressed with the melt-recrystallization method. Lastly, a review solution-phase approaches, including hot-injection and solvothermal syntheses, for synthesizing Cu–Sb–S materials will be provided.

2.3.1 Melt-recrystallization Synthesis

A substantial majority of tetrahedrite studies utilize a traditional melt-recrystallization approach. Figure 2.6 displays the melt-recrystallization synthesis throughout various stages of the procedure. In this approach, elemental precursors are loaded into a quartz ampule with subsequent evacuation and heating to 650 °C with a hold time of at least 12 h.[91] A slow heating rate ($\approx$ 0.3 °C min^{-1}) is a necessary precaution for preventing pressure build-up from volatilized S. The resultant ingot does not come out phase-pure, and in turn, it is subsequently ground, pressed, and annealed for up to 3 weeks at 450 °C. Finally, the sample is ground and consolidated via either hot-pressing or spark plasma sintering. Overall, long reaction times (12 to 40+ h), accompanied by a lengthy annealing phase (25 h to 3 weeks), are required to promote the formation of single-phase tetrahedrite by this method. A similar melt-spinning glass crystallization technique has been used to synthesize $Cu_{12}Sb_{3.6}Bi_{0.4}S_{10}Se_3$ ribbons, but other issues (e.g., phase purity) arose in those samples.[128] Due to long synthesis times and high energy requirements, the melt-recrystallization approach is not be amenable to large-scale applications. Therefore, more facile and less energy-intensive techniques than the traditional approach would be more favorable for commercial application of tetrahedrite materials.

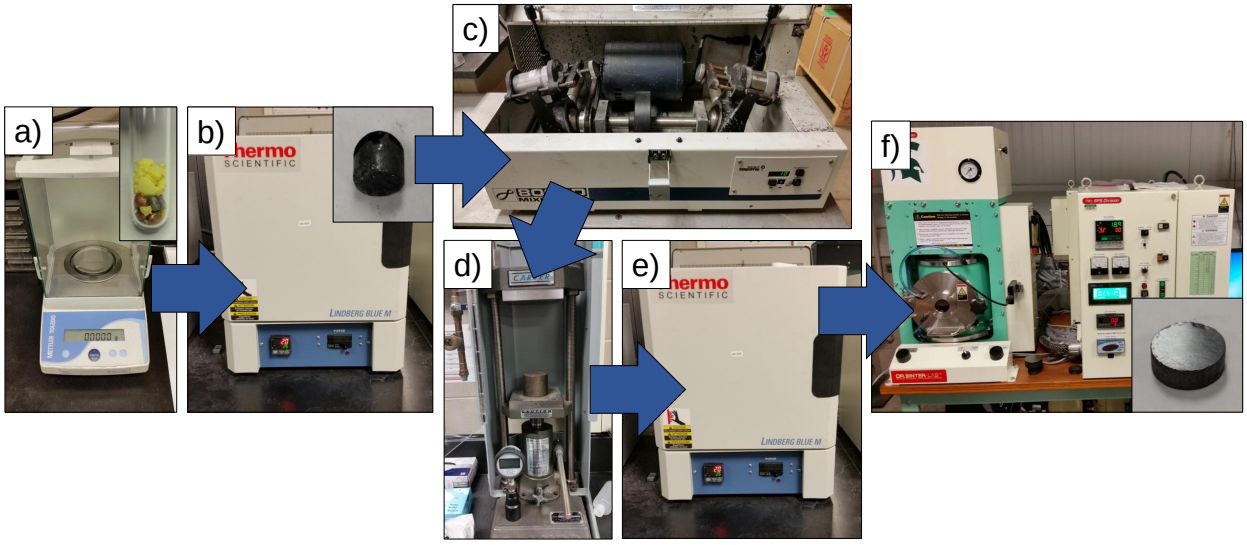

Figure 2.6: Procedure for synthesizing tetrahedrite by the conventional melt-recrystallization approach with panels depicting the (a) mass balance for weighing precursors, (b) high-temperature furnace for melting, (c) ball mill for grinding the ingot, (d) cold-press for powder consolidation, (e) high-temperature furnace for annealing, and (f) spark plasma sintering machine for powder processing. Insets display the (a) weighed elements in a 10 mm diameter quartz ampule, (b) resultant impure tetrahedrite ingot after melting/recrystallizing, and (f) dense 10 mm diameter tetrahedrite pellet for TE characterization.

It is worth briefly mentioning that synthetic tetrahedrites combined with natural mineral specimens demonstrate decent TE performance. Mineralogists and geologists were the first to study the physical properties of natural mineral specimens, and as the potential of tetrahedrite materials was realized, scientists characterized the physical properties of more natural minerals from around the world.[129,130] In fact, much of the earliest TE studies by Thomas Seebeck involved natural minerals, and Telkes expanded on this work significantly in the 1950s.[22,131] More recently, by mixing natural minerals with synthetic tetrahedrites, Lu and coworkers were able to synthesize natural mineral-based samples and characterize their TE behavior.[132–134] In this approach, synthetic tetrahedrite (made by the conventional melt-recrystallization method) acts as a seed matrix to encourage formation of pure single-phase material from natural mineral specimens (obtained from a mineral vendor). Natural

mineral-based tetrahedrites showed reduced thermal conductivity and increased electrical resistivity compared to pristine synthetic samples, and the best ZT of natural mineral-based tetrahedrites was approximately 0.9 at 723 K.[132] Although this approach is more scalable and cost-effective, natural minerals often contain trace amounts of impurities (i.e., As or Pb), which make precise compositional control difficult. Furthermore, synthetic tetrahedrites demonstrate better properties than their mineral-based counterparts, and natural mineral-based samples still rely on the conventional synthesis for the pure-phase tetrahedrite seed. Thus, natural mineral-based tetrahedrites, with relatively good TE properties, can be produced with very little refinement beyond the conventional melt-recrystallization synthesis.

2.3.2 Solution-phase Syntheses

Solution-phase syntheses boast many advantages over the conventional melt-recrystallization synthesis, but these techniques possess their own drawbacks as well. While the "top-down" melt-recrystallization approach requires high temperatures and long reaction times, "bottom-up" methodologies may be preferable because they often yield nanostructured material and require lower temperatures and shorter synthesis times. Previously, Cu–Sb–(S,Se) nanomaterials have been synthesized by a variety of wet-chemical approaches, such as hot-injection[135–140] or solvothermal [141–143] synthesis. Most notably, James et al. achieved $ZT = 0.63$ at 720 K for $Cu_{12}Sb_4S_{13}$ synthesized by the solvothermal method.[141] In a different study, the optical properties and charge generation capabilities of tetrahedrite thin films prepared from metal xanthates were examined.[144] Unfortunately, these solution-phase techniques commonly yield product on the scale of $\approx$ 100 mg per batch, and multiple batches must be combined to obtain enough material for TE characterization. Furthermore, wet-chemical approaches pose a greater risk of contamination because they often require careful

removal of undesirable byproducts. Lastly, nanoscale materials demonstrate higher reactivity due to their increased surface energy, and as a result, organic additives (i.e., ligands or surfactants) are usually employed to stabilize the material. However, previous studies provide evidence to suggest that organics can be detrimental to TE performance.[145] Therefore, solution-phase syntheses require shorter reaction times and less energy-intensive processes, but they typically utilize organics for stability and only produce small amounts of material in each batch.

Chapter 3

Experimental Methods

One major objective of this work was to investigate practical synthetic approaches with lower energy requirements, shorter synthesis/processing times, and consistently higher purity than the conventional techniques. This chapter will share details about three novel synthetic approaches for obtaining bulk samples of tetrahedrite material. All syntheses begin with production of tetrahedrite (≈2 g per sample) in powder form, followed by powder processing via spark plasma sintering (SPS) to obtain highly dense bulk samples for characterization of material properties. Furthermore, several experimental techniques are needed to study the structural and compositional behavior of these materials.[146] Lastly, quantifying ZT requires an abundance of characterization methods at low and high temperatures. Accordingly, experimental techniques for measuring the structural, compositional, electrical, and thermal properties of tetrahedrite thermoelectrics will be discussed in this chapter.

3.1 Materials Synthesis

In the following subsections, three synthetic procedures for obtaining doped and undoped tetrahedrite powders are described. The first is a solution-phase chemical synthesis method called the modified polyol process. Second, tetrahedrite may be synthesized by mechanical alloying via planetary ball milling. Finally, a reactive SPS synthesis was developed in our lab, and the procedure for producing the precursor in this synthesis will be addressed.

3.1.1 Modified Polyol Procedure

Doped and undoped tetrahedrite nanoparticles were synthesized by the modified polyol process in about 2 h of total synthesis time.[147] Chemical synthesis was done in collaboration with the Anderson research lab at Hope College in Holland, MI. Precursors of $Cu(OAc)_2 \bullet H_2O$ ($\geq$98%), $Zn(OAc)_2$ (99.99%), $FeCl_3$ (99.9%), $Sb(OAc)_3$ (99.99%), S powder (99.98%), and $NaBH_4$ (98%) were used as obtained from Aldrich Chemical Company. Tetraethylene glycol (TTEG, 99%, Alfa Aesar) was used as the solvent, and anhydrous ethanol (EtOH, 200 proof, Pharmco-Aaper) was used for washing and removing contaminants from the final powder.

Figure 3.1 shows the modified polyol process throughout various steps in the reaction, and glassware photos were obtained from Andrew Ochs with permission. Metal salts and S powder were transferred to a 1 L round-bottom flask in their stoichiometric ratios. For Cu-based tetrahedrite, only $Cu(OAc)_2 \bullet H_2O$ was used as a reactant. $Zn(OAc)_2$, $FeCl_3$, and many other metal salts may be used as precursors for obtaining doped tetrahedrites by this solution-based approach. Next, TTEG (200 mL) was added to the flask, the mixture was stirred with a magnetic stirbar to dissolve reagents, and then the solution was sparged under N_2 gas for 10 min. $NaBH_4$, a strong reducing agent, was weighed out in excess (4 g) and dissolved in 100 mL of tetraethylene glycol. The resulting sodium borohydride solution was slowly added to the round-bottom flask, and the color of the solution immediately darkened upon addition of the reducing agent. The reaction was then heated to 220 °C and held for 1 h with a positive N_2 flow. Subsequently, the heat was removed, and the reaction was allowed to cool to room temperature. The mixture was loaded into 50 mL centrifuge tubes and centrifuged at 5000 rpm for 10 min, followed by washing with EtOH, sonication,

and centrifuging again. This washing procedure was repeated at least three times before the final product was dried overnight in a vacuum dessicator. The resulting $Cu_{12}Sb_4S_{13}$ powder appeared as an opaque black color, whereas the final $Cu_{11}ZnSb_4S_{13}$ powder was dark brick-red.

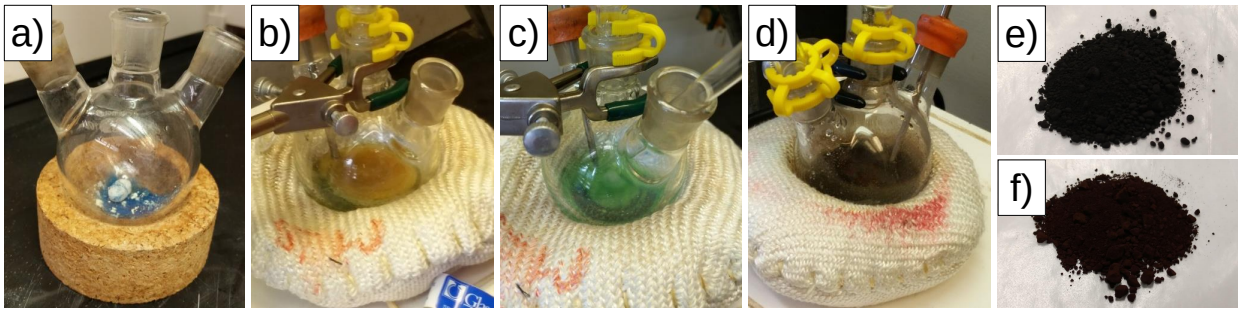

Figure 3.1: Photos of tetrahedrite synthesis by modified polyol process (a) after addition of metal salts and S powder, (b) while precursors mix with tetraethylene glycol, (c) after sparging with N_2 for 10 min, and (d) after reacting at 220 °C for 1 h. The final powder products of $Cu_{12}Sb_4S_{13}$ and $Cu_{11}ZnSb_4S_{13}$ are shown in (e) and (f), respectively.

3.1.2 Mechanical Alloying Procedure

The mechanical alloying procedure is a scalable and highly reproducible method for synthesizing tetrahedrite powder via planetary ball milling.[148] The following approach was adapted from Barbier et al.[109] Powders of Cu (99.9%), Ni (99.9%), Zn (99.9%), Sb (99.5%), and S (99.5%) were used as obtained from Alfa Aesar. Elemental powders were loaded according to their stoichiometric ratios into a 50 mL agate milling jar with 8 agate grinding balls (10 mm diameter). Precusors of Ni, Zn, Fe, Co, and other transition metals may be used when doping on the Cu site. Reactants were milled at 300 rpm for 48 h (1 min cooldown every 30 min) in a Retsch PM-100 planetary ball mill (shown in Figure 3.2). The mill was housed in an Ar glovebox such that no oxidation to place during the reaction. Lastly, the jar was removed and allowed to cool before extracting the resultant tetrahedrite product.

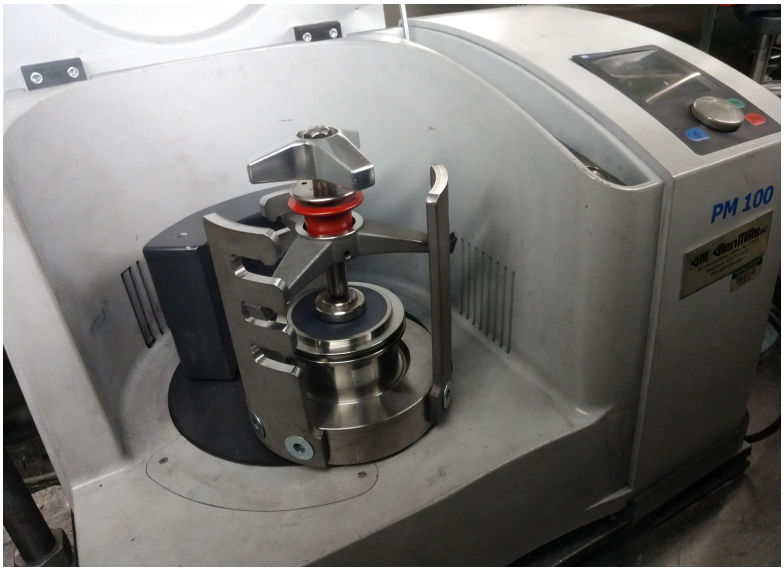

Figure 3.2: Planetary ball mill used for synthesis of tetrahedrite by mechanical alloying.

3.1.3 Reactive Spark Plasma Sintering Procedure

In our lab, we developed a reactive SPS synthesis that combines a short ball milling step with an extended SPS procedure to yield tetrahedrite in less than 2 h.[148] This subsection will explain the procedure for creating the "intermediate precursor" via vibratory ball milling, and the SPS procedure for generating the final tetrahedrite product from the intermediate precursor will be described later in subsection 3.2.3. Elemental powders and binary precursors of CuS (99.8%), Cu_2S (99.5%), Cu (99.9%), Ni_3S_2 (99.9%), ZnS (99.99%), and Sb_2S_3 (99.999%) were used as received from Alfa Aesar. The reagents were added to a 50 mL stainless steel ball mill jar containing two 10 mm diameter and four 5 mm diameter stainless steel grinding balls. The jar was filled with Ar and sealed to prevent oxidation of reactants. Subsequently, the mixture was milled at 1080 rpm for 1 h in a SPEX 8000D vibratory ball mill (shown in Figure 3.3). Upon completion, the ball mill jar cooled ambiently to room temperature before removing the intermediate precursor powder. This product typically contains a seed tetrahedrite phase, along with impurity phases and unreacted precursors.

Figure 3.3: Vibratory ball mill used to prepare the intermediate precursor for synthesis of tetrahedrite by reactive spark plasma sintering.

3.2 Powder Processing

Powders obtained from the three synthetic approaches discussed above were consolidated and refined via SPS. This technique effectively utilizes pressure and joule heating (induced by a pulsed DC electric current) to fabricate dense pellets from powder precursors. SPS is a relatively new method that boasts advantages over conventional hot pressing such as shorter sintering times, lower power consumption, and more precise control over sintering parameters.[149, 150] Furthermore, the rapid nature of this densification technique inhibits grain coarsening and enables facile maintenance of nanostructuring in samples. A Calnano 211-LX Dr. Sinter spark plasma sintering machine (shown in Figure 3.4(a)) with a type-K thermocouple and DAS software was used for all SPS procedures in this report. Initially, powders were loaded into a 10 mm graphite die and mounted between two electrodes inside the SPS chamber (see Figure 3.4(b)). After processing via SPS, a highly dense cylindrical puck, like that displayed in Figure 3.4(c), was obtained.

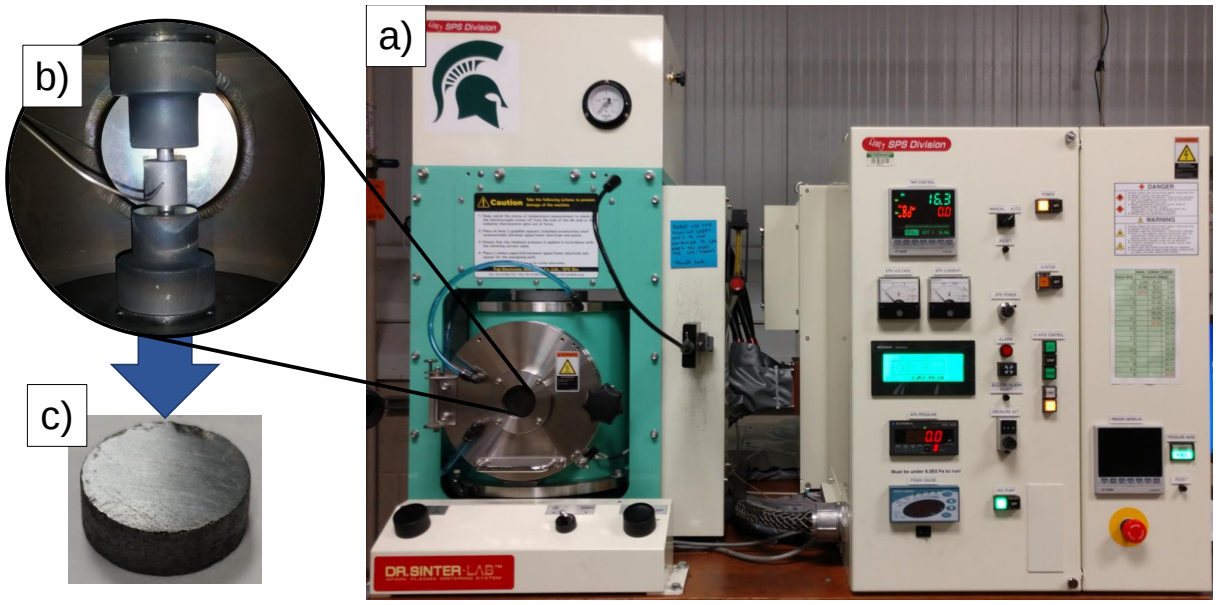

Figure 3.4: (a) Spark plasma sintering machine used for processing tetrahedrite powder; (b) SPS viewing window where a 10 mm graphite die is mounted between two electrodes; (c) densified puck (10 mm diameter) obtained from powder processing.

Through process optimization, it was found that similar sintering conditions could be used for all three synthetic approaches. All samples were held under 40 MPa of uniaxial pressure in a vacuum-purged atmosphere for the entire SPS process. Initially, a two-step SPS procedure was used for the samples synthesized by the modified polyol process. Figure 3.5(a) shows the details regarding ramp rates for this procedure, henceforth termed SPS profile A. In the first step, tetrahedrite powder was sintered at 300 °C for 10 min to remove residual organics leftover from the chemical synthesis, and then the sample was cooled naturally to room temperature by turning off the SPS power. The resulting pellet was sanded to remove surface graphite, milled for 5 min via vibratory ball milling, and sintered for another 10 min at 350 °C to achieve high density. After the first sintering step, a density of ≈85% was achieved, but by the end of SPS profile A, all sample densities exceeded 92% of the theoretical value. For the mechanical alloying approach, the first step of SPS profile A was omitted and samples were simply sintered at 350 °C for 10 min. For the reactive SPS samples, sintering

was carried out at 350 °C for 30 min, with extra sintering time given to allow intermediate precursor to react completely and form single-phase tetrahedrite.

Later in our optimization, additional ethanol washes (after the chemical synthesis) were performed to eliminate the need for a multi-step sintering procedure like that described previously. Thus, the single-step SPS profile B was developed (depicted in Figure 3.5(b)); tetrahedrite powder was sintered at 400 °C for 10 min to achieve densities above 93 %. This temperature was found to be optimal for producing highly dense bulk samples, while also mitigating brittleness that resulted from sintering at higher temperatures. Ultimately, SPS profile B provided the best sintering conditions for obtaining dense pellets from all three synthetic approaches discussed in this report.

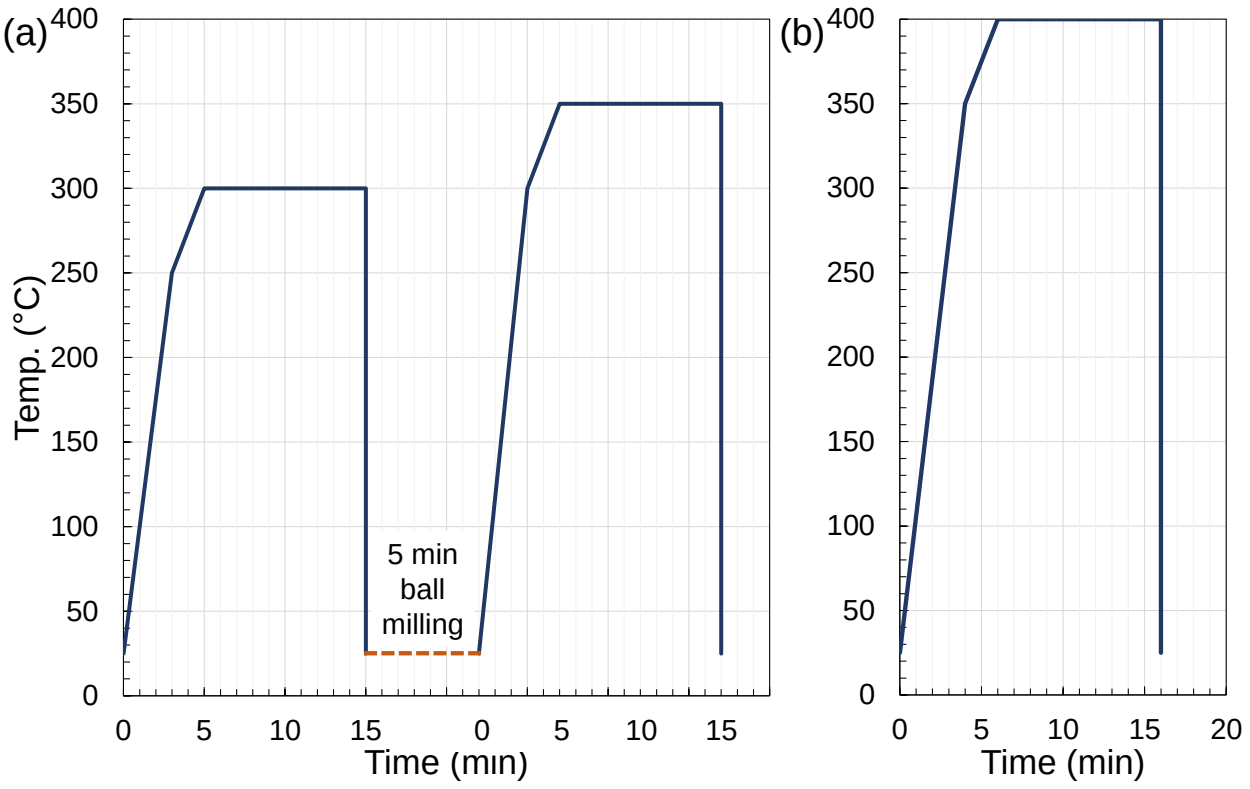

Figure 3.5: Spark plasma sintering temperature profiles for (a) SPS profile A and (b) SPS profile B used in the processing of tetrahedrite powder.

3.3 Materials Characterization

Following powder processing, some sample preparation was required before analyzing the material properties. The pellet obtained from sintering was sanded to remove surface graphite and polished with fine-grit sand paper. Subsequently, room temperature density of the pellet was measured by a geometric approach and by Archimedes' method. In general, higher density is desirable for the most accurate determination of material properties, and all of the samples discussed in this report were at least 92% dense, with many of the samples being greater than 95% of the theoretical value. Next, the sample was cut with a diamond saw apparatus, such that a thin disc (≈1 mm thick, 10 mm diameter), 2 rectangular prisms (roughly 3×3×7 mm^3), and 4 rounded edge pieces were obtained. These pieces were to be used for the various characterization techniques described in the following subsections.

3.3.1 Structural and Compositional Analysis

X-ray diffraction (XRD) is a common materials science technique that utilizes X-ray scattering to probe the crystal structure and phase of a material.[151] X-rays are electromagnetic radiation with wavelengths on the order of the distance between atomic planes in a crystal. When incident X-rays strike a crystal, they scatter off the atoms in the material. Diffraction occurs due to the periodicity of the lattice, and a diffraction pattern with regularly spaced areas of constructive and destructive interference will result. Constructive interference (i.e., a Bragg reflection) occurs according to Bragg's Law (Equation 3.1), where d is the distance between atomic planes, θ is the angle of incident X-rays, n can be any integer, and λ is the wavelength of the incoming radiation beam.

$$2d\sin\theta = n\lambda \tag{3.1}$$

The interatomic spacing (d_{hkl}) for a cubic system may be calculated by Equation 3.2, where a is the lattice constant and (hkl) are the Miller indices for a given plane.

$$d_{hkl} = \frac{a}{\sqrt{h^2 + k^2 + l^2}} \tag{3.2}$$

In XRD, Bragg reflections are measured with a detector and indexed to their corresponding crystal planes. From the XRD profile, one can ascertain information regarding the interatomic spacing, lattice constant, crystallite size, and strain in the lattice.

Edge pieces of the sample pellet were ground by mortar and pestle, and measurements were taken with a Rigaku Miniflex-II benchtop diffractometer via Cu K_α radiation (30 kV and 15 mA). Figure 3.6(a) displays the XRD instrument, and Figure 3.6(b) shows tetrahedrite powder mounted to a glass XRD slide inside the XRD chamber. In order to calculate lattice parameter, a Si standard was added to the powder and it was scanned again to account for any offset due to the height of powder on the XRD slide. The reference XRD pattern for tetrahedrite, obtained from Wuensch, is presented in Figure A1 of the Appendix.[51]

In addition to XRD, electron microscopy is another useful approach for visualizing and analyzing the structural properties of a material. In electron microscopy, an electron beam with a set energy (keV scale) is accelerated toward a sample and scattered or transmitted in a variety of ways. When incident electrons are inelastically scattered, low-energy secondary electrons are produced. In scanning electron microscopy (SEM), secondary electrons are detected to form a microscopic image of the surface of a sample. Another form of imaging that is particularly useful for imaging the morphology of nano-scale materials is transmission electron microscopy (TEM). Here, incident electrons are transmitted through a material and detected to form an image of the sample with nanometer resolution. These electron

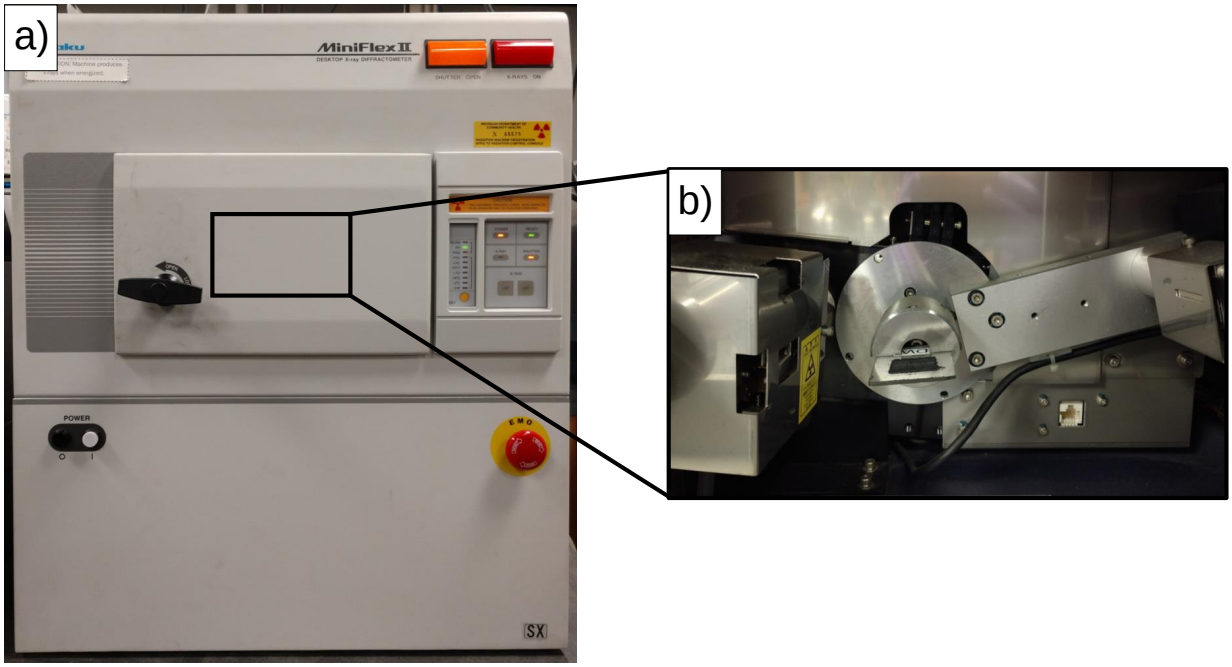

Figure 3.6: (a) Bench-top X-ray diffractometer for analyzing crystal structure and phase and (b) tetrahedrite powder mounted to a glass slide inside the diffractometer chamber.

microscopy techniques are used for two main purposes in our lab: (1) to confirm the particle size of powders synthesized by the modified polyol method and (2) to measure grain size in sintered TE materials.

To prepare for SEM characterization, powders obtained from chemical synthesis or edge pieces of sintered samples were mounted onto carbon tabs adhered to aluminum SEM stubs. Two high-resolution SEM instruments were used to characterize samples presented in this report. The first, located in the Center for Advanced Microscopy at MSU, was a JSM-JEOL-6610LV SEM with a tungsten hairpin emitter and an accelerating voltage of 15 kV. The second instrument, owned by JEOL USA Inc., was a JEOL JSM-7200F-LV field emission microscope with an accelerating voltage of 2 kV. For both instruments, SEM images were obtained via the in-lens detector. For TEM characterization, dilute nanoparticle solutions in ethanol were drop-cast onto a Ni TEM grid (formvar/carbon 400 mesh). TEM analysis was performed using a Tecnai G2 20XTWIN and an accelerating voltage of 80kV. TEM work was

performed as a collaboration with the Pennsylvania State University chemistry department.

Elemental analysis is commonly performed by energy dispersive X-ray spectroscopy (EDS). Typically, EDS instruments are attached or combined with SEMs, since they are both capable of using a beam of electrons as the probing source. In addition to secondary electrons, characteristic X-rays will be emitted from a material upon interacting with the incident electron beam. Characteristic X-rays can be detected to provide information about the atomic composition of microscopic regions in a material. EDS samples were prepared in the same way that SEM samples were prepared. In the Center for Advanced Microscopy at MSU, EDS was performed with an Oxford Instruments Aztec system (software version 3.1, 15 kV accelerating voltage) with a 20 mm^2 Si drift detector. At Hope College, EDS data was collected with a Hitachi TM-3000 Tabletop Microscope (15 kV accelerating voltage) and a Bruker XFlash MIN SVE detector/scan generator. When determining the chemical composition of a sample, EDS data was averaged over three sites and atomic ratios were normalized to have 13 S atoms per formula unit. Overall, EDS allows characterization of the chemical composition, elemental distribution, and phase homogeneity of a material.

3.3.2 Low-temperature Transport Property Analysis

Although tetrahedrite demonstrates enhanced TE properties at intermediate temperatures (400–700 K), low-temperature measurements provide fundamental information about samples being investigated, as well as comparative measurements for high-temperature properties in the overlapping temperature range (300–350 K). A home-built liquid nitrogen cryostat, depicted in Figure 3.7a, was used to measure TE properties from 80-350 K (ΔT = 10 K). Ultimately, this instrument is capable of characterizing electrical conductivity, thermopower, and thermal conductivity with uncertainties of approximately 5%, 5%, and 10%, respectively.

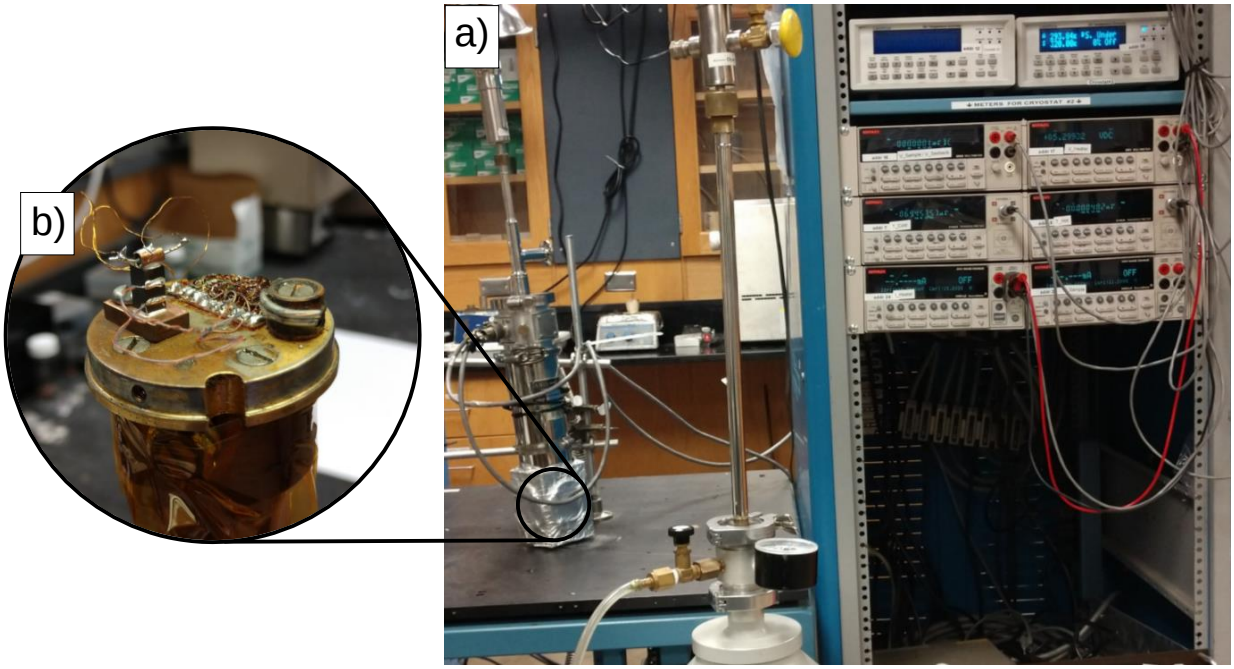

Figure 3.7: (a) Liquid nitrogen cryostat for thermoelectric characterization from 80 to 350 K and (b) a tetrahedrite sample mounted to the cryostat stage with electrical probes in place.

One of the rectangular prisms obtained from cutting the sample was used for low-temperature TE property characterization. The sample was mounted on a stage assembly (see Figure 3.7b); it was fixed to a Cu base on bottom and an 800 Ω resistor (i.e., resistive heater) on top via Ag epoxy. The resistor was wrapped in Cu foil, and small Cu strips were epoxied to the side of the sample. Subsequently, contacts were soldered to the sample, both ends of the resistor, and the top and bottom of the assembly. Figure 3.8 depicts a schematic of the cryostat assembly with various electrical contacts, sample dimensions, and signal data labeled. In particular, two constantan-Cu contacts were attached to the face of the sample, with a separation of about 2 mm. The set-up was placed in the cryostat instrument and subsequently evacuated to a pressure $\leq 1 \times 10^{-5}$ torr before undergoing characterization. During measurement, a LakeShore 311 temperature controller was used to adjust the temperature of apparatus with a steady-state hold time of 20 min per data point.

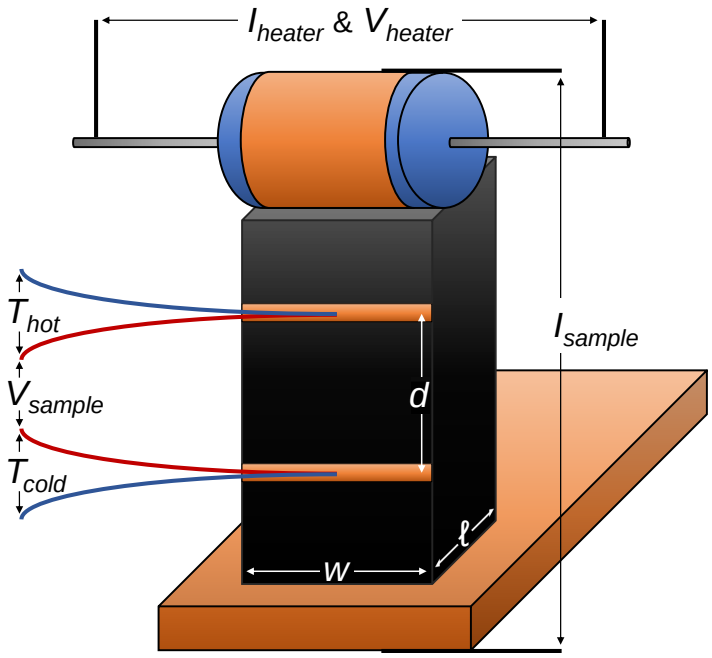

Figure 3.8: Schematic of tetrahedrite sample mounted to the cryostat stage assembly.

According to Ohm's Law ($V = IR$), electrical resistance (R) is obtained by providing a current (I_{sample}) and measuring the voltage difference across the material (V_{sample}).[18] The cross-sectional area (A) is the product of sample width (w) and length (ℓ). For an assembly with probe separation (d), electrical resistivity (ρ) may be calculated by Equation 3.3.

$$\rho = R_{sample}\left(\frac{A}{d}\right) = \frac{V_{sample}}{I_{sample}}\left(\frac{w\ell}{d}\right) \tag{3.3}$$

To establish a temperature gradient across the sample, a current (I_{heater}) is passed through the resistor for 10 min. Typically, I_{heater} is chosen such that a temperature difference of ≈1.5 K between the probes would be expected. Thermopower (S) is obtained from dividing the voltage difference (V_{sample}) by the temperature difference ($\Delta T = T_{hot} - T_{cold}$) between probes, as shown in Equation 3.4.

$$S = \frac{V_{sample}}{\Delta T} \tag{3.4}$$

While in principle the measured TE voltage must be corrected for the thermopower of the contacts, in practice, this correction is less than 1% and is therefore ignored. If all the power ($P_{heater} = I_{heater}V_{heater}$) generated by the resistor goes towards heating the sample, then the uncorrected thermal conductivity (κ^*) is found by Equation 3.5.

$$\kappa^* = \frac{P_{heater}}{\Delta T}\left(\frac{d}{A}\right) = \frac{I_{heater}V_{heater}}{\Delta T}\left(\frac{d}{w\ell}\right) \tag{3.5}$$

Although error due to conduction and convection is reduced by the low-vacuum atmosphere, a significant portion of the power generated by the resistor is given off as radiation. Thus, κ^* is converted to thermal conductance ($K^* = \kappa^*\,(A/d)$) and modified by subtracting a corrective factor derived from the Stefan-Boltzmann law. The previous calculation yields the radiation-corrected thermal conductance (K), which easily be converted to the final radiation-corrected thermal conductivity (κ) by Equation 3.6.

$$\kappa = K\left(\frac{d}{A}\right) = \left[K^* - \left(0.00146\ \text{W K}^{-1}\right)\left(\frac{T^3}{300}\right)\right]\left(\frac{d}{w\ell}\right) \tag{3.6}$$

3.3.3 High-temperature Transport Property Analysis

For high-temperature electrical property characterization, the second rectangular prism was measured in an Ulvac ZEM-3 instrument, portrayed in Figure 3.9a. Dimensions of the sample were measured before mounting it between two graphite electrodes (see Figure 3.9b). Two probes were spring-loaded against the sample at a defined separation distance, and the set-up was encased in a metallic heat shield equipped with a thermocouple. Then, the chamber was closed and purged 3 times for 5 min via vacuum pump and Ar backfilling. In the end,

ZEM measurements provide electrical conductivity and thermopower data from 300 to 723 K (ΔT=50 K) with uncertainties of about 5% for both properties.

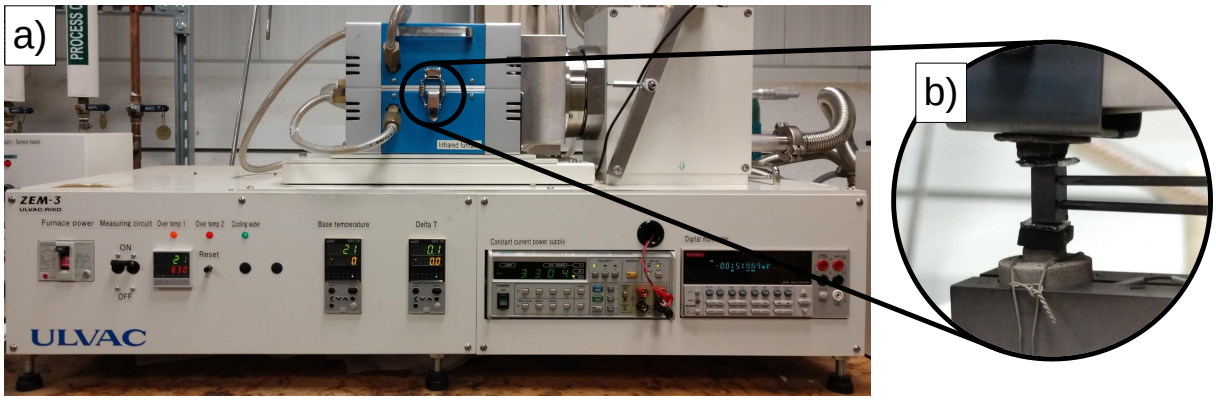

Figure 3.9: (a) Ulvac ZEM-3 instrument for high-temperature electrical properties characterization and (b) a tetrahedrite sample mounted on the ZEM with contact probes in place.

The thin disc obtained from cutting was polished with fine-grit sandpaper, measured for thickness via calipers, and coated with graphite before undergoing characterization by laser flash analysis (LFA). In collaboration with the ECE department at MSU, a Netzsch LFA-457 instrument was used to measure thermal diffusivity (α) from 323 to 723 K in an Ar atmosphere with a pyroceram reference. Equation 1.27 was used to calculate the total thermal conductivity (κ) from these measurements. Tetrahedrites have been shown to demonstrate C_p equivalent to the Dulong-Petit value over a wide temperature range, and this value was used when calculating κ at high-temperature.[66] Overall, this method provides thermal conductivity data with an uncertainty of $\approx$ 10%.

For both low-temperature (cryostat) and high-temperature (LFA) measurements, lattice thermal conductivity (κ_L) data is obtained by subtracting the electronic thermal conductivity (κ_e) component from the total thermal conductivity (κ_{total}), as dictated by the Wiedemann-Franz law (Equation 1.31). However, the degenerate limit, in which the Lorenz number (L) is equal to 2.44×10^{-8} WΩK^{-2}, is not an adequate assumption in the case

of most tetrahedrite materials. Instead, we use the approach suggested by Kim et al. to estimate L from measurements of thermopower (S), as shown by Equation 3.7.[152]

$$L = 1.5 + \exp\left(\frac{-|S|}{116}\right) \tag{3.7}$$

The above equation is used to estimate $L \times 10^{-8}$ WΩK^{-2} for every data point. Then, L values are averaged for each sample and the average is used for calculations of κ_e. Typically, L equates to approximately 1.8×10^{-8} WΩK^{-2} for the tetrahedrites reported in this thesis.

Chapter 4

Modified Polyol Synthesis

Solution-phase techniques have been used to synthesize tetrahedrite compounds in the past, but many of them have disadvantages like small batch sizes (100 mg scale) or the use of organics for stabilization. The investigations detailed in this chapter describe a novel synthetic approach, termed the modified polyol process, for obtaining terahedrite nanomaterial with no residual organics. In this method, synthesis and processing times sum to about two hours, relatively low reaction temperatures are needed, and a wide variety of compositions may be synthesized. Furthermore, the synthesis has been shown to be easily scalable up to 2 g per batch, with potential for even greater scalability. The modified polyol process is advantageous over conventional methods because it is facile and versatile, while also obtaining tetrahedrite with comparable or better TE properties.

First, some background on polyol syntheses will be covered. Then, research findings for several different tetrahedrites fabricated by this method will be disseminated. All tetrahedrites synthesized by the modified polyol process were produced in collaboration with the Anderson Chemistry Lab at Hope College. Material properties and TE data will be reported for Cu-based ($Cu_{12}Sb_4S_{13}$), Zn-doped ($Cu_{11}ZnSb_4S_{13}$), and Fe-doped ($Cu_{12-x}Fe_xSb_4S_{13}$, $x = 1$ and 1.5) tetrahedrites. Intermittently, some background information will be provided for Fe-doped tetrahedrites as well, since these compositions demonstrate unique mixed-valence states not observed in other tetrahedrites.

4.1 Background on Modified Polyol Process

The polyol method is a relatively nascent solution-phase technique for synthesizing metallic, intermetallic, and organometallic compounds. The process was pioneered about three decades ago, when polyalcohols were used to reduce metals that are easily oxidized like Cu, Co, and Ni.[153] Metal industries found the polyol process favorable because of its simplicity, limited use of raw precursors, and relatively low toxicity reactants/products. In addition, polyol reactions offer precise control over particle size and morphology, allowing for use in specialized applications. Over the years, these methods were refined to synthesize an encompassing variety of metal nanoparticles for various technical applications (e.g., energy storage, catalysis, coatings, etc.). Previously, numerous TE materials have been synthesized by the polyol process. Recently, many state-of-the-art TE materials have been successfully produced by this method, including bismuth tellurides/selenides [154–156], bismuth antimony chalcogenides [157, 158], lead tellurides [159], and skutterudites [160–163]. Accordingly, the polyol process is quite versatile in its capabilities to synthesize a broad range of materials for widespread applications.

The procedure for synthesizing materials by the polyol process is relatively simple and straightforward. In general, the reaction begins by dissolving metal salts in a high boiling point (b.p. $\approx$ 200–300 °C) alcohol, which allows for higher reaction temperatures than other solution-phase methodologies. Upon heating, the polyalcohol solvent oxidizes, eventually to monomeric CO_2, and donates electrons to metal salt complexes. The resultant metallic species are highly reactive, and they diffuse easily in the solution to nucleate and form metal particles. The particles are then extracted from the solution via centrifuging or capped and suspended in solution. Candidate materials to be made by the polyol process are deter-

mined by their reduction potential relative to the reduction potential of the polyalcohol. While the polyol acts as a reducing agent to form the desired product, it also acts as a solvent that prevents the oxidation of these products. Moreover, a strong reducing agent, such as $NaBH_4$, may be used to modify the process (i.e., the "modified polyol process") and enhance the possibilities for reducible precursors. Process optimization requires careful consideration of reaction temperature, precursor ratios, total reaction scale, and contamination sources. Accordingly, these reactions are run under an inert atmosphere via traditional Schlenk techniques. Therefore, the polyol process is a simple solution-phase procedure with a wide range of possible modifications.

We use the modified polyol process to synthesize tetrahedrite compounds, and a schematic of the simplified chemical reaction is shown in Figure 4.1. Much of the process optimization and procedural details were determined by Stevens.[164] Tetraethlyene glycol (b.p. = 314 °C) is the polyalcohol used in the reaction, with sodium borohydride added to enhance the reduction potential of the solution. For Cu-based tetrahedrite, the reactants comprised copper(II) acetate monohydrate, antimony(III) acetate, and elemental sulfur. As aforementioned in Chapter 3, a variety of metal salts could be added to dope the material. The reaction runs at 220 °C for 1 h, and multiple chemical intermediates form as the polyalcohol and metal salts undergo redox.[164] In the end, tetrahedrite forms as a final product with various byproducts leftover including organics (oxidized or unreacted polyalcohol), soluble sodium salts (sodium acetate), and borane molecules. The final product is reclaimed via centrifuging and washing away byproducts with ethanol. Ultimately, enough stable nanoscale tetrahedrite powder is obtained for TE characterization in a single-batch synthesis. Therefore, the modified polyol procedure is applicable to a wide range of tetrahedrite compositions.

$$\_H(OCH_2CH_2)_4OH + \_Cu(OAc)_2{\bullet}H_2O + \_Sb(OAc)_3 + \_S + \_NaBH_4$$

$$\Rightarrow \_Cu_{12}Sb_4S_{13} + \_Na(OAc) + \_BH_3 + \_Organics$$

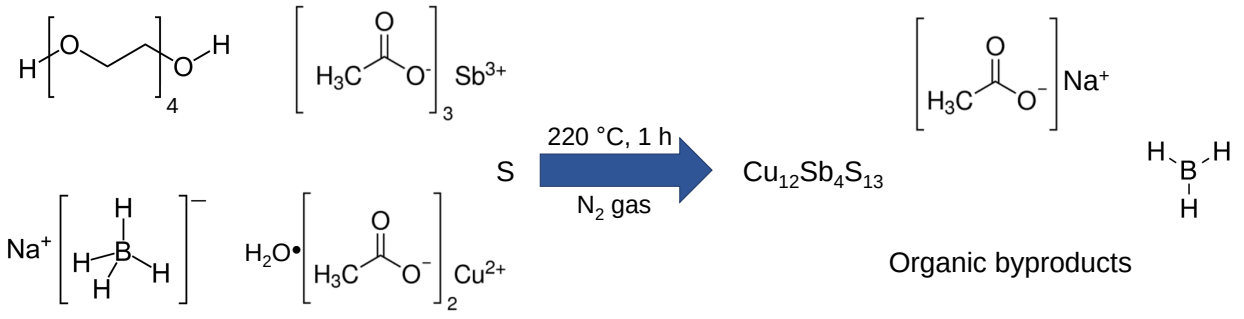

Figure 4.1: Generalized chemical equation and reaction schematic detailing the modified polyol process for synthesizing tetrahedrite material. Reactants are tetraetylene glycol, copper(II) acetate monohydrate, antimony(III) acetate, elemental sulfur, and sodium borohydride. Products are copper-based tetrahedrite, sodium acetate, borane, and organic byproducts (e.g., tetraethlyene glycol, carbon dioxide, etc.).

The reaction temperature of 220 °C was determined to be optimal for forming high-purity tetrahedrites.[164] Through process optimization, it was found that lower reaction temperatures yield copper sulfides and famatinite. For example, when the reaction was held at 180 °C, Cu_2S and CuS were obtained, and at 200 °C Cu_2S and Cu_3SbS_4 were produced. This was also the case when reactions were carried out at 220 °C for 45 min or less. On the other hand, with reaction temperatures of 240 ° and 250 °C, numerous different products formed including Cu_2S, $CuSbS_2$, Sb, and Sb_6O_{13}. Tetrahedrite is the only product that forms when running the reaction at 220 °C for 1 h.

4.2 $Cu_{12}Sb_4S_{13}$ and $Cu_{11}ZnSb_4S_{13}$

The initial tetrahedrite samples synthesized by modified polyol process were $Cu_{12}Sb_4S_{13}$ and $Cu_{11}ZnSb_4S_{13}$ tetrahedrites. The literature database for these compositions is quite expansive, enabling simple comparison between nanostructured samples and their bulk counter-

parts. Furthermore, Zn was chosen as a dopant for pioneer studies owing to its effectiveness in improving TE performance. In addition to some unpublished data, much of this section details the findings from the *Chemistry of Materials* article by Weller et al.[147] The following subsections will promulgate the first TE characterizations of tetrahedrites synthesized by the modified polyol process.

4.2.1 Analysis of Pre-processed Powders

Powder X-ray diffraction (XRD) profiles of the as-synthesized powders are shown in Figure 4.2. Single-phase tetrahedrite was obtained for both the Cu-based sample and the Zn-doped sample. While other synthetic methods benefit from a dopant to stabilize the tetrahedrite phase, the modified polyol process can produce pure Cu-based tetrahedrite with no secondary phases and without the inclusion of dopants.

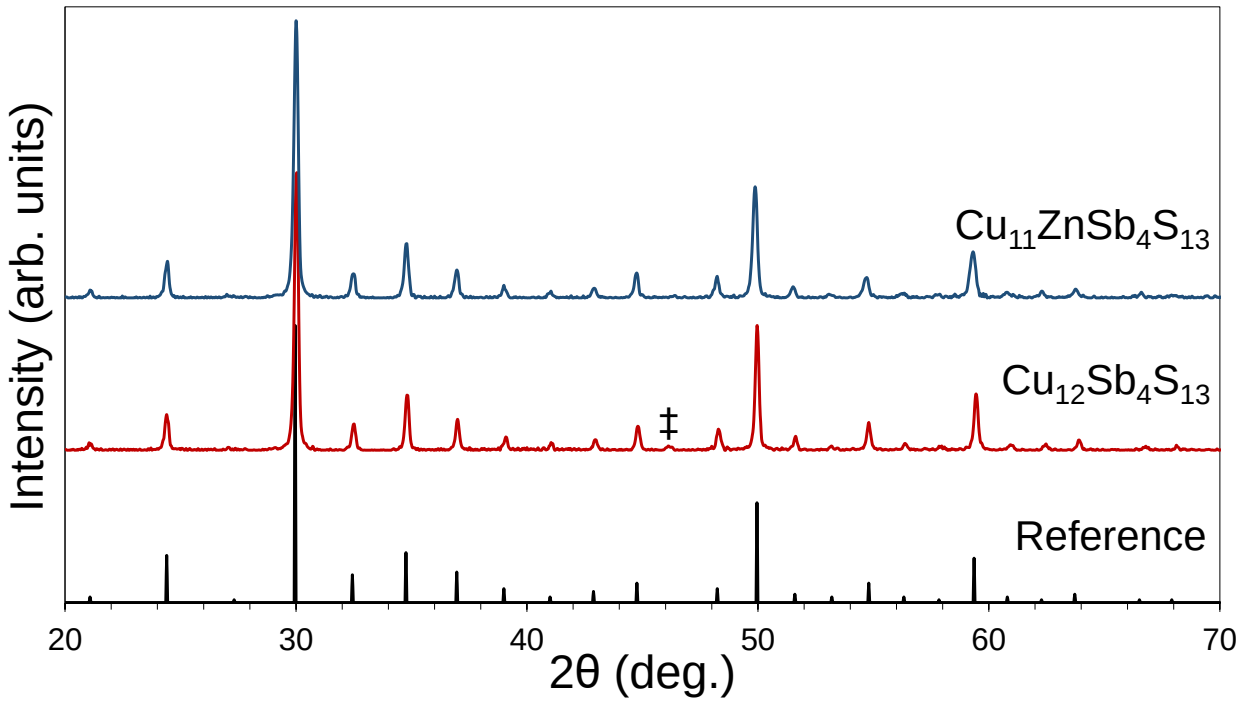

Figure 4.2: X-ray diffraction profiles of $Cu_{12}Sb_4S_{13}$ and $Cu_{11}ZnSb_4S_{13}$ synthesized by modified polyol process (pre-processing). An impurity peak of Cu_2S is marked by a ‡ symbol.

Electron microscopy was conducted to probe the size, morphology, and dispersity of tetrahedrite nanoparticles. Transmission electron microscopy (TEM) data of the as-synthesized Cu-based and Zn-doped powders are displayed in Figure 4.3. Both samples appear to be polydisperse nanoparticles on the length scale of 50–200 nm. Although these sizes are too large for quantum confinement effects to play a significant role, pellets consolidated from powders within this size regime have previously demonstrated enhanced thermopowers and reduced thermal conductivity.[26,39,165] Scanning electron microscopy (SEM) images of the as-synthesized $Cu_{12}Sb_4S_{13}$ product are shown in Figure 4.4. The microscopy data reveal particles with the tetrahedron morphology characteristic of tetrahedrite compounds. The author would like to acknowledge and thank Cameron Holder and Dr. Jennifer Misuraca for acquisition of these TEM and SEM images, respectively. Accordingly, the TE properties of samples synthesized by the modified polyol process are expected to be positively impacted by their nanostructuring.

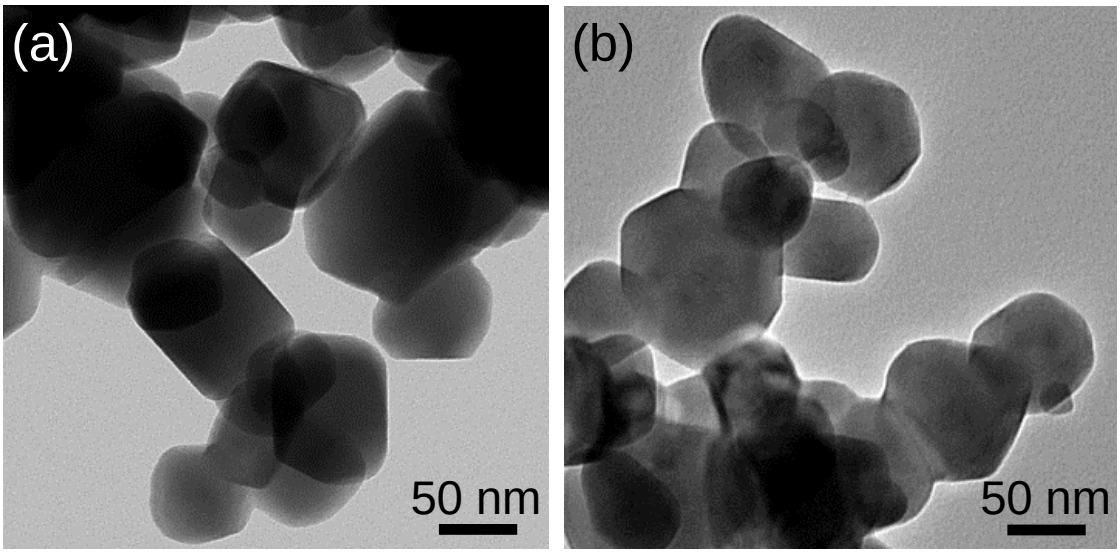

Figure 4.3: Transmission electron microscopy images of pre-processed (a) $Cu_{12}Sb_4S_{13}$ and (b) $Cu_{11}ZnSb_4S_{13}$ powder products synthesized by modified polyol process.

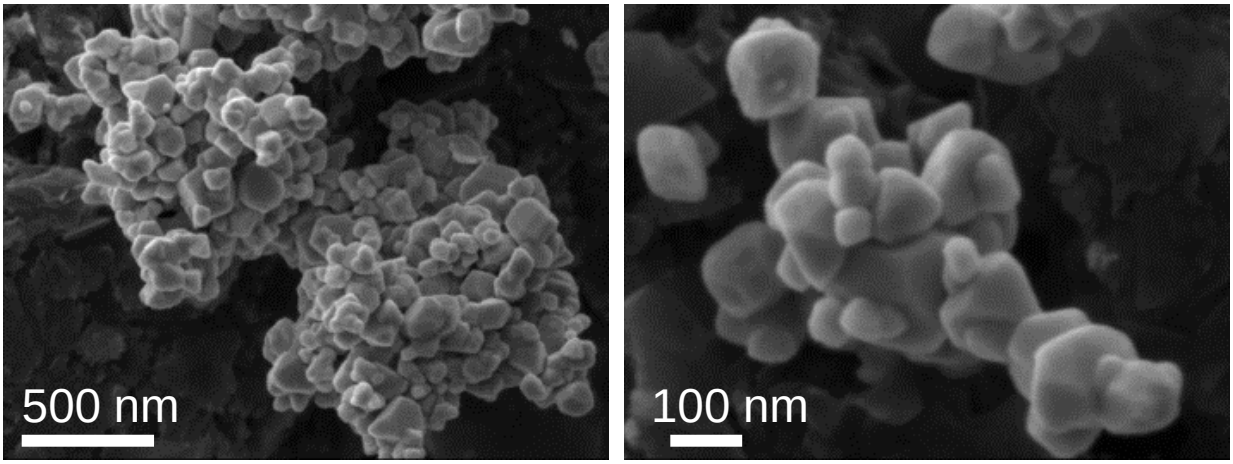

Figure 4.4: Scanning electron microscopy images of pre-processed $Cu_{12}Sb_4S_{13}$ powder product synthesized by modified polyol process.

4.2.2 Analysis of Processed Samples

Tetrahedrite powders obtained from the modified polyol process were consolidated via spark plasma sintering (SPS) profile A (see Figure 3.5). Figure 4.5 shows the XRD profiles obtained after processing. In accordance with the claim that dopants stabilize the tetrahedrite structure, the Zn-doped sample remains completely single-phase. On the other hand, the Cu-based sample phase-separated into two tetrahedrite structures with slightly different unit cell parameters. This is believed to be the exsolution of Cu-rich ($Cu_{12+x}Sb_4S_{13}$) and Cu-poor ($Cu_{12}Sb_4S_{13}$) phases that has been demonstrated previously for tetrahedrites with excess Cu.[98, 99, 120, 166] Regardless, the tetrahedrite crystal structure is present in both samples with no impurity phases detected.

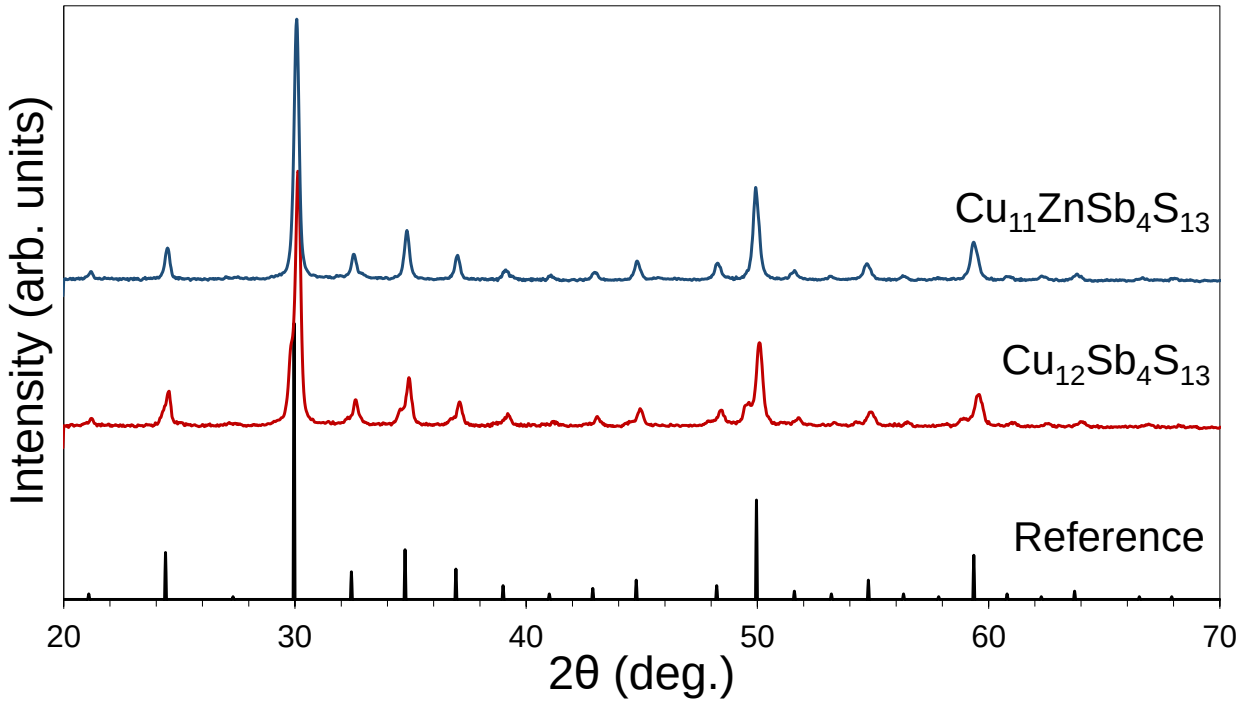

Figure 4.5: X-ray diffraction profiles of $Cu_{12}Sb_4S_{13}$ and $Cu_{11}ZnSb_4S_{13}$ synthesized by modified polyol process (post-processing).

High-resolution SEM images were obtained to examine the structure of samples after undergoing SPS. Pellets of $Cu_{12}Sb_4S_{13}$ and $Cu_{11}ZnSb_4S_{13}$ were fractured, and SEM images collected along the break are displayed in Figure 4.6. Low magnification images show a close-packed arrangement of particles on the 10^1 to 10^2 nm size scale. At higher magnifications, necking is noticeable between particles. One major advantage of SPS as a consolidation technique is that its rapid and low-energy nature prevents grain agglomeration and coarsening. As is shown in the high-resolution SEM images, nanostructuring was maintained in both samples after undergoing SPS processing. Additional SEM images of the surfaces of post-processed samples collected via secondary electrons and backscatter electrons are provided in Figure A2 of the Appendix.

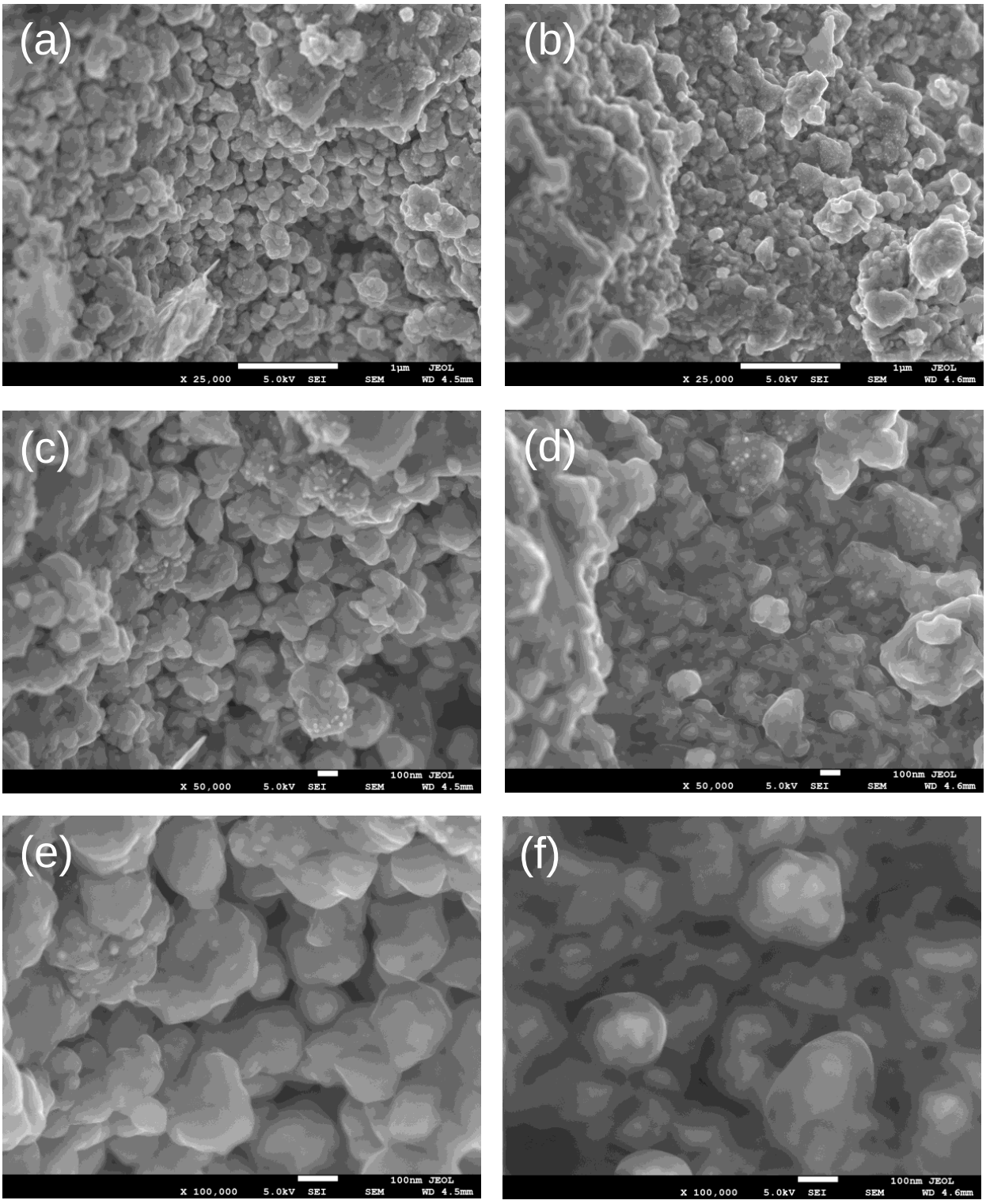

Figure 4.6: High-resolution scanning electron microscopy images of (a,c,e) $Cu_{12}Sb_4S_{13}$ and (b,d,f) $Cu_{11}ZnSb_4S_{13}$ synthesized by modified polyol process (post-processing).

Elemental distribution maps were collected via energy-dispersive X-ray spectroscopy (EDS). SEM images of the site where EDS data were collected, and their associated elemental distribution maps, are shown in Figure 4.7. EDS maps indicate stoichiometric homogeneity throughout both samples, and the incorporation of Zn is confirmed in the Zn-doped sample. Therefore, the elemental distribution appears to be relatively homogeneous in both $Cu_{12}Sb_4S_{13}$ and $Cu_{11}ZnSb_4S_{13}$ tetrahedrites synthesized by the modified polyol process.

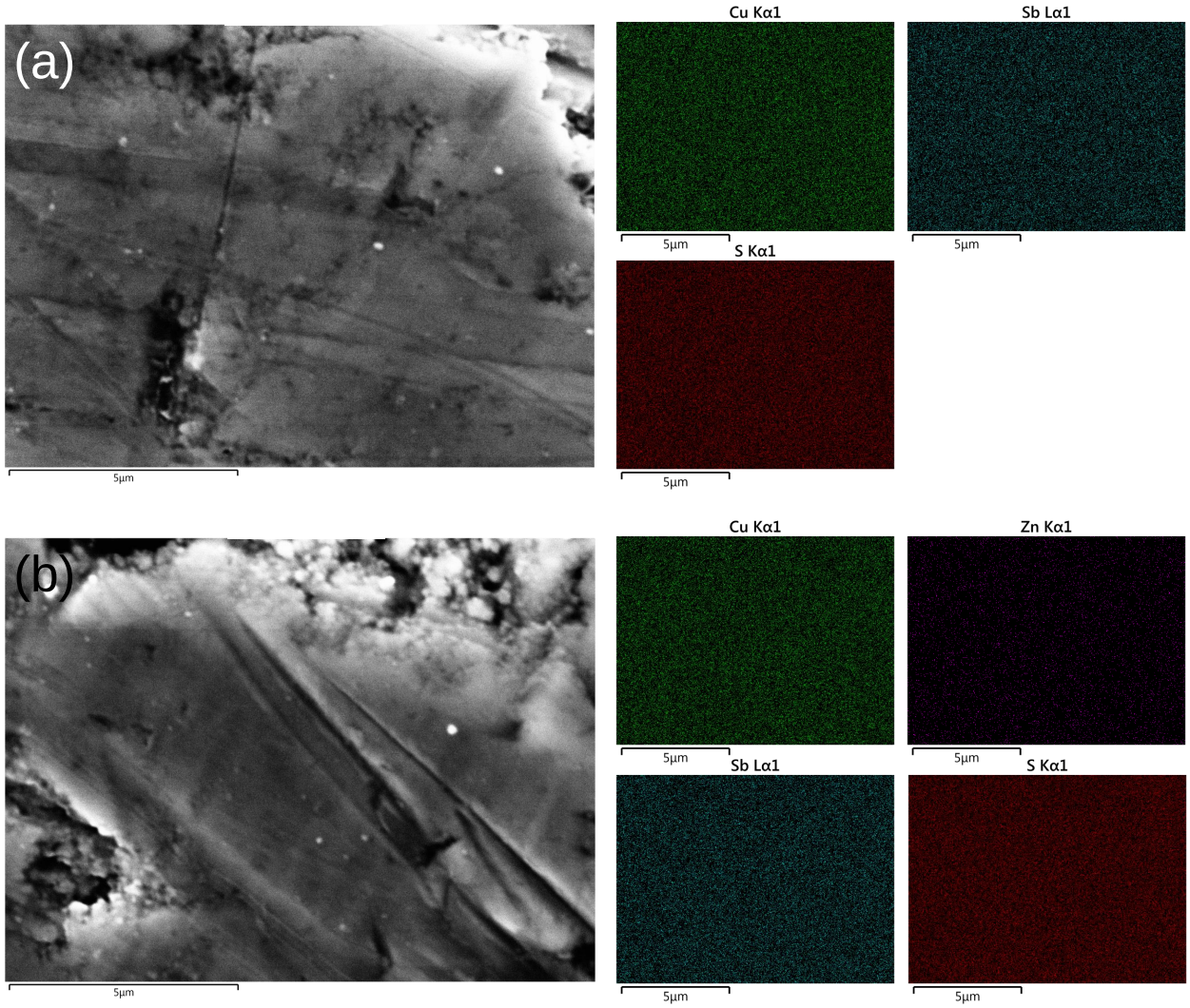

Figure 4.7: Energy-dispersive X-ray spectroscopy data of (a) $Cu_{12}Sb_4S_{13}$ and (b) $Cu_{11}ZnSb_4S_{13}$ synthesized by modified polyol process. Electron microscopy images (left-side) display the sites where elemental distribution maps (right-side) were collected.

To further analyze the relationship between structure and elemental distribution, compositions were determined by EDS measurements. The data for pre-processed and post-processed tetrahedrites are summarized in Table 4.1. EDS data were collected in collaboration with Hope College. Both data sets indicate Cu-enrichment, yet the Zn-doped composition maintains an 11:1 atomic ratio of Cu to Zn. The atomic distribution is relatively close to the target stoichiometry for all other elements, besides Cu. Regardless, all compositions fall within the range of stable compositions reported previously for tetrahedrites.[96] The Cu-enrichment demonstrated by the post-processed Cu-based sample is consistent with its XRD profile. Moreover, the post-processed compositions match the pre-processed powders within error, providing evidence that no significant chemical changes take place during processing. Overall, the samples demonstrate enrichment on the metal site, while still within the range of stable tetrahedrite compositions before and after SPS processing.

Target Composition	EDS Data (pre-processing)	EDS Data (post-processing)
$Cu_{12}Sb_4S_{13}$	$Cu_{13.6\pm0.1}Sb_{4.3\pm0.2}S_{13.0\pm0.3}$	$Cu_{13.8\pm0.2}Sb_{4.0\pm0.1}S_{13.0\pm0.2}$
$Cu_{11}ZnSb_4S_{13}$	$Cu_{12.6\pm0.2}Zn_{1.2\pm0.1}Sb_{4.2\pm0.1}S_{13.0\pm0.2}$	$Cu_{12.3\pm0.2}Zn_{1.1\pm0.1}Sb_{4.0\pm0.1}S_{13.0\pm0.2}$

Table 4.1: Energy-dispersive X-ray spectroscopy (EDS) data of Cu-based and Zn-doped tetrahedrites synthesized by modified polyol process; data are included for pre-processed powders and post-processed samples.

4.2.3 Transport Property Characterization

Electrical transport data are displayed in Figure 4.8 over the range of 80–723 K. Thermopower (Figure 4.8a) of both samples demonstrate p-type metallic behavior with a positive linear temperature dependence. The Cu-based tetrahedrite shows a lower thermopower than the zinc-doped sample, which is likely a consequence of Zn acting as a dopant and

shifting the Fermi level closer to the valence band edge. As Cu^{1+} is replaced by Zn^{2+}, electrons are added to the lattice and holes are filled. The outlier thermopower datum at 80 K in $Cu_{12}Sb_4S_{13}$ may be indicative of the metal to semiconductor transition that has been reported to occur near 85 K.[60–62] At 723 K, $Cu_{12}Sb_4S_{13}$ and $Cu_{11}ZnSb_4S_{13}$ achieve thermopower values of approximately $220\,\mu VK^{-1}$ and $245\,\mu VK^{-1}$. These values are higher than those reported for bulk samples of the same compositions synthesized by traditional means.[66, 89] The greater thermopowers could be attributed to nanostructuring affecting the electronic band structure.[40, 167] Alternatively, these nanostructured samples may be demonstrating an energy filtering process, in which charge carriers are selectively scattered according to their energies.[165, 168] Evidently, nanostructuring impacts thermopower behavior in tetrahedrites produced by the modified polyol process.

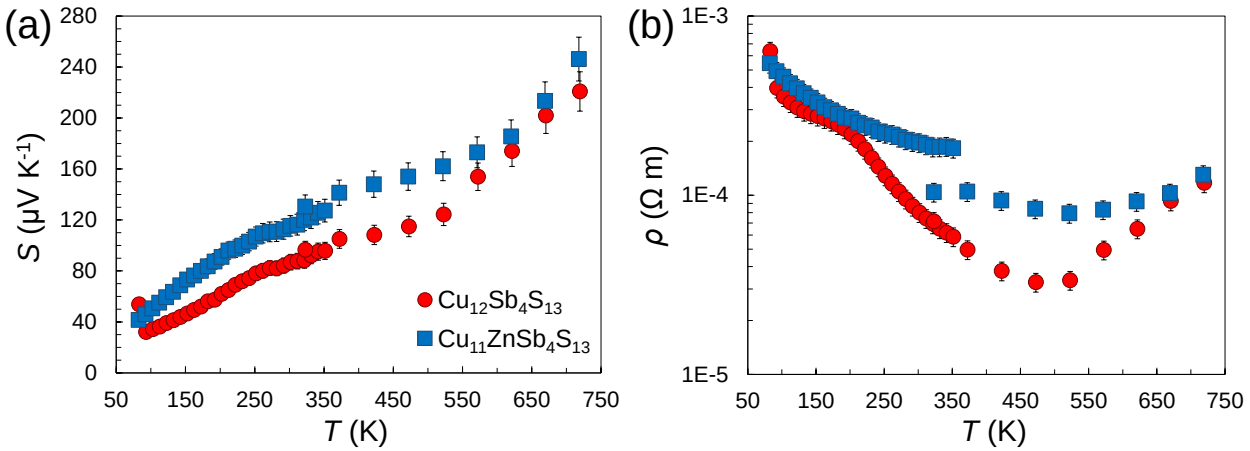

Figure 4.8: Electrical transport data of $Cu_{12}Sb_4S_{13}$ and $Cu_{11}ZnSb_4S_{13}$ synthesized by modified polyol process, where data for thermopower (S) and electrical resistivity (ρ) are shown in (a) and (b), respectively.

In accordance with thermopower data, the Cu-based tetrahedrite demonstrates lower electrical resistivity (Figure 4.8b) values than the Zn-doped sample. Again, this pattern is consistent with our understanding of the electronic band structure of $Cu_{12}Sb_4S_{13}$ and

$Cu_{11}ZnSb_4S_{13}$. The samples reach resistivities as low as 3×10^{-5} Ωm and 8×10^{-5} Ωm at 523 K in Cu-based and Zn-doped samples, respectively. This is partially owing to greater porosity (92% density by polyol versus 95% in the literature), but the density difference is not enough to account for differences between our samples and those previously reported. Reduced charge carrier conduction is a consequence of increased grain boundary scattering and changes in the temperature dependence of carrier mobility.

Nanostructuring effects are expected to be the most prevalent in the thermal conductivity data. Figure 4.9a depicts thermal conductivity data for Cu-based and Zn-doped tetrahedrites. It is immediately apparent that the radiation correction in the low-temperature regime is not strong enough, which is most prominent for samples with low thermal conductivity and high electrical conductivity. Regardless, the high-temperature data demonstrate a shape consistent with a mixture of interfacial scattering (low and intermediate temperatures) and phonon-phonon scattering (higher temperatures). The total thermal conductivities are significantly lower than previously reported values for these compositions, which range from 0.7 to 1.5 $Wm^{-1}K^{-1}$.[66,141] Evidently, grain boundary scattering strongly reduces phonon propagation via interfacial scattering. In addition, differences between Cu-based and Zn-doped thermal conductivity values are attributed to mass-difference impurity scattering from the increased presence of Zn point defects. In general, the thermal conductivity data agree with previously reported behavior for Zn doping in tetrahedrites.

After removing the electronic component from the total thermal conductivity, we obtain data for lattice thermal conductivity data (Figure 4.9b). The samples align reasonably well with each other, reaching values below 0.4 $Wm^{-1}K^{-1}$ at 723 K. Overall, the thermal conductivity values obtained for these samples are much lower than those reported for bulk tetrahedrites.[66] This provides further evidence for greater grain boundary scattering with

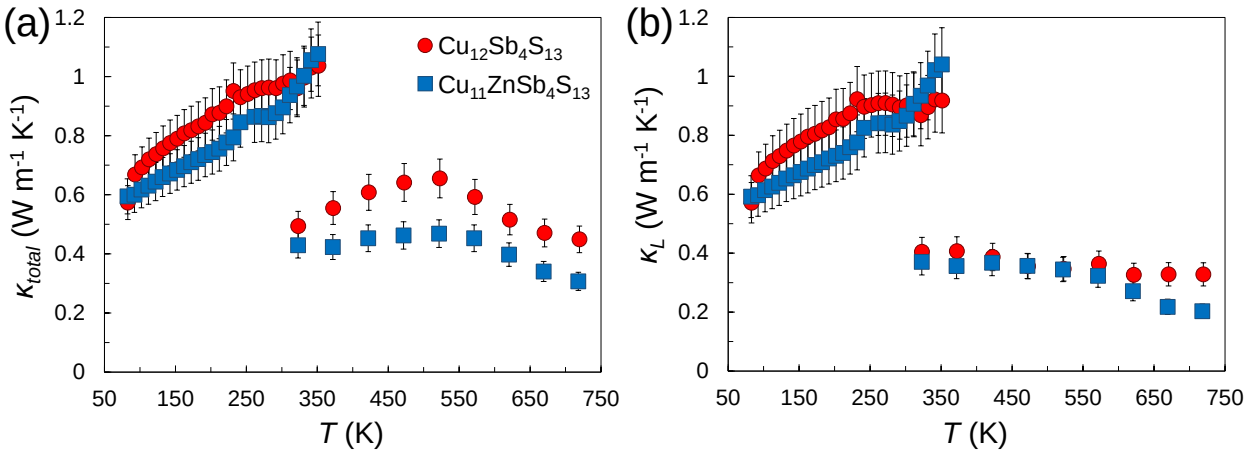

Figure 4.9: Thermal transport data of $Cu_{12}Sb_4S_{13}$ and $Cu_{11}ZnSb_4S_{13}$ synthesized by modified polyol process, where data for total thermal conductivity (κ_{total}) and lattice thermal conductivity (κ_L) are shown in (a) and (b), respectively.

a phonon mean free path that approaches the theoretical minimum. Variation between the lattice thermal conductivities can be explained by point defect scattering in the Zn-doped sample. Of course, the slightly lower than ideal sample densities also contributes to the low lattice thermal conductivity demonstrated by these samples. Thus, exceptionally low values of lattice thermal conductivity were obtained due to phonon scattering from point defects, the complex crystal structure, and interfacial scattering at grain boundaries.

Lastly, tetrahedrites synthesized by the modified polyol process exhibit ZT values that are on par or improved compared to bulk materials. ZT values (Figure 4.10) peak at 723 K with values of 0.66 and 1.09 obtained for the Cu-based and Zn-doped polyol samples, respectively. While enhanced thermopower and reduced thermal conductivity values were obtained, these samples demonstrate relatively similar ZT behavior owing to greater electrical resistivity. Our $Cu_{12-x}Zn_xSb_4S_{13}$ ($x = 1$) sample demonstrates higher ZT values than the previously reported by Lu et al., which attained $ZT = 0.7$ at 673 K and $ZT = 0.95$ at 723 K for $x = 1$ and $x = 0.5$, respectively. Overall, nanostructuring in our Cu-based and Zn-doped tetrahedrites synthesized by the modified polyol process led to comparable or better ZT

values than previous reports. This work lays the foundation for future TE research with tetrahedrites synthesized by the modified polyol process, which is significantly simplified and lower energy than traditional methods.

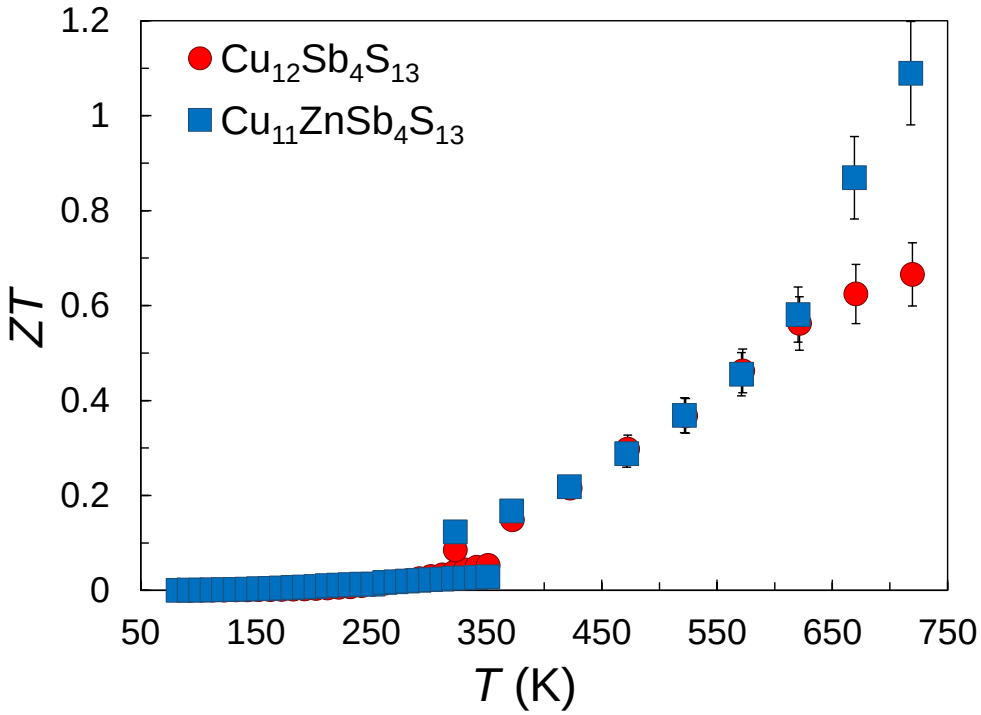

Figure 4.10: Figure of merit (ZT) data of $Cu_{12}Sb_4S_{13}$ and $Cu_{11}ZnSb_4S_{13}$ synthesized by modified polyol process.

4.3 $Cu_{12-x}Fe_xSb_4S_{13}$

Iron is a unique dopant in tetrahedrite because its valence state varies as a function of composition. Over twenty years ago, this distinct behavior was studied by mineralogists, and it was concluded that Fe in synthetic $Cu_{12-x}Fe_xSb_4S_{13}$ was nominally trivalent from $0 \leq x \leq 1$ and divalent for $x > 1$.[169–171] However, recent studies have suggested that both Fe^{2+} and Fe^{3+} valence states persist at concentrations of ($x = 1.5$ and 2.0), while only Fe^{3+} is present at lower concentrations ($x = 0.8$, 1.0, and 1.2).[103] Electron hopping between

the different Fe centers was observed for certain compositions as well, but hopping in mixed valence tetrahedrites will be addressed in Chapter 5. The structural behavior of Fe-doped tetrahedrites has been analyzed by neutron diffraction measurements, which indicate that Fe substitutes exclusively on the tetrahedral Cu12d site.[103, 105, 172] At the same time, electronic band structure calculations have indicated a collection of minority spin states that become available above the Fermi level upon doping with Fe.[66, 67] In a similar manner to how divalent Zn dopants raise the Fermi level into the band gap, we hypothesize that doping with trivalent Fe may have a significant enough effect to induce n-type behavior. Thus, Fe-doped tetrahedrites demonstrate remarkable mixed valence states unlike other doped tetrahedrites, and it is difficult to ascertain the outcome of such phenomena on TE properties.

There are limited reports on the TE properties of Fe-doped tetrahedrites over a range of compositions. Suekuni et al. reported TE properties of from 4 to 340 K for $Cu_{10}Fe_2Sb_4S_{13}$, and soon after, Heo et al. reported high-temperature TE properties from 300 to 600 K.[55,89] Recently, Tippireddy et al. measured TE properties of $Cu_{11.5}Fe_{0.5}Sb_4S_{13}$ from 350 to 700 K, obtaining a max ZT value of 0.5.[70] These investigations observed p-type behavior consistent with the study by Lu et al. that examined natural Fe- and As-bearing mineral specimens combined with synthetic Cu-based tetrahedrite.[66] Many of the aforementioned studies involved impure and low density samples, and the TE properties have only been reported for a select few Fe-doped tetrahedrites ($x = 1.0$ and 2.0 mostly). Therefore, to further explore the TE properties of Fe-doped compositions heretofore not studied, $Cu_{12-x}Fe_xSb_4S_{13}$ ($x = 0.5$, 1.0, and 1.5) tetrahedrites were synthesized by the modified polyol process. Much of these findings are included in the *Materials Today Physics* article by Weller et al.[173]

4.3.1 Structural and Compositional Characterization

Iron-doped tetrahedrites produced by the modified polyol process were consolidated via SPS profile B. Figure 4.11 shows the X-ray diffraction profiles of $Cu_{12-x}Fe_xSb_4S_{13}$ ($x = 0.5$, 1.0, and 1.5) obtained after processing. Each sample exhibits mostly pure tetrahedrite, aside from the peak at $2\theta \approx 46°$ in the $x = 1.0$ data, which corresponds to the Cu_2S phase. In any case, the minuscule presence of secondary phase is not expected to impact transport properties significantly. The $x = 0.5$ profile is broadened because the measurement was taken from ball milled powder instead of the usual mortar and pestle treatment. These Fe-doped tetrahedrites maintain the tetrahedrite crystal structure before and after processing.

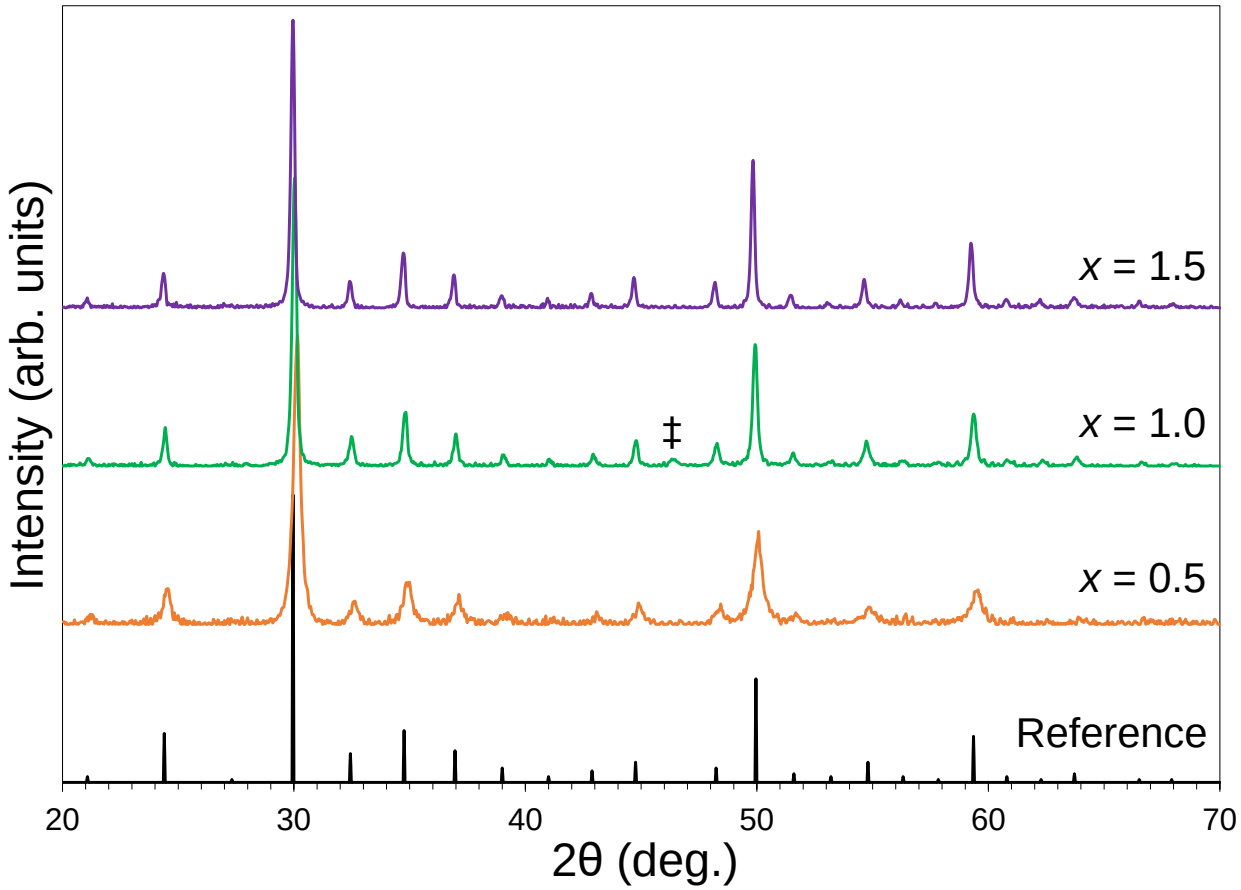

Figure 4.11: X-ray diffraction profiles of $Cu_{12-x}Fe_xSb_4S_{13}$ ($x = 0.5$, 1.0, and 1.5) synthesized by modified polyol process. An impurity peak of Cu_2S is marked by a ‡ symbol.

Incorporation of Fe into the tetrahedrite structure was confirmed by EDS measurements. Elemental distribution maps, and the associated scanning electron microscopy image of the site, are shared for $Cu_{10.5}Fe_{1.5}Sb_4S_{13}$ in Figure 4.12. White particles are residual SiC from the polishing medium. EDS maps confirm the presence of Fe in the tetrahedrite structure, as well as relatively homogenous distribution of Cu, Sb, and S. This EDS data is representative for the set of Fe-doped samples in this section. Quantitative EDS data for all Fe-doped tetrahedrites synthesized by the modified polyol process are shown in Table 4.2. EDS data were collected in collaboration with Hope College. In general, data was collected over multiple sites and a spot-to-spot deviation less than 6% was observed for all elements in all samples. Similar to the Cu-based and Zn-doped samples, Cu-enriched compositions are detected. Nevertheless, the Fe content remains near the target amount in our samples, and the measured compositions agree with the nominal compositions detected before processing, indicating that no material was lost during the pellet preparation.

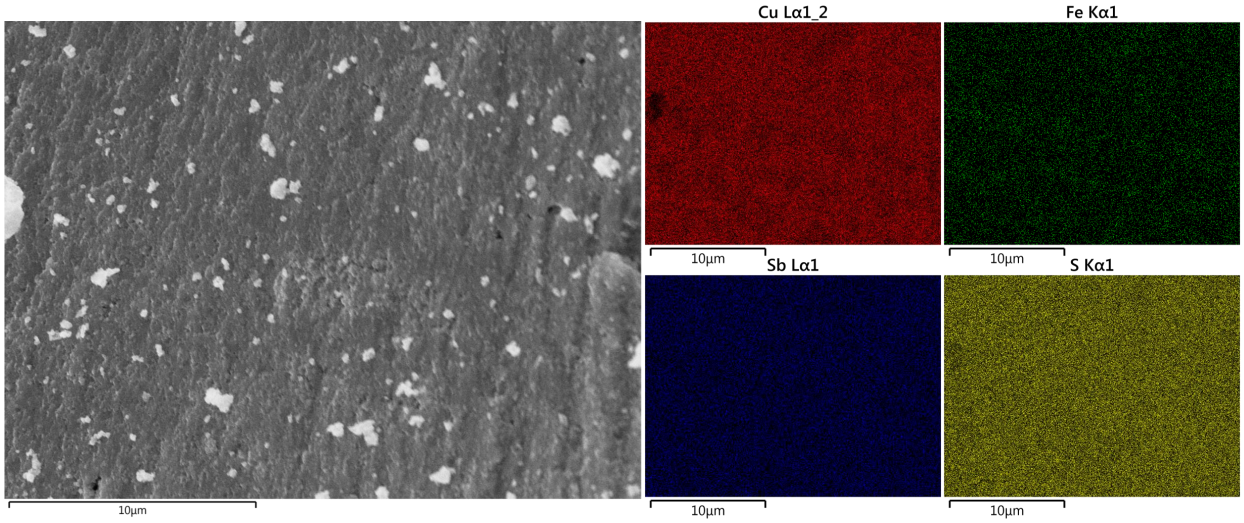

Figure 4.12: Energy-dispersive X-ray spectroscopy data of $Cu_{10.5}Fe_{1.5}Sb_4S_{13}$ synthesized by modified polyol process. Electron microscopy image (left-side) displays the site where elemental distribution maps (right-side) were collected.

Target Composition	EDS Data
$Cu_{11.5}Fe_{0.5}Sb_4S_{13}$	$Cu_{12.5\pm0.2}Fe_{0.5\pm0.1}Sb_{4.4\pm0.2}S_{13.0\pm0.2}$
$Cu_{11}FeSb_4S_{13}$	$Cu_{12.4\pm0.5}Fe_{1.2\pm0.1}Sb_{4.0\pm0.1}S_{13.0\pm0.4}$
$Cu_{10.5}Fe_{1.5}Sb_4S_{13}$	$Cu_{11.2\pm0.3}Fe_{1.7\pm0.1}Sb_{4.2\pm0.1}S_{13.0\pm0.2}$

Table 4.2: Energy-dispersive X-ray spectroscopy (EDS) data of $Cu_{12-x}Fe_xSb_4S_{13}$ ($x = 0.5$, 1.0, and 1.5) synthesized by modified polyol process.

4.3.2 Transport Property Characterization

Thermopower data are displayed in Figure 4.13a. At 673 K, the $x = 0.5$ thermopower peaks at about $280\,\mu VK^{-1}$, while the other two samples converge to approximately $210\,\mu VK^{-1}$. These values are higher than those reported by Tippireddy et al. ($170\,\mu VK^{-1}$ at 673 K for $x = 0.5$) and Heo et al. ($170\,\mu VK^{-1}$ at 575 K for $x = 2$).[70, 89] Electrical resistivity values (Figure 4.13b) decrease with increasing temperature, which is typical for semiconducting materials. The $x = 1$ and 1.5 samples are highly resistive at low temperatures as expected from hole filling via Fe doping. Contrastingly, the $x = 0.5$ sample demonstrates the lowest resistivity over most of the measurement range owing to the location of the Fermi level in the valence band. These findings agree well with resistivity data for Fe-substituted tetrahedrites from 80 to 720 K, which have been reported to range from 10^1 to 10^{-4} Ωm.[70,89] Thus, our resitivity values are similar to those previously reported for Fe-doped tetrahedrites, given differences sample density ($\geq$93% for all samples) and chemical composition.

Unique signatures of bipolar conduction are apparent in the $Cu_{12-x}Fe_xSb_4S_{13}$ thermopower data. Most notably, the $x = 1$ and 1.5 samples demonstrate a transition from n-type to p-type as temperature increases. The $x = 1$ sample transitions at 160 K and demonstrates the largest magnitude negative thermopower of $-19\,\mu VK^{-1}$ at 80 K. Interestingly, the $x = 1.5$ sample shows n-type behavior over a larger temperature range from 80 to 310 K with the greatest negative magnitude $-12\,\mu V$ at 240 K. While this behavior is quite

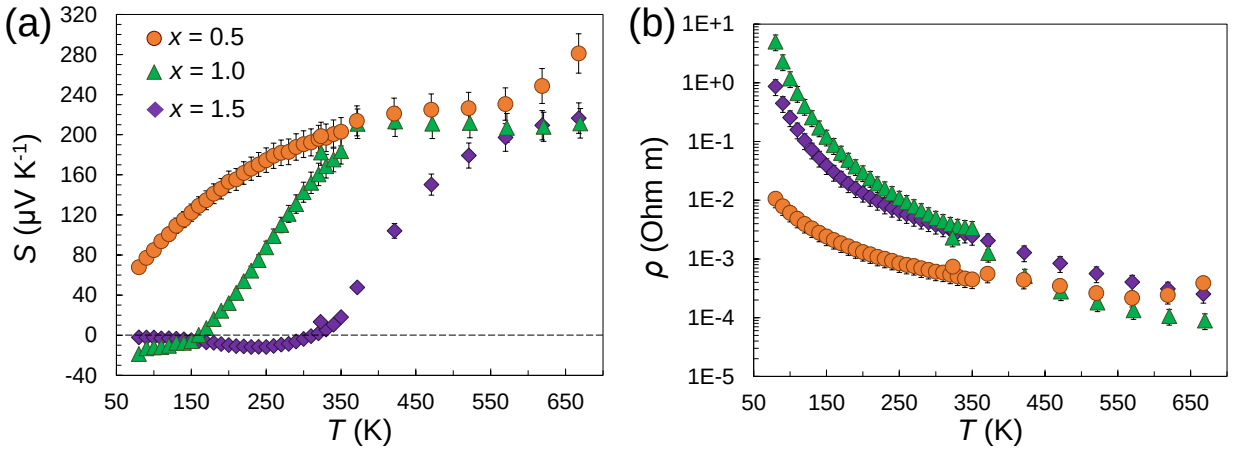

Figure 4.13: Electrical transport data of $Cu_{12-x}Fe_xSb_4S_{13}$ (x = 0.5, 1.0, and 1.5) synthesized by modified polyol process, where data for thermopower (S) and electrical resistivity (ρ) are shown in (a) and (b), respectively.

novel in tetrahedrite materials, copper ferrites and other ternary copper sulfides have shown comparable temperature dependent transitions from n-type to p-type conduction.[174, 175] Although the $x = 0.5$ composition is p-type over the entire temperature range, all three compositions exhibit a similar temperature-dependent curvature from negative to positive thermopower. The crossover temperature may be systematically related to Fe concentration in $Cu_{12-x}Fe_xSb_4S_{13}$, but additional liquid He cryostat measurements are needed to elucidate this concept. In the low-temperature regime, electrons dominate holes in terms of charge conduction in these Fe-doped tetrahedrites.

N-type behavior is attributed to doping effects, minority spin states in the band structure, and charge carrier hopping. The replacement of Cu ions with $Fe^{2+/3+}$ dopant ions elevates the Fermi level into the pocket of minority states engendered by Fe minority spin centers.[66, 67] We propose that carriers excited into the minority band states are dominant at lower temperatures, yielding n-type behavior. It should be noted that valence bands also have greater curvature (lower effective mass and higher mobility), whereas minority spin bands are relatively flat (high effective mass and low mobility). Accordingly, carriers are excited

over a larger energy range as temperature increases, and holes become the dominant carriers as valence band states outnumber minority spin states. Furthermore, doping is expected to be more effective in Cu-rich compositions (like those reported here), owing to the greater portion of Cu^{1+} ions.[65] Models for explaining hopping in tetrahedrites will be explored in Chapter 5, and a different set of samples will be analyzed alongside this set. Therefore, at higher temperatures Fe-doped tetrahedrite behaves more like a typical semiconductor that demonstrates standard band conduction.

Figure 4.14 presents thermal transport data for Fe-doped samples. The low-temperature radiation correction is a decent approximation, although it still is not strong enough to match data between overlapping measurement regions. For the $x = 0.5$ composition at 673 K, our thermal conductivity values are significantly lower ($\leq$0.6 $Wm^{-1}K^{-1}$) relative to bulk samples (1.1 $Wm^{-1}K^{-1}$).[70] After removing the electronic thermal conductivity, lattice thermal conductivity values approach the theoretical minimum of 0.4 $Wm^{-1}K^{-1}$.[34] The drop-off in lattice thermal conductivity beyond 573 K is likely an indication of sample degradation at higher temperatures.

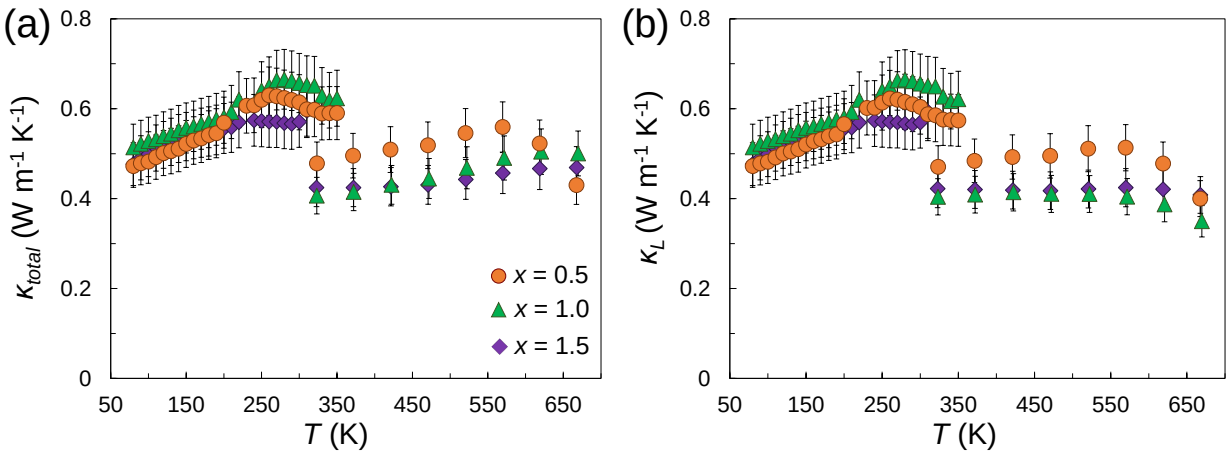

Figure 4.14: Thermal transport data of $Cu_{12-x}Fe_xSb_4S_{13}$ ($x = 0.5$, 1.0, and 1.5) synthesized by modified polyol process, where data for total thermal conductivity (κ_{total}) and lattice thermal conductivity (κ_L) are shown in (a) and (b), respectively.

Figure of merit data for Fe-doped tetrahedrites synthesized by the modified polyol process are displayed in Figure 4.15. Peak ZT values of 0.32, 0.67, and 0.26 were achieved at 673 K for the $x = 0.5, 1,$ and 1.5, respectively. Compared to data reported previously by other groups, these compounds outperform samples with lower ($x = 0.5$) and higher ($x = 2$) amounts of Fe.[70, 89] For the $x = 1$ composition, ZT values agree quite well with the recent reports by Guler et al. for this composition.[106] These findings lay the groundwork for designing n-type tetrahedrites. In terms of next steps, magnetization measurements would provide insight on the valence state of Fe at various concentrations, and combining data with TE measurements could deepen our understanding of this complex material system.

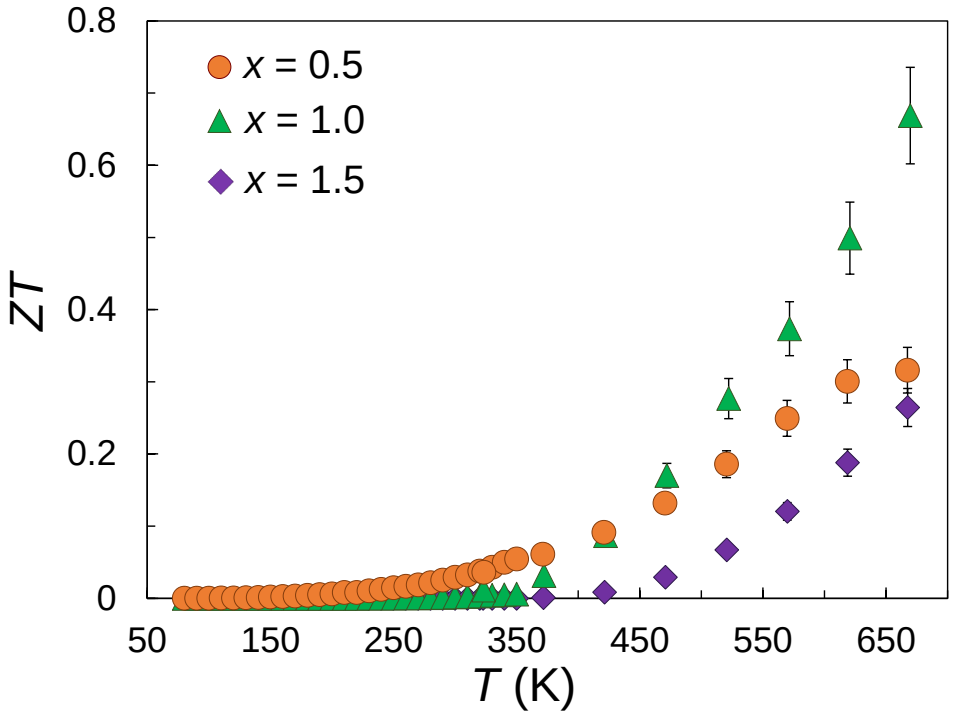

Figure 4.15: Figure of merit (ZT) data of $Cu_{12-x}Fe_xSb_4S_{13}$ ($x = 0.5$, 1.0, and 1.5) synthesized by modified polyol process.

Chapter 5

Mechanical Alloying Synthesis

Mechanical alloying is a simple and scalable approach for obtaining tetrahedrite thermoelectrics with relative ease. This chapter will detail the exploration of mechanical alloying as a method for synthesizing tetrahedrites doped with Ni, Zn, and Fe. This technique has been shown to synthesize a broad phase space of tetrahedrites in about 48 h of total reaction time. Furthermore, mechanical alloying avoids issues with large sulfur overpressure in the conventional melt-recrystallization method. Therefore, mechanical alloying boasts multiple advantages over the traditional solid-state synthesis including shorter reaction times, greater reproducibility, and a more versatile range of possible compositions.

To begin, a brief review of mechanical alloying will be provided. Subsequently, the findings from exploratory studies with Ni and Zn co-doped tetrahedrites will be shared, followed by results of Fe-doped tetrahedrites synthesized by mechanical alloying. Samples of $Cu_{12-x}Fe_xSb_4S_{13}$ will be compared to similar compositions synthesized by the modified polyol method (Chapter 4). Lastly, the electron exchange phenomenon observed in Fe-doped tetrahedrites will be analyzed.

5.1 Background on Mechanical Alloying

Mechanical alloying is a straightforward technique, where powder precursors undergo a mechanochemical reaction via milling. The grinding media, milling time, and atmospheric

reactivity are common factors to consider when performing these reactions. Since the 1990s, mechanical alloying research has gained momentum in an effort to find viable industrial alternatives to rapid solidification processing reactions.[176] A diverse array of materials are viable candidates for mechanical alloying synthesis, including intermetallic compounds and ceramic oxides.[177, 178] Commonly, powderized products from the milling process are densified by hot-pressing or spark plasma sintering (SPS).

Previously, other groups have synthesized tetrahedrites by mechanical alloying. Barbier and coworkers were the first group to do this by synthesizing $Cu_{10.4}Ni_{1.6}Sb_4S_{13}$ and obtaining ZT of 0.75 at 700 K.[109] In a follow-up study by the same group, the scalability of this procedure was utilized for fabricating large square monoliths ($50 \times 50 \times 3$ mm) of tetrahedrite from mechanically alloyed powders.[110] Similarly, Harish et al. studied phase stability in Zn-doped tetrahedrites made by mechanical alloying.[113] Very recently, $Cu_{12}Sb_4S_{13}$ was prepared by planetary milling at 350 rpm for 24 h.[94] To the author's knowledge, this study provided the highest ZT to date for the unsubstituted composition, reaching a peak ZT of 0.87 at 723 K. In another study, $Cu_{12}Sb_4S_{13}$ was synthesized by mechanical alloying for photovoltaic thin film applications.[179] Therefore, mechanical alloying has been shown to be a practical approach for producing tetrahedrite TE materials.

5.2 $Cu_{10}Ni_{2-x}Zn_xSb_4S_{13}$

Some of the highest ZT values reported for tetrahedrite arise in Ni and Zn co-doped compositions. For example, Lu et al. achieved ZT above unity at 723 K for $Cu_{10.5}NiZn_{0.5}Sb_4S_{13}$.[90] The additional Ni-dopant electronic states near the Fermi level, combined with fine adjustment of the Fermi level via Zn doping, were shown to significantly improve TE performance.

Using these findings as a foundation, we attempted to use mechanical alloying to synthesize a broader phase space of unexplored co-doped compositions involving fully substituted tetrahedrites (with 10 Cu atoms per formula unit). In the following subsections, the characterization of $Cu_{10}Ni_{2-x}Zn_xSb_4S_{13}$ ($x = 0$, 0.5, 1.0, 1.5, and 2.0) synthesized by mechanical alloying will be presented, and much of this data is included in the *Journal of Alloys and Compounds* article by Weller and Morelli.[148]

5.2.1 Structural and Compositional Characterization

The fully substituted Zn-doped composition was chosen as an initial exploratory composition owing to its enhancement in the formation of pure-phase tetrahedrite. Figure 5.1 displays X-ray diffraction profiles for this composition every 8 h throughout the planetary ball milling process. After 8 h of milling, famatinite (Cu_3SbS_4) is the primary phase and there is virtually no tetrahedrite phase. Following every subsequent 8 h interval, famatinite diminishes and tetrahedrite forms, until only pure-phase tetrahedrite is present after 48 h. This reaction time was shown to yield single-phase tetrahedrite for the entire solid-solution studied here (see Figure A3 of the Appendix). These reaction times are longer than those reported by Barbier et al. (8 h at 600 rpm).[109] We attribute this to equipment limitations because our ball mill cannot exceed 300 rpm, and in turn, longer milling times are required. Regardless, the phase evolution exhibited by our samples qualitatively matches that of previous reports.

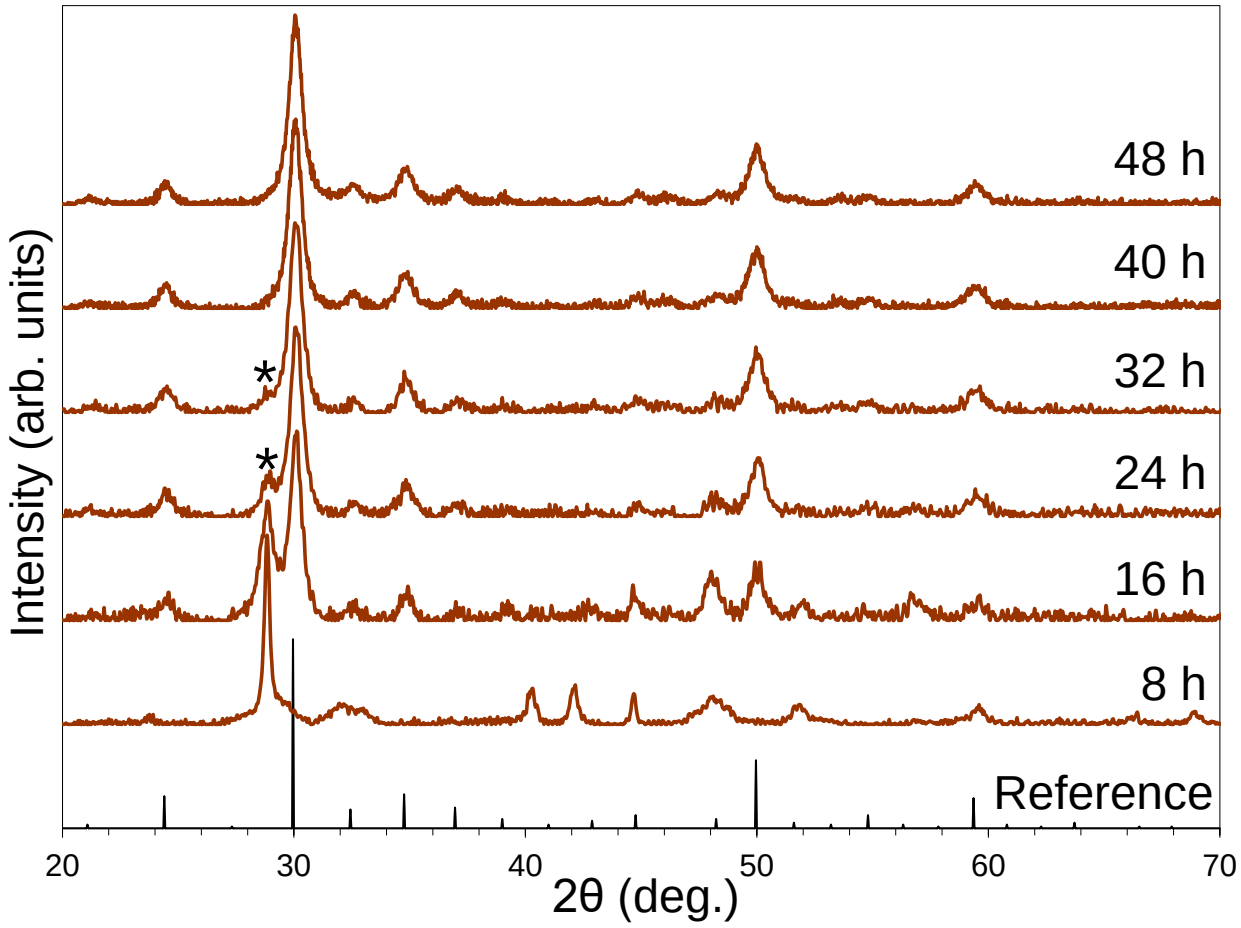

Figure 5.1: X-ray diffraction profiles of $Cu_{10}Zn_2Sb_4S_{13}$ after 8, 16, 24, 32, 40, and 48 h of planetary ball milling. Primary peaks of Cu_3SbS_4 impurities are marked by $*$ symbols.

Figure 5.2 shows the X-ray diffraction profiles obtained from the solid solution of Ni and Zn co-doped tetrahedrites after processing by spark plasma sintering (SPS). Peaks become noticeably more narrow and all samples demonstrate mostly pure tetrahedrite, aside from the small presence of NiS secondary phases in samples with lower levels of Zn doping ($x = 0$, 0.5, and 1.0). The solid solution demonstrates a systematic shift to lower 2θ with increasing Zn concentration, and lattice parameters are presented in Figure 5.3. These data agree very well with other groups, whom report values of 10.31 Å and 10.38 Å for the $x = 0$ and $x = 2$ compositions, respectively.[55] The XRD data provide evidence that mostly pure tetrahedrite is obtained via mechanical alloying after 48 h of planetary ball milling.

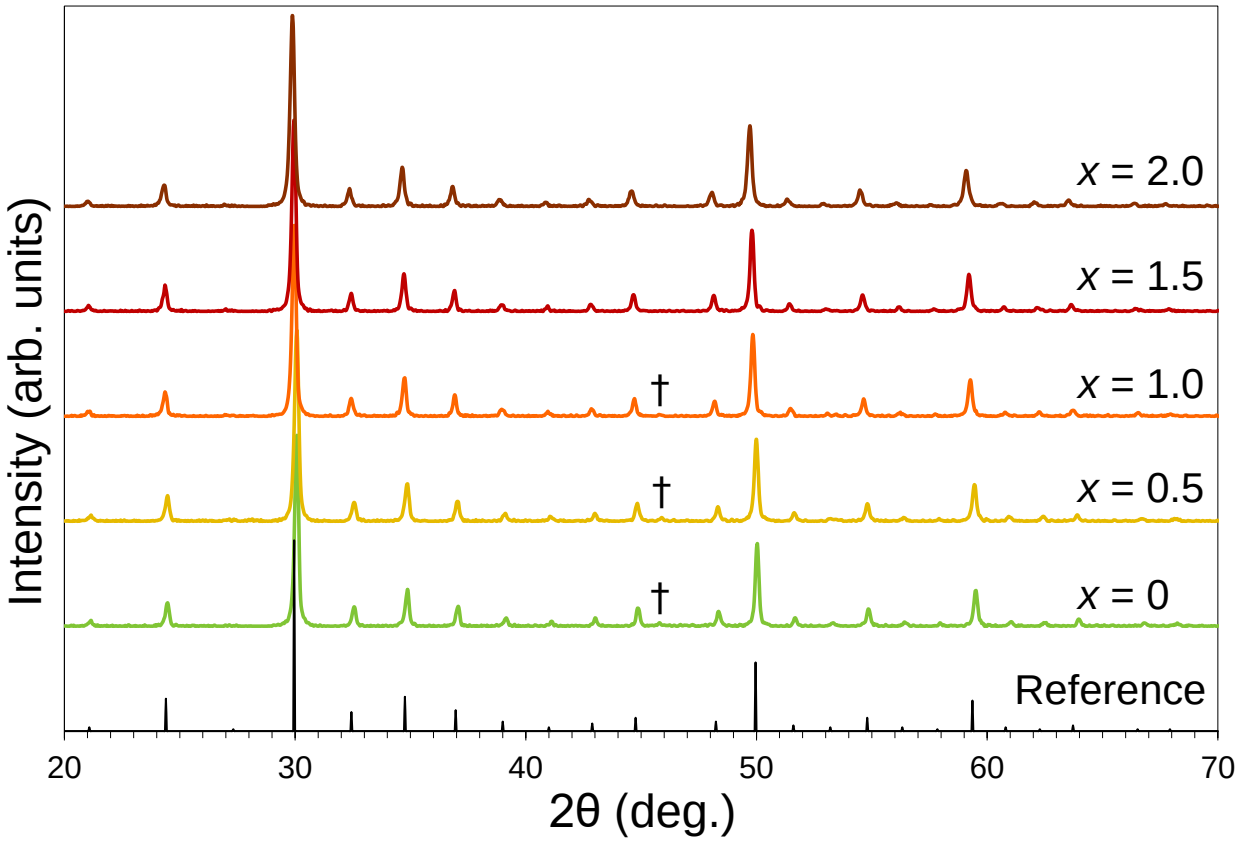

Figure 5.2: X-ray diffraction profiles of $Cu_{10}Ni_{2-x}Zn_xSb_4S_{13}$ ($x = 0$, 0.5, 1.0, 1.5, and 2.0) synthesized by mechanical alloying. Impurity peaks of NiS are marked by † symbols.

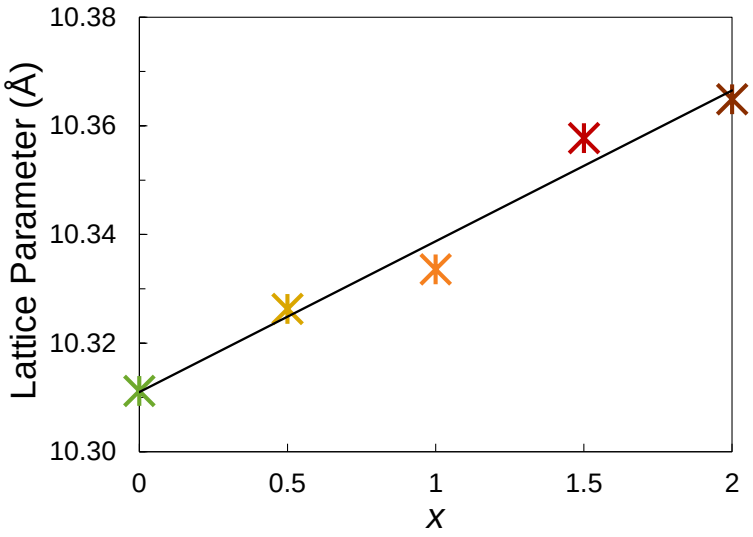

Figure 5.3: Lattice parameter of $Cu_{10}Ni_{2-x}Zn_xSb_4S_{13}$ ($x = 0$, 0.5, 1.0, 1.5, and 2.0) synthesized by mechanical alloying.

Elemental distribution maps, displayed in Figure 5.4, were obtained for the Zn and Ni end-members via energy-dispersive X-ray spectroscopy (EDS). EDS maps verify the incorporation of Ni and Zn dopants, and a high degree of homogeneity is observed in both samples. Furthermore, atomic distributions were determined by EDS for the entire $Cu_{10}Ni_{2-x}Zn_xSb_4S_{13}$ solid solution, and results are summarized in Table 5.1. All samples are slightly enriched on the metal site, demonstrating excessive Cu, Ni, and Zn content. On the other hand, Sb remains relatively close to the target concentration in all samples.

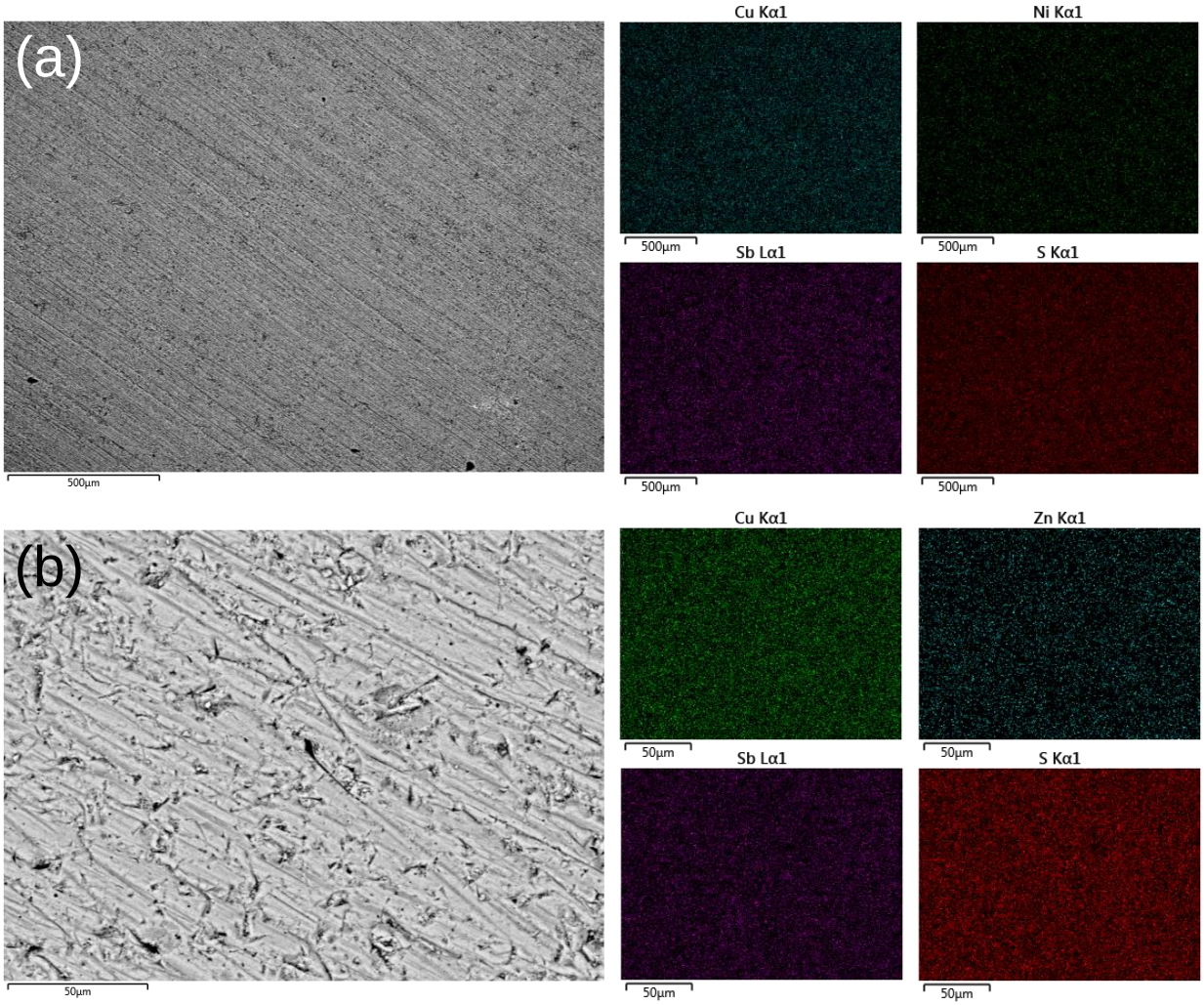

Figure 5.4: Energy-dispersive X-ray spectroscopy data of (a) $Cu_{10}Ni_2Sb_4S_{13}$ and (b) $Cu_{10}Zn_2Sb_4S_{13}$ synthesized by mechanical alloying. Electron microscopy images (left-side) display the sites where elemental distribution maps (right-side) were collected.

Target Composition	EDS Data
$Cu_{10}Ni_2Sb_4S_{13}$	$Cu_{10.4\pm0.6}Ni_{2.2\pm0.2}Sb_{4.0\pm0.3}S_{13.0\pm0.3}$
$Cu_{10}Ni_{1.5}Zn_{0.5}Sb_4S_{13}$	$Cu_{10.3\pm0.3}Ni_{1.6\pm0.2}Zn_{0.4\pm0.1}Sb_{4.0\pm0.2}S_{13.0\pm0.2}$
$Cu_{10}NiZnSb_4S_{13}$	$Cu_{10.6\pm0.4}Ni_{1.2\pm0.3}Zn_{0.9\pm0.2}Sb_{4.0\pm0.2}S_{13.0\pm0.3}$
$Cu_{10}Ni_{0.5}Zn_{1.5}Sb_4S_{13}$	$Cu_{10.2\pm0.5}Ni_{0.5\pm0.2}Zn_{1.6\pm0.3}Sb_{3.9\pm0.4}S_{13.0\pm0.4}$
$Cu_{10}Zn_2Sb_4S_{13}$	$Cu_{10.8\pm0.7}Zn_{2.2\pm0.4}Sb_{4.1\pm0.3}S_{13.0\pm0.2}$

Table 5.1: Energy-dispersive X-ray spectroscopy (EDS) data of $Cu_{10}Ni_{2-x}Zn_xSb_4S_{13}$ (x = 0, 0.5, 1.0, 1.5, and 2.0) synthesized by mechanical alloying.

5.2.2 Transport Property Characterization

Electrical transport data are presented in Figure 5.5. The linear trend of increasing thermopower (Figure 5.5a) with increasing temperature is characteristic of degenerate semiconductor behavior.[26] In general, these samples achieve similar values as those reported previously for Ni and Zn co-doped tetrahedrites (approximately 150–220 μVK^{-1} from 300 to 700 K).[90] Thermopower data for the $x = 2$ composition were excluded for visual clarity, but from 300 to 673 K, $Cu_{10}Zn_2Sb_4S_{13}$ demonstrates a constant thermopower of approximately 600 μVK^{-1}. The $x = 2$ composition demonstrates high thermopower because Zn doping raises the Fermi level into the band gap (by filling holes) in the electronic band structure.[66] Similarly, Ni doping leads to hole filling, but at the same time, additional Ni minority spin bands also become available above the Fermi level.[67] Thus, the highest thermopower is observed in $Cu_{10}Ni_{0.5}Zn_{1.5}Sb_4S_{13}$ due to the interplay between hole filling and additional available electronic states.

Deviations in thermopower data from metal-like behavior are related to higher electrical resistivity (Figure 5.5b). Mechanical alloying produces tetrahedrites with resistivity values (roughly 10^{-3} to 10^{-4}) on a similar order of magnitude to those reported by Lu et al. (about 5×10^{-5} Ωm) from 300 to 700 K.[90] In accordance with higher thermopower values,

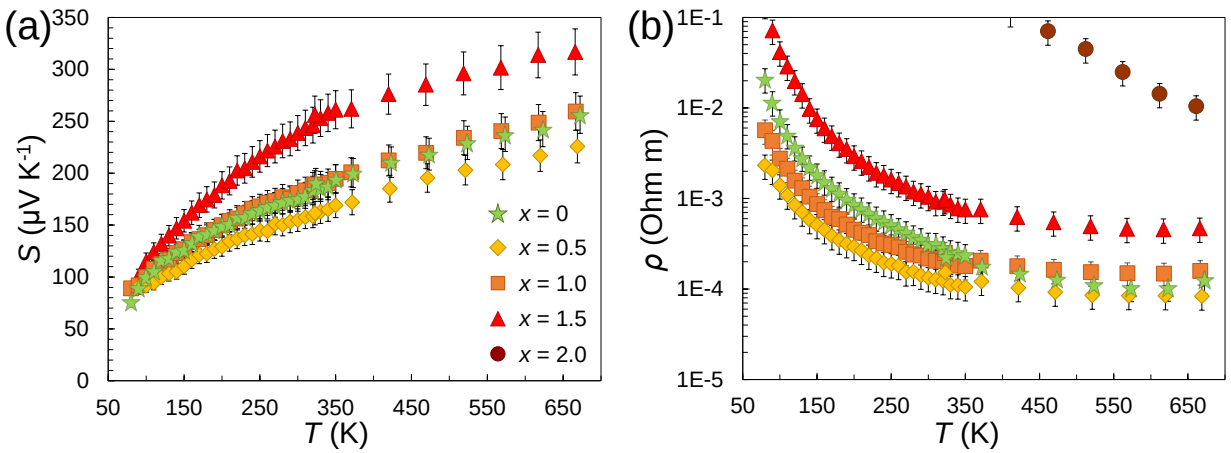

Figure 5.5: Electrical transport data of $Cu_{10}Ni_{2-x}Zn_xSb_4S_{13}$ ($x = 0$, 0.5, 1.0, 1.5, and 2.0) synthesized by mechanical alloying, where data for thermopower (S) and electrical resistivity (ρ) are shown in (a) and (b), respectively. Thermopower for the $x = 2$ sample, which has been excluded for visual clarity, is approximately 600 μVK^{-1} from 300 to 673 K.

Zn doping generally leads to higher electrical resistivity. As a result of hole filling via Zn doping, the Zn end-member is highly resistive. Low-temperature electrical measurements of this composition are especially difficult owing to its insulating properties. Hence, Ni and Zn co-doped tetrahedrites synthesized by mechanical alloying demonstrate electrical properties that are comparable to tetrahedrites synthesized by traditional methods.

Thermal transport data are illustrated in Figure 5.6. Evidently, the low-temperature radiation correction is not strong enough to match measurements between overlapping temperature regions. Regardless, all samples in the high-temperature region demonstrate values below 0.65 $Wm^{-1}K^{-1}$ from 300 to 700 K. After removing the electronic component from the total thermal conductivity, we observe lattice thermal conductivities that approach the theoretical minimum of 0.4 $Wm^{-1}K^{-1}$.[34] The values detailed here are in very good agreement with those by Lu et al. for Ni and Zn co-doped tetrahedrites. Therefore, $Cu_{10}Ni_{2-x}Zn_xSb_4S_{13}$ ($0 \geq x \geq 2$) fabricated by mechanical alloying demonstrate exceptionally low thermal conductivities.

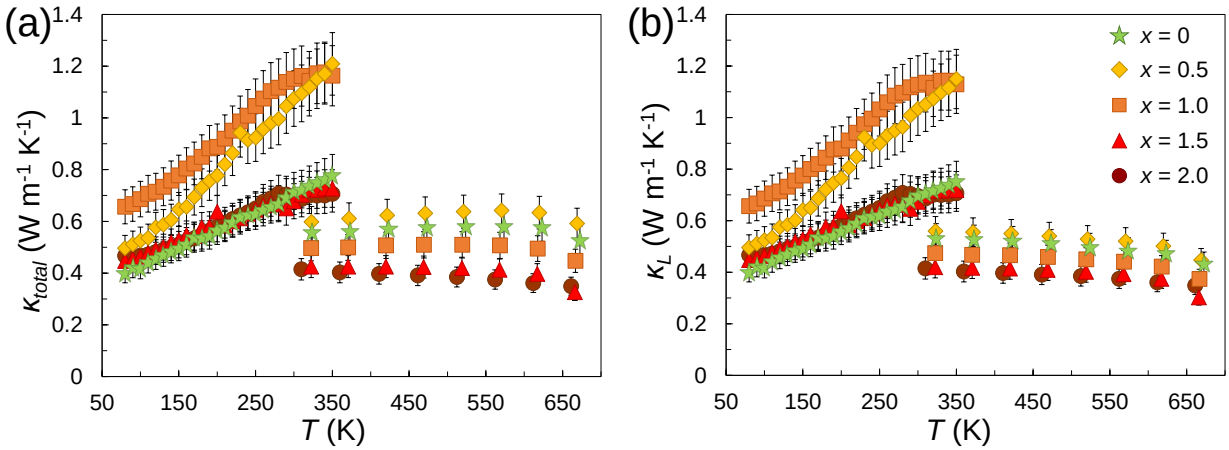

Figure 5.6: Thermal transport data of $Cu_{10}Ni_{2-x}Zn_xSb_4S_{13}$ (x = 0, 0.5, 1.0, 1.5, and 2.0) synthesized by mechanical alloying, where data for total thermal conductivity (κ_{total}) and lattice thermal conductivity (κ_L) are shown in (a) and (b), respectively.

Data for figure of merit (ZT) of the Ni and Zn co-doped solid solution are shown in Figure 5.7. The data generally indicate increasing ZT with decreasing Zn content. Our $Cu_{10}Ni_{2-x}Zn_xSb_4S_{13}$ solid solution demonstrates lower ZT values at 673 K than those of Lu et al.[90] We attribute these differences to lower power factors and slightly higher thermal conductivities in samples made by mechanical alloying. As a result of extremely high electrical resistivity, the $x = 2$ composition exhibits an abysmal ZT comparing to the other members of the solid solution. Ultimately, peak ZT of 0.66 was attained in $Cu_{10}Ni_2Sb_4S_{13}$ at 673 K. Therefore, the mechanical alloying synthesis approach is capable of producing a wide range of high-performance tetrahedrite TE materials in shorter time than the conventional furnace-ampule method.

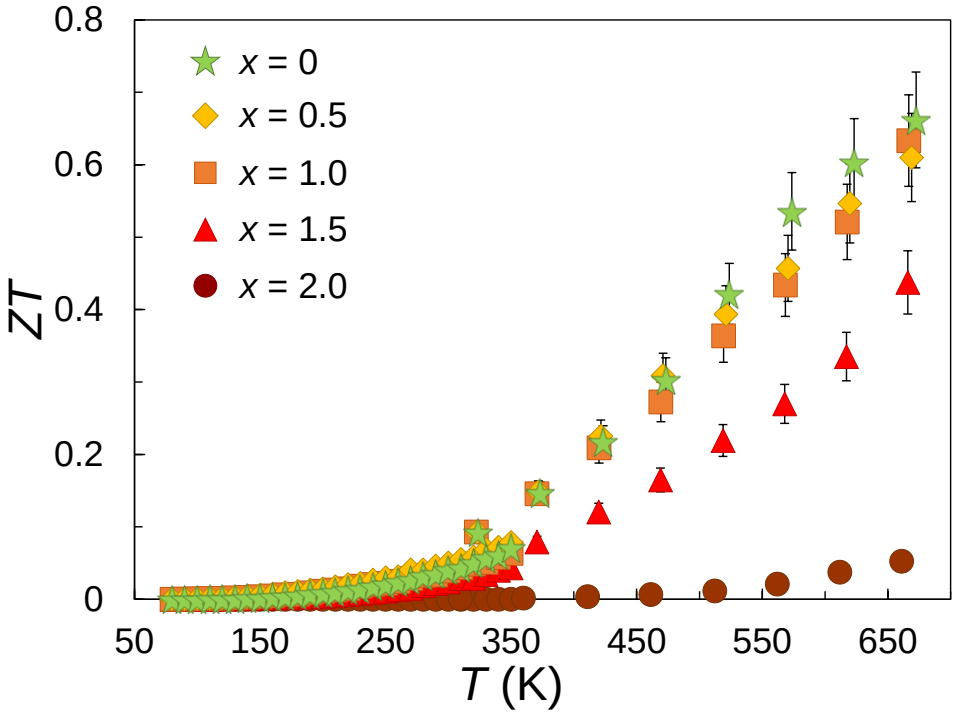

Figure 5.7: Figure of merit (ZT) data of $Cu_{10}Ni_{2-x}Zn_xSb_4S_{13}$ (x = 0, 0.5, 1.0, 1.5, and 2.0) synthesized by mechanical alloying.

5.3 $Cu_{12-x}Fe_xSb_4S_{13}$

For comparison with Fe-doped samples synthesized by the modified polyol process, a solid solution of $Cu_{12-x}Fe_xSb_4S_{13}$ (x = 0.5, 1.0, 1.3, 1.5, and 2.0) was prepared by mechanical alloying synthesis.[173] As discussed in Chapter 4, Fe assumes a nominally trivalent or divalent state in tetrahedrite depending on Fe concentration. We speculate that the extra donated electrons from $Fe^{3+/2+}$ dopants may engender n-type behavior in tetrahedrite materials. Certain compositions synthesized by the modified polyol process were shown to demonstrate negative thermopower values in the low-temperature regime, and we expect a similar outcome in Fe-doped tetrahedrites synthesized by mechanical alloying. Herein, we examine the TE properties of intermediate compositions of Fe-doped tetrahedrites, which have previously not been reported.

5.3.1 Structural and Compositional Characterization

X-ray diffraction profiles of Fe-doped tetrahedrites synthesized by mechanical alloying are illustrated in Figure 5.8. Samples with higher doping levels ($x = 1.3$, 1.5, and 2.0) demonstrate pure-phase tetrahedrite with no impurities detected. The $x = 1$ and $x = 0.5$ samples demonstrate mostly tetrahedrite as the primary phase, but secondary peaks of famatinite (Cu_3SbS_4) were also present in these samples with lower amounts of Fe. The XRD data again imply that the dopant atom, in this case Fe, is required to stabilize the tetrahedrite crystal structure.

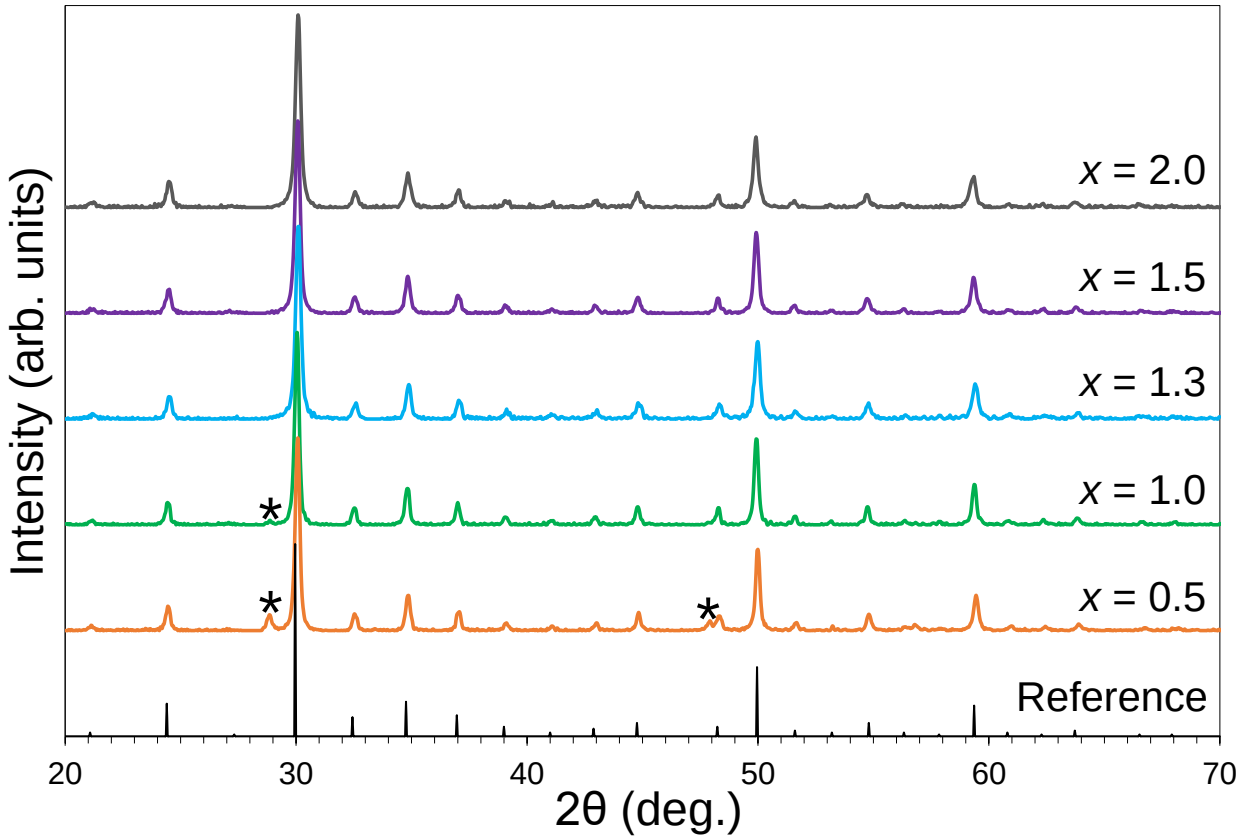

Figure 5.8: X-ray diffraction profiles of $Cu_{12-x}Fe_xSb_4S_{13}$ ($x = 0.5$, 1.0, 1.3, 1.5, and 2.0) synthesized by mechanical alloying. Primary peaks of Cu_3SbS_4 impurities are marked by $*$ symbols.

Compositional data were obtained via energy-dispersive X-ray spectroscopy (EDS) with

the $x = 1.3$ composition as a representative sample of the solid solution. Elemental distribution maps and a scanning electron microscopy image of the observation site are displayed in Figure 5.9. The sample is relatively homogeneous with respect to each element, including Fe dopant. In the Cu signal, noticeable shadowing effects result from contours in the sample surface. Numerical EDS data are provided in Table 5.2 for all Fe-doped samples synthesized by mechanical alloying. As was the case with Ni and Zn co-doped tetrahedrites, all samples exhibit enrichment on the metal site, with the greatest off-stoichiometry demonstrated by the $x = 0.5$ sample. It is worth noting that these data may be convoluted by the presence of secondary phases in samples with lower Fe concentrations. Regardless, all samples demonstrate compositions within the documented range of stability for tetrahedrites.

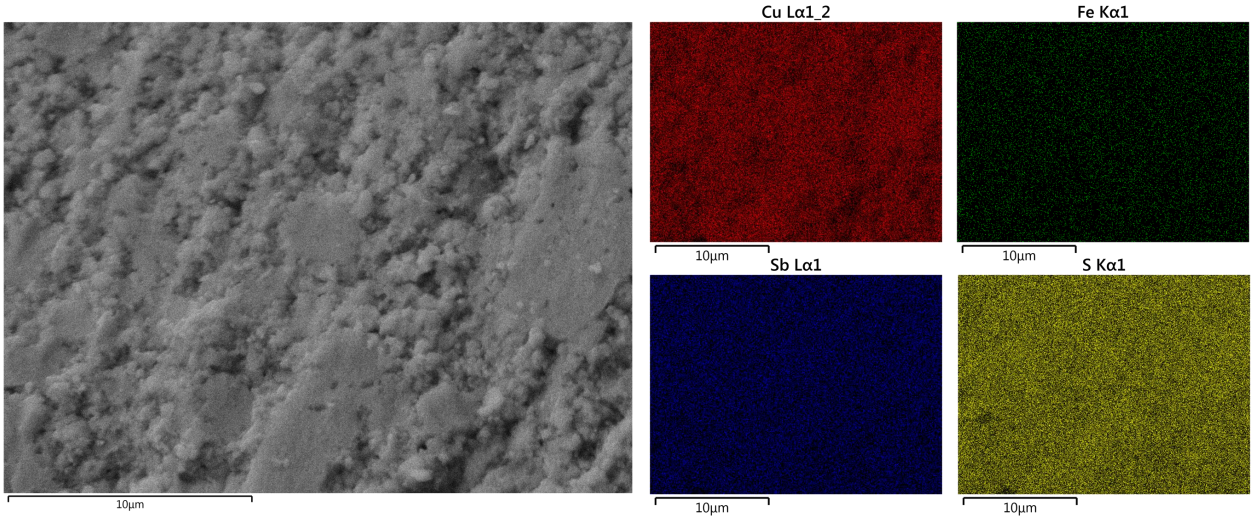

Figure 5.9: Energy-dispersive X-ray spectroscopy data of $Cu_{10.7}Fe_{1.3}Sb_4S_{13}$ synthesized by mechanical alloying. Electron microscopy image (left-side) displays the site where elemental distribution maps (right-side) were collected.

5.3.2 Transport Property Characterization

Electrical transport data are depicted in Figure 5.10 for Fe-doped tetrahedrites produced by the mechanical alloying approach. In terms of thermopower (Figure 5.10a), the $x =$

Target Composition	EDS Data
$Cu_{10}Fe_2Sb_4S_{13}$	$Cu_{11.1\pm0.9}Fe_{2.0\pm0.2}Sb_{3.8\pm0.2}S_{13.0\pm0.5}$
$Cu_{10.5}Fe_{1.5}Sb_4S_{13}$	$Cu_{10.9\pm0.4}Fe_{1.6\pm0.1}Sb_{4.3\pm0.2}S_{13.0\pm0.1}$
$Cu_{10.7}Fe_{1.3}Sb_4S_{13}$	$Cu_{11.8\pm0.4}Fe_{1.4\pm0.1}Sb_{4.1\pm0.1}S_{13.0\pm0.3}$
$Cu_{11}FeSb_4S_{13}$	$Cu_{11.6\pm0.5}Fe_{1.1\pm0.1}Sb_{4.5\pm0.1}S_{13.0\pm0.4}$
$Cu_{11.5}Fe_{0.5}Sb_4S_{13}$	$Cu_{12.6\pm0.2}Fe_{0.5\pm0.1}Sb_{4.0\pm0.2}S_{13.0\pm0.2}$

Table 5.2: Energy-dispersive X-ray spectroscopy (EDS) data of $Cu_{12-x}Fe_xSb_4S_{13}$ ($x = 0.5$, 1.0, 1.3, 1.5, and 2.0) synthesized by mechanical alloying.

1.0, 1.3, and 2.0 data converge to about 230 μVK^{-1} at 673 K, whereas the $x = 0.5$ and 1.5 samples reach approximately 170 μVK^{-1} at the highest temperature. Electrical resistivity (Figure 5.10b) demonstrates semiconductor-like behavior in samples with $x \geq 1.0$, while the $x = 0.5$ sample demonstrates metallic behavior with a relatively constant electrical resistivity over the entire temperature range. At 673 K, the solid solution follows a trend of increasing electrical resistivity with increasing Fe content, suggesting that higher doping levels yield greater values of resistivity. Moreover, these values on par with those reported elsewhere for the fully substituted composition.[55, 89] The $x = 0.5$ data is in very good agreement with data reported by Tippireddy et al. ($\rho \approx 3 \times 10^{-5}$ Ωm and $S \approx 130 - 170$ μVK^{-1}) from 350 to 700 K.[70] Density-functional theory calculations indicate that the Fermi level likely remains well within the valence band manifold at the $x = 0.5$ composition, granting properties similar to the undoped composition.[70] Indeed, the linear thermopower data indicate metal-like characteristics in $Cu_{11.5}Fe_{0.5}Sb_4S_{13}$. Thus, mechanical alloying may be used to synthesize tetrahedrites with decent electrical properties at high temperatures.

Furthermore, the data in Figure 5.10a reflect unique electrical behavior at low temperatures. Similar to samples made by the modified polyol process, a transition from p-type to n-type conductivity is observed in certain mechanically alloyed samples as temperature decreases. Accordingly, this conductivity transition is independent of the synthetic method

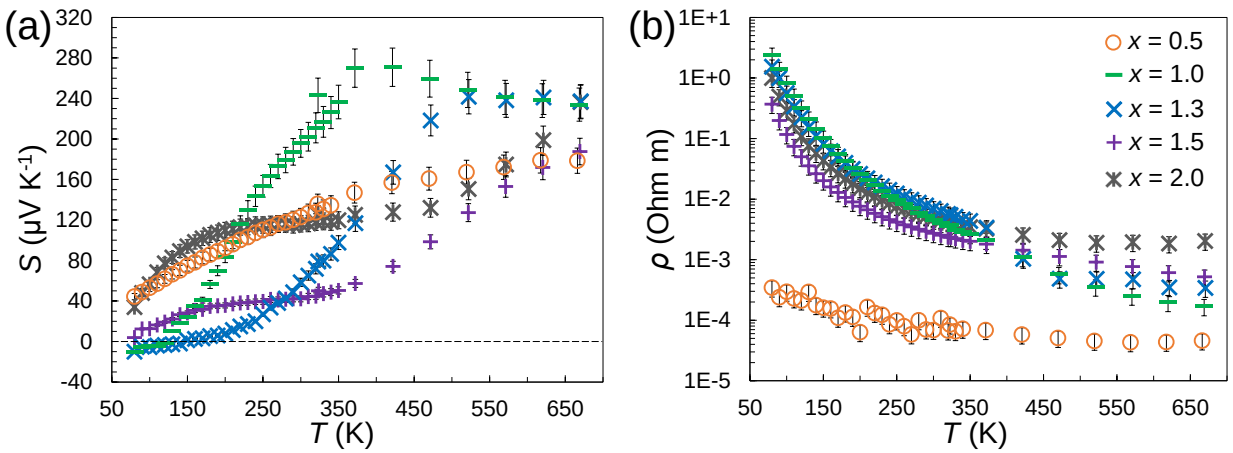

Figure 5.10: Electrical transport data of $Cu_{12-x}Fe_xSb_4S_{13}$ ($x = 0.5$, 1.0, 1.3, 1.5, and 2.0) synthesized by mechanical alloying, where data for thermopower (S) and electrical resistivity (ρ) are shown in (a) and (b), respectively.

used to produce tetrahedrites. Previously, other copper chalcogenide materials have been reported to demonstrate a similar phenomenon.[174, 175] Crossover temperatures were determined to be 120 K and 150 K for the $x = 1.0$ and $x = 1.3$ samples, respectively; and both compositions reach a minimum value of $-10\,\mu VK^{-1}$ at 80 K. This set of samples allows for a more complete representation of the influence of Fe-doping across a large range of compositions. While the $x = 0.5$ sample has metal-like qualities, the other samples move toward and then away from n-type behavior as Fe concentration increases. In the fully substituted end-member, doping with Fe alters the material properties similar to Zn doping. In intermediate compositions, available Fe minority electronic states and hole filling via Fe doping engender the onset of n-type conductivity at low temperatures. Again, the n-type to p-type transition temperature is believed to be related to composition, and liquid He cryostat measurements could be helpful in analyzing these materials below 80 K. Regardless, the temperature dependent decrease in thermopower and increase in electrical resistivity implies that electrons and holes are competing as the dominant charge carrier in these Fe-doped tetrahedrites.

Thermal transport data for the $Cu_{12-x}Fe_xSb_4S_{13}$ ($0.5 \leq x \leq 2.0$) solid solution are

shown in Figure 5.11. A weak radiation correction leads to the offset between low-temperature and high-temperature data, but still the cryostat data qualitatively match the compositional trend demonstrated by LFA data. From 300 to 700 K, all samples demonstrate exceptionally low thermal conductivity below 0.5 $Wm^{-1}K^{-1}$, except for the $x = 0.5$ sample, which demonstrates thermal conductivity lower than 0.7 $Wm^{-1}K^{-1}$. After subtracting the electronic component from the total thermal conductivity, lattice thermal conductivity data for all samples converge at 673 K. All samples exhibit lattice thermal conductivity near the theoretical minimum calculated by theory.[34] Kim et al. noted a reduction in particle size after precursors underwent ball milling, and it is possible that nanostructuring effects occur in samples exposed to prolonged ball milling.[94] Therefore, small grain sizes combined with non-ideal density may be a source of ultra-low lattice thermal conductivity demonstrated by mechanically alloyed Fe-doped tetrahedrites.

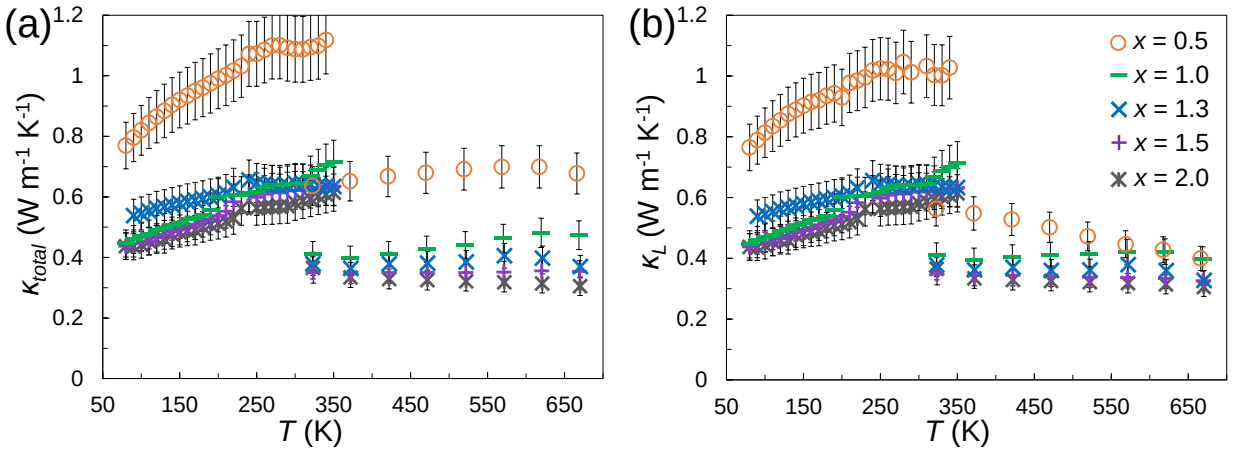

Figure 5.11: Thermal transport data of $Cu_{12-x}Fe_xSb_4S_{13}$ ($x = 0.5$, 1.0, 1.3, 1.5, and 2.0) synthesized by mechanical alloying, where data for total thermal conductivity (κ_{total}) and lattice thermal conductivity (κ_L) are shown in (a) and (b), respectively.

As has been shown repeatedly throughout this report, the most remarkable feature of tetrahedrites are the unusually low, "glass-like" thermal conductivity they maintain while

simultaneously exhibiting electrical properties more typical of a crystalline semiconductor. Figure 5.12 displays figure of merit (ZT) data for the $Cu_{12-x}Fe_xSb_4S_{13}$ ($0.5 \leq x \leq 2.0$) solid solution synthesized by mechanical alloying. At 673 K, data follow a trend of decreasing ZT with increasing Fe concentration. Aside from the $x = 0.5$ compositions, the mechanically alloyed samples generally demonstrate lower ZT than polyol samples, and discrepancies mostly arise from differences in electrical power factors. Variations between samples made by alternative syntheses are primarily attributed to differences in chemical composition. Ultimately, an optimal ZT value of 0.68 was obtained for $Cu_{11.5}Fe_{0.5}Sb_4S_{13}$ at 673 K. Hence, mechanical alloying may be used to synthesize Fe-doped tetrahedrite materials in faster times and with less energy than the traditional melt-recrystallization method.

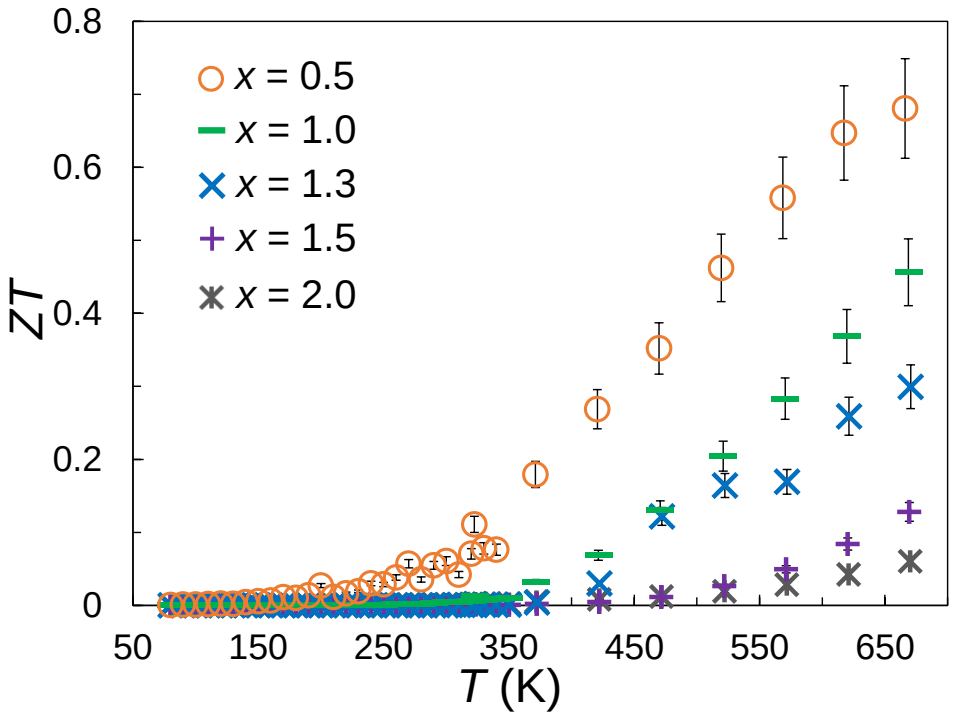

Figure 5.12: Figure of merit (ZT) data of $Cu_{12-x}Fe_xSb_4S_{13}$ ($x = 0.5$, 1.0, 1.3, 1.5, and 2.0) synthesized by mechanical alloying.

5.3.3 Electron Exchange in Fe-doped Tetrahedrites

Herein, the recently discovered electron exchange phenomenon observed in Fe-doped tetrahedrites will be addressed, along with its potential effects on TE properties. Nasonova et al. used Mössbauer spectroscopy to provide evidence for the presence of mixed valence Fe^{2+} and Fe^{3+} cations in $Cu_{12-x}Fe_xSb_4S_{13}$, even at higher Fe concentrations ($x = 1.5$ and 2.0).[103] On the other hand, strictly Fe^{3+} was detected in tetrahedrites with lower Fe concentration ($x = 0.8,\ 1.0,$ and 1.2). They also observed electron hopping between Fe cations at 300 K, which freezes out by 77 K, leaving non-interacting Fe^{3+} and high-spin Fe^{2+} centers. In a follow-up study, Sobolev and many of the same coworkers studied the thermally activated electron exchange in Fe-doped tetrahedrites.[180] Mössbauer measurements allowed for direct determination of the activation energy for electron transfer, which was found to be dependent on chemical composition. Very recently, Guler et al. attempted to use electron paramagnetic resonance to demonstrate an exchange-coupled pair of Fe^{3+} and Cu^{2+} cations.[106] They also paired TE measurements with magnetic characterization and attained a peak ZT value of 0.6 for $Cu_{11}FeSb_4S_{13}$ at 550 K. Regardless, recent observations of temperature-dependent electron hopping could significantly influence TE behavior in Fe-doped tetrahedrites.

The author hypothesizes that low-temperature n-type behavior in mechanically alloyed and modified polyol Fe-doped tetrahedrites is a consequence of electron hopping, in addition to minority spin band conduction and hole filling via Fe doping. As temperature increases, thermally activated charge transfer becomes more prominent and lowers electrical resistivity in Fe-doped tetrahedrites at higher temperatures. For example, the $x = 1.5$ polyol sample demonstrated n-type behavior over a large temperature range (80 to 310 K). We propose that this sample, which has a greater concentration of Fe^{2+} and Fe^{3+} centers, counteracts

hole formation by enabling more pathways for electron hopping. Accordingly, the primary mechanisms of charge transport that cause n-type behavior in Fe-doped tetrahedrites are excitation of electrons into minority spin bands, hole filling via doping, and electron hopping.

In an attempt to better understand the mechanism by which electrical charge is conducted in Fe-doped tetrahedrites at low-temperature, we comparatively analyze two models of charge transfer: an Arrhenius thermally activated hopping model and a Mott variable-range hopping model. The samples of $Cu_{12-x}Fe_xSb_4S_{13}$ that demonstrated n-type conductivity (polyol: $x = 1.0$ and 1.5; mechanical alloying: $x = 1.0$ and 1.3) were chosen for analysis. First, an Arrhenius model may be used to describe the dominant charge transport mechanism as a thermally activated hopping process.[175] Assuming a constant carrier concentration, the electrical conductivity (σ) is defined by Equation 5.1.

$$\sigma = \sigma_0 \exp\left(\frac{-E_A}{k_B T}\right) \tag{5.1}$$

In the above equation, σ_0 is the residual conductivity at 0 K, k_B is the Boltzmann constant, E_A is the activation energy for charge transfer, and T is temperature. Analysis of low-temperature electrical data by an Arrhenius model is illustrated in Figure 5.13a. In general, greater Fe concentration was related to lower E_A values for both synthetic approaches, supporting the claim that the increased presence of Fe^{2+} and Fe^{3+} centers facilitates hopping. However, our resulting E_A values are an order of magnitude different than those reported by Sobolev et al.[180] Admittedly, analysis by the Arrhenius model is convoluted by a mixture of electron hopping and standard band conduction.

Contrastingly, we analyzed the low-temperature electrical properties of n-type Fe-doped tetrahedrites by a Mott variable-range hopping model as well. According to the variable-

range charge transport mechanism, electrical conductivity (σ) is defined by Equation 5.2, where σ_0 is the high-temperature limit of the conductivity and T_0 is the Mott temperature.[181]

$$\sigma = \sigma_0 \exp\left(\frac{-T_0}{T}\right)^{1/4} \tag{5.2}$$

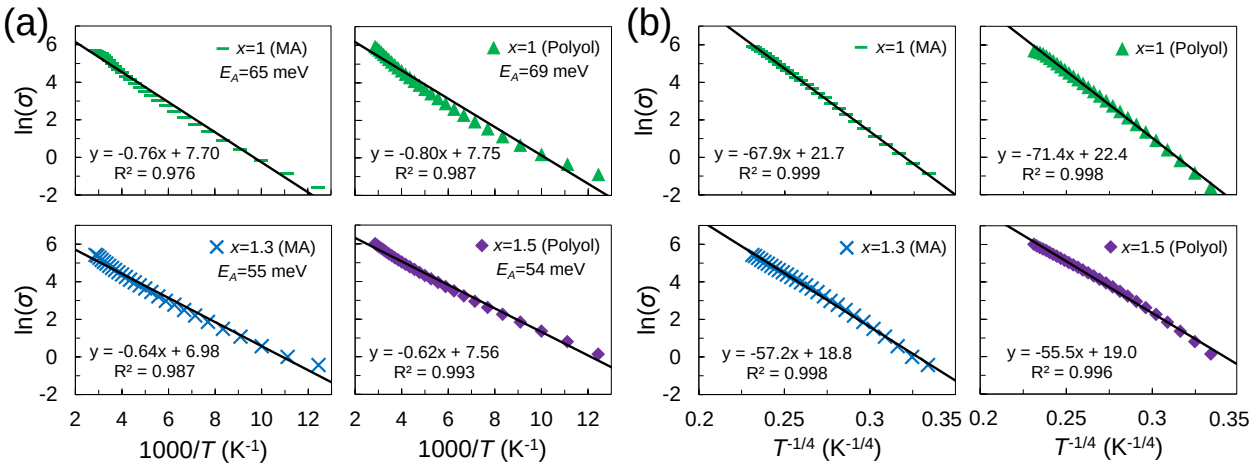

Figure 5.13: Comparative analysis of charge transport by (a) an Arrhenius model for thermally activated charge carriers and (b) a Mott variable-range hopping model for $Cu_{12-x}Fe_xSb_4S_{13}$ from 80 to 350 K synthesized by mechanical alloying (MA) and modified polyol process (Polyol). Data symbols match the corresponding symbols used in Chapters 4 and 5. According to the Arrhenius model in (a), activation energy (E_A) for electron transfer is determined from the slope of the linear trendline.

Analyses of electrical data by the variable-range hopping model are depicted in Figure 5.13b. The Mott model provides a better fit to the data, and deviations from the model are mostly attributed to the entanglement of hopping and band conduction. In general, these Fe-doped tetrahedrites are near the so-called "mobility edge," at which the dominant charge transport mechanism transitions from hopping at low temperatures to band transport at high temperatures. While both charge transfer models qualitatively describe the data, the Mott model yields a better fit. Therefore, variable-range hopping is likely the dominant charge transport mechanism in these Fe-doped tetrahedrites at low temperatures.

These findings allow for pressing further into understanding the requirements for designing n-type tetrahedrites. Magnetization measurements would be of interest to shed light on the charge states of cations in Fe-doped tetrahedrites. By combining magnetic measurements with TE characterization, one can elucidate the relationship between Fe doping and TE transport properties. Recently, Guler et al. simulataneously characterized TE and magnetic properties (via electron spin resonance) in Fe-doped tetrahedrites from 300 to 600 K.[106] However, they did not present results below 300 K, leaving the unique electron exchange phenomenon in Fe-doped tetrahedrites relatively enigmatic. The analyses presented in this report are preliminary and would strongly benefit from liquid He cryostat measurements, which are capable of characterization down to 4 K. The potential that tetrahedrite shows as a high performing p-type TE at intermediate temperatures, in combination with its low toxicity and high elemental abundance, warrants continued investigation of these technologically important materials.

Chapter 6

Reactive Spark Plasma Sintering Synthesis

The lengthy reaction time and extensive annealing required for traditional tetrahedrite synthesis is a major obstacle that impedes its application on a commercial scale. Herein, a reactive spark plasma sintering (SPS) method, which is significantly faster and easier than the conventional approach, is proposed and investigated. This novel approach can be scaled up to a large degree as well. Throughout the chapter, an exploration of Ni and Zn co-doped tetrahedrites synthesized by reactive SPS will be presented. In general, this technique is capable of fabricating tetrahedrite TE bulk materials in less than two hours, from start to finish. Accordingly, reactive SPS is highly amenable to commercial implementation, as it only requires ball milling and spark plasma sintering, with no heat treatment of any form.

To start, an overview of reactive SPS will be given, and then, findings from the investigation of $Cu_{10}Ni_{2-x}Zn_xSb_4S_{13}$ ($0 \leq x \leq 2$) will be disseminated. Specifically, information regarding process optimization and the formation of tetrahedrite throughout this process will be shared. As a complementary study, material properties of Ni and Zn co-doped tetrahedrites synthesized by reactive SPS may be compared with data from samples produced by mechanical alloying (Chapter 5). Much of the data presented here may be found in the *Journal of Alloys and Compounds* article by Weller and Morelli.[148]

6.1 Background on Reactive SPS

Reactive SPS is a method that rapidly synthesizes materials in a single step. Whereas other approaches trivially use SPS for powder consolidation, a chemical reaction takes place in the reactive approach. In general, SPS is relatively novel technique with much of the technological development and applied research occurring after the year 2000.[149] "Spark plasma sintering" is somewhat of a misnomer, since no spark is actually detectable from this method. Instead, many researchers have used the terms "field-assisted sintering technique" or "pulsed electric current sintering."[150] In particular, reactive SPS is useful for working with ultra high temperature ceramics, which require reaction temperatures that are otherwise difficult to reach by means of traditional furnace heating.[182] Previously, reactive SPS has been used for the synthesis of composites and a variety of borides, carbides, nitrides, oxides, and silicides.[183–189] As a result, this approach has been used for a wide range of applications in materials science. Nanocrystalline materials especially benefit from SPS methods because the rapid-nature of the sintering process mitigates grain coarsening.

Numerous groups have used SPS for densification of tetrahedrite materials, but there are very few studies using sintering as a synthetic approach for forming tetrahedrites. Battiston et al. published a one step sintering synthesis for Ni and Zn substituted tetrahedrites, which is very similar to the work reported in this chapter.[190] They used open die pressing as a fast and simple method for obtaining doped tetrahedrites in less than 6 h. It should also be noted that their Ni substituted samples exhibited secondary phases of NiSbS and Cu_2S. In the end, the best ZT for Ni and Zn co-doped tetrahedrites prepared by open die pressing was 0.65 at 673 K for $Cu_{11}NiZnSb_4S_{13}$.[190] Thus, reactive SPS as a synthetic approach for obtaining tetrahedrites remains relatively unexplored.

6.2 $Cu_{10}Ni_{2-x}Zn_xSb_4S_{13}$

The solid solution of $Cu_{10}Ni_{2-x}Zn_xSb_4S_{13}$ ($0 \leq x \leq 2$) was chosen in order to explore compositions of tetrahedrites similar to $Cu_{10.5}NiZn_{0.5}Sb_4S_{13}$, which exhibited a record high ZT for tetrahedrite materials.[66] As was shown with mechanical alloying (Chapter 4), Ni and Zn demonstrate distinct doping effects in tetrahedrites that can be fine-tuned to optimize TE performance. Additionally, these dopants tend to stabilize the tetrahedrite structure, and as such, they are appropriate compositions for the exploration of novel synthetic approaches. Whereas the other syntheses in this report utilize elemental S as a precursor, this reactive SPS procedure uses binary sulfides, since the volatilization of S during ball milling could lead to S deficiency in the final product.

6.2.1 Structural and Compositional Characterization

The $x = 2$ composition of $Cu_{10}Ni_{2-x}Zn_xSb_4S_{13}$ was used for pioneering the reactive SPS synthesis. X-ray diffraction profiles in Figure 6.1 depict the tetrahedrite phase evolution after 1 h of ball milling and at various subsequent SPS time intervals. After the ball milling step, some mechanical alloying has occurred, with mostly the famatinite (Cu_3SbS_4) and tetrahedrite ($Cu_{12}Sb_4S_{12}$) crystal structures being detected. This was found to be the case, to varying degrees, for all samples in the solid solution after 1 h of ball milling (see Figure A4 of the Appendix). As the sample underwent longer SPS, the impurity peak diminishes and pure tetrahedrite emerges as the dominant phase. Through process optimization, 30 min of SPS was determined to be the necessary sintering time to obtain high-purity tetrahedrite.

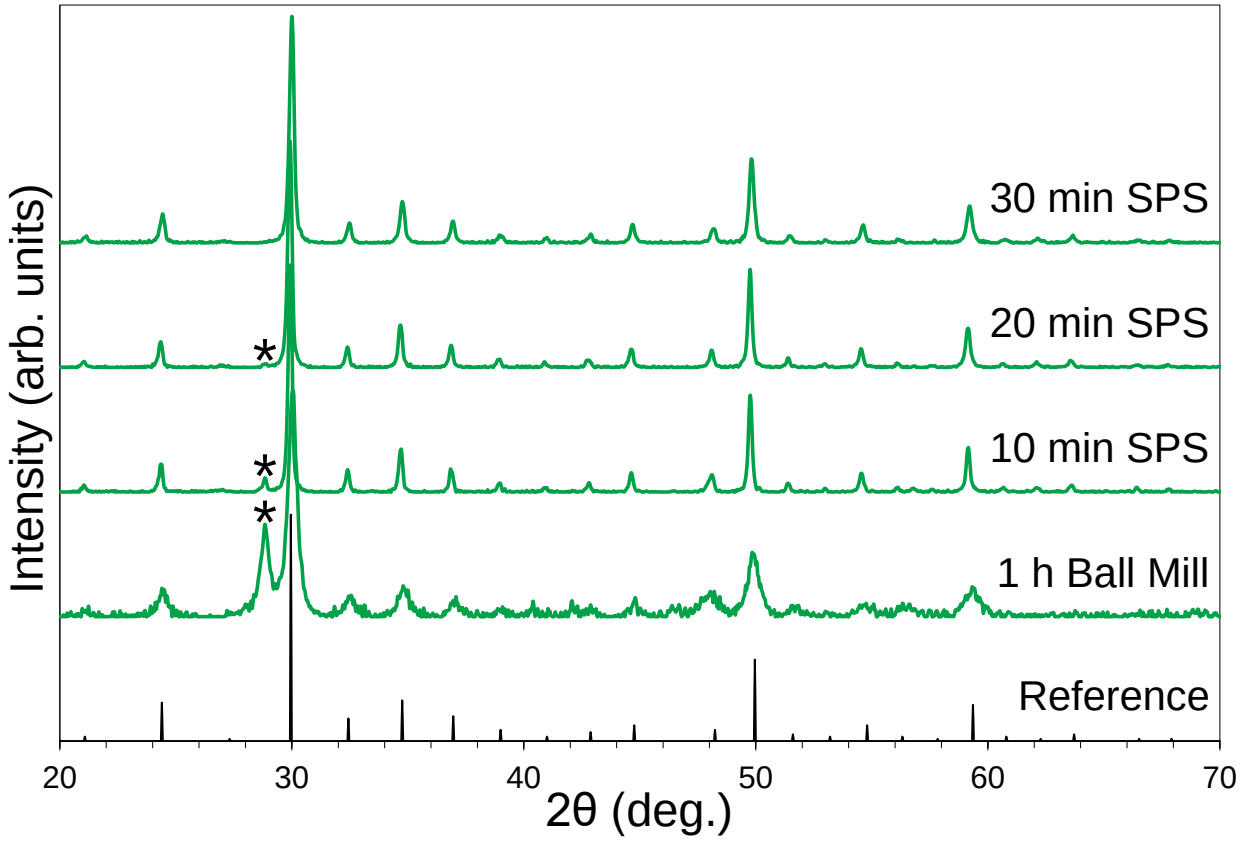

Figure 6.1: X-ray diffraction profiles of $Cu_{10}Zn_2Sb_4S_{13}$ after 1 h of vibratory ball milling and 10, 20, and 30 min of spark plasma sintering (SPS). Primary peaks of Cu_3SbS_4 impurities are marked by $*$ symbols.

Figure 6.2 illustrates the X-ray diffraction profiles for all samples after 30 min of reactive SPS. In the Zn-doped end-member, single-phase tetrahedrite is observed. The Ni-substituted end-member and intermediate compositions display secondary phases of NiSbS and NiS2, respectively. These impurities are a consequence of thermodynamic formation energies, and could potentially be removed by adjusting sintering parameters (i.e., temperature, pressure, hold time). A shift to lower 2θ values is observed as Zn content increases, and lattice parameter calculations are displayed in Figure 6.3. According to Vegard's law, a linear relationship is demonstrated between lattice parameter and chemical composition. Ultimately, the samples made by reactive SPS agree extremely well with our results from mechanical alloying.

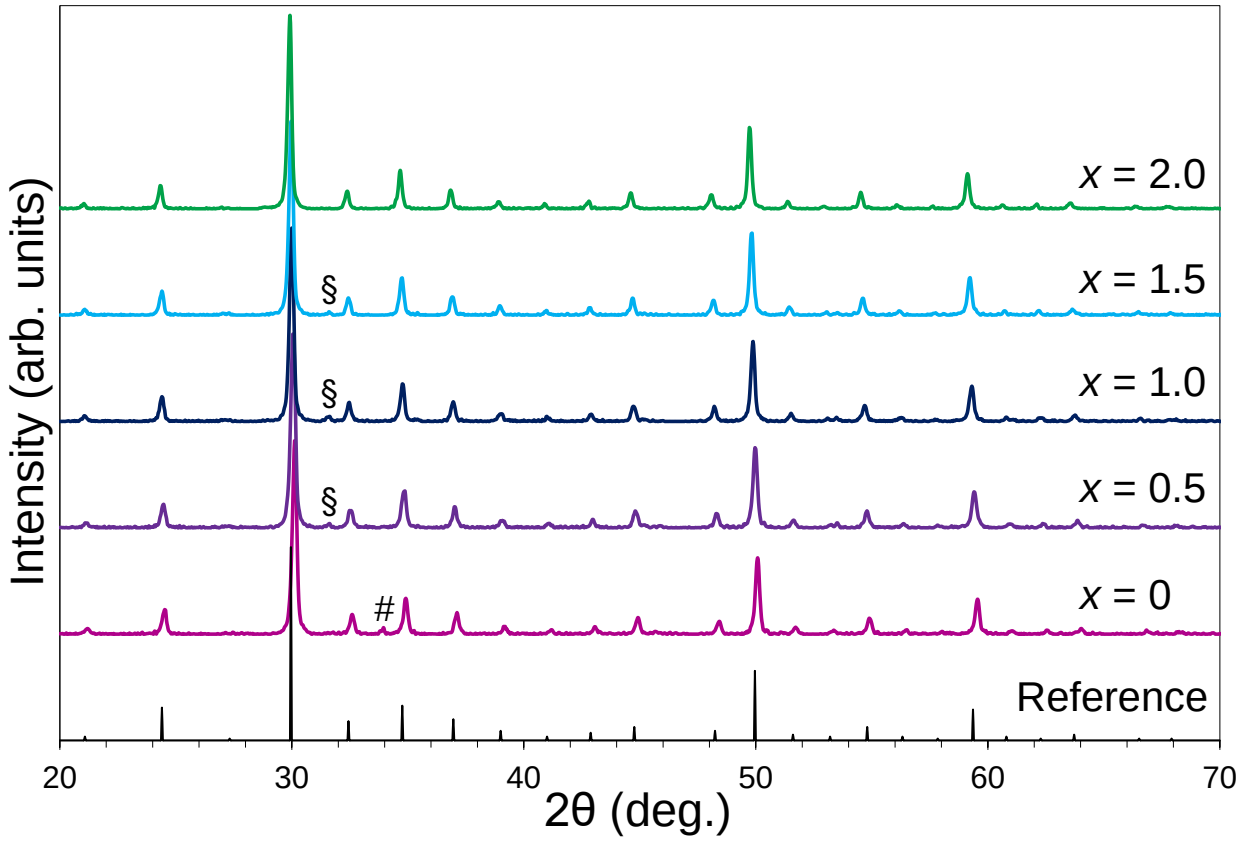

Figure 6.2: X-ray diffraction profiles of $Cu_{10}Ni_{2-x}Zn_xSb_4S_{13}$ (x = 0, 0.5, 1.0, 1.5, and 2.0) synthesized by reactive spark plasma sintering. Impurity peaks of NiSbS and NiS_2 are marked by # and § symbols, respectively.

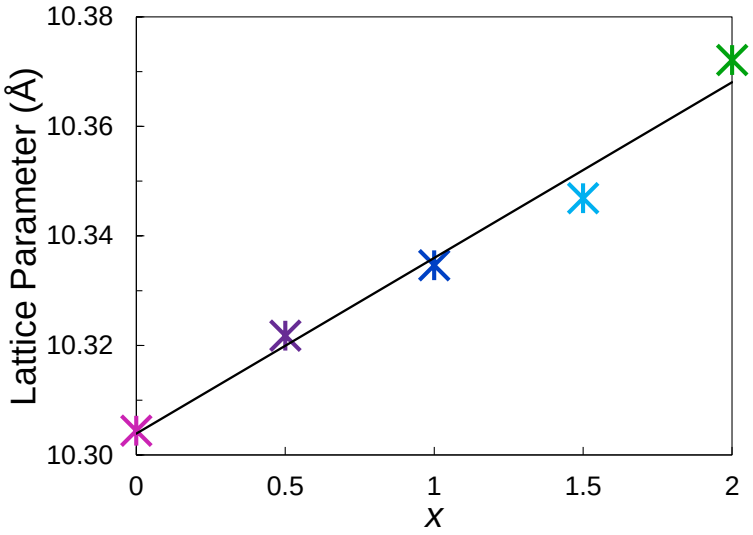

Figure 6.3: Lattice parameter of $Cu_{10}Ni_{2-x}Zn_xSb_4S_{13}$ (x = 0, 0.5, 1.0, 1.5, and 2.0) synthesized by reactive spark plasma sintering.

Elemental distribution maps of the Ni and Zn end-members of $Cu_{10}Ni_{2-x}Zn_xSb_4S_{13}$ ($0 \leq x \leq 2$) are shown in Figure 6.4. Large Sb precipitates were detected in the $x = 0$ composition, and although this Sb phase was not detected by XRD, it likely originates from unreacted elemental Sb (a precursor for the reactive SPS synthesis). Regardless, the majority phase for the $x = 0$ sample demonstrates uniform distribution with regards to Cu, Sb, S, and the dopant (Ni). On the other hand, the $x = 2$ sample demonstrates incorporation of the Zn dopant, as well as uniform chemical distribution throughout the bulk of the material.

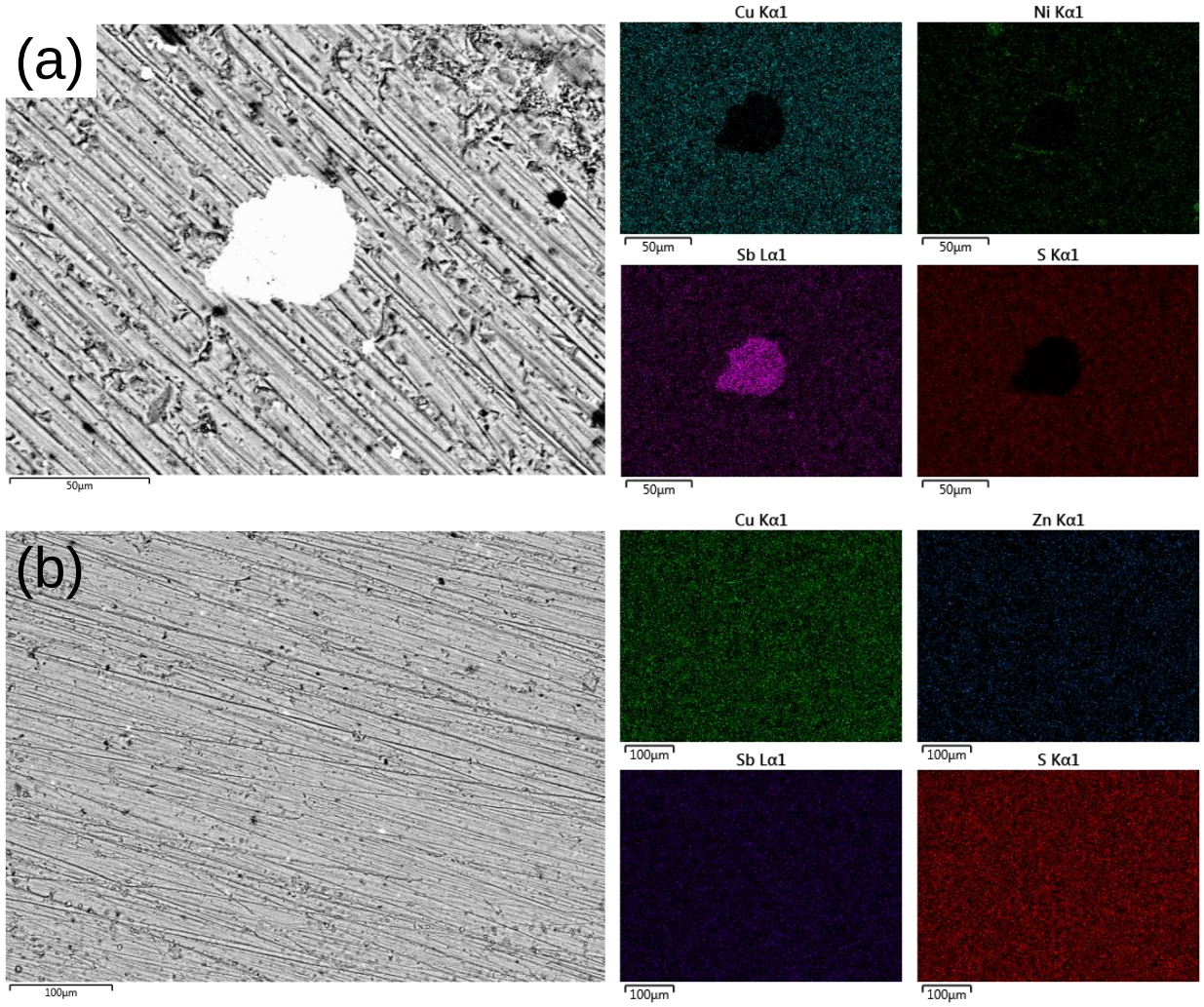

Figure 6.4: Energy-dispersive X-ray spectroscopy data of (a) $Cu_{10}Ni_2Sb_4S_{13}$ and (b) $Cu_{10}Zn_2Sb_4S_{13}$ synthesized by reactive spark plasma sintering. Electron microscopy images (left-side) display the sites where elemental distribution maps (right-side) were collected.

Quantitative data for chemical compositions of the $Cu_{10}Ni_{2-x}Zn_xSb_4S_{13}$ solid solution are summarized in Table 6.1. As with the other synthetic approaches, enrichment on the metal site is observed. Still, the dopant level remains close to the target amount, and there is little variation in Sb and S content between the samples. All compositions determined by EDS are within the reported range of stability for tetrahedrites.

Target Composition	EDS Data
$Cu_{10}Ni_2Sb_4S_{13}$	$Cu_{10.8\pm0.5}Ni_{2.1\pm0.3}Sb_{4.2\pm0.2}S_{13.0\pm0.4}$
$Cu_{10}Ni_{1.5}Zn_{0.5}Sb_4S_{13}$	$Cu_{10.5\pm0.5}Ni_{1.6\pm0.2}Zn_{0.5\pm0.3}Sb_{4.1\pm0.3}S_{13.0\pm0.5}$
$Cu_{10}NiZnSb_4S_{13}$	$Cu_{10.4\pm0.6}Ni_{1.1\pm0.3}Zn_{1.0\pm0.4}Sb_{4.0\pm0.3}S_{13.0\pm0.4}$
$Cu_{10}Ni_{0.5}Zn_{1.5}Sb_4S_{13}$	$Cu_{10.5\pm0.5}Ni_{0.5\pm0.2}Zn_{1.6\pm0.4}Sb_{4.0\pm0.3}S_{13.0\pm0.3}$
$Cu_{10}Zn_2Sb_4S_{13}$	$Cu_{10.4\pm0.6}Zn_{2.0\pm0.3}Sb_{4.1\pm0.3}S_{13.0\pm0.4}$

Table 6.1: Energy-dispersive X-ray spectroscopy (EDS) data of $Cu_{10}Ni_{2-x}Zn_xSb_4S_{13}$ (x = 0, 0.5, 1.0, 1.5, and 2.0) synthesized by reactive spark plasma sintering.

6.2.2 Transport Property Characterization

Electrical transport data for the Ni and Zn co-doped tetrahedrites made by reactive SPS are represented in Figure 6.5. While the thermopower and resistivity demonstrated by $Cu_{10}Zn_2Sb_4S_{13}$ are outside of the bounds of the plot, the vertical range was chosen to enhance visual clarity and allow for easy comparison between reactive SPS and mechanical alloying syntheses. In the high-temperature regime, samples demonstrate metal-like behavior with a linear rise in thermopower as temperature increases. Good agreement was found between measurements at low and high temperatures, strengthening the veracity of these data. Low-temperature thermopower data for the $x = 2$ composition were omitted because the signal was very noisy owing to the highly resistive nature of this composition. At higher levels of Zn doping (x = 1.5 and 2.0) samples demonstrates a higher thermopower consistent with a hole filling effect. This is attributed to the replacement of monovalent Cu ions

with divalent Zn dopants, which pushes the Fermi level into the band gap.[66] Simultaneously, Ni doping unlocks new electronic states, which convolute the overall effect of doping. $Cu_{10}Ni_{0.5}Zn_{1.5}Sb_4S_{13}$ demonstrates the highest thermopower, aside from the $x = 2$ composition, reflecting the complex multivalley character of the Ni valence band manifold combined with the shifted Fermi level via Zn doping. Overall, these data demonstrate similar thermopower values (150–220 μVK^{-1}) to those observed previously for tetrahedrites synthesized by the tradtional method.[66]

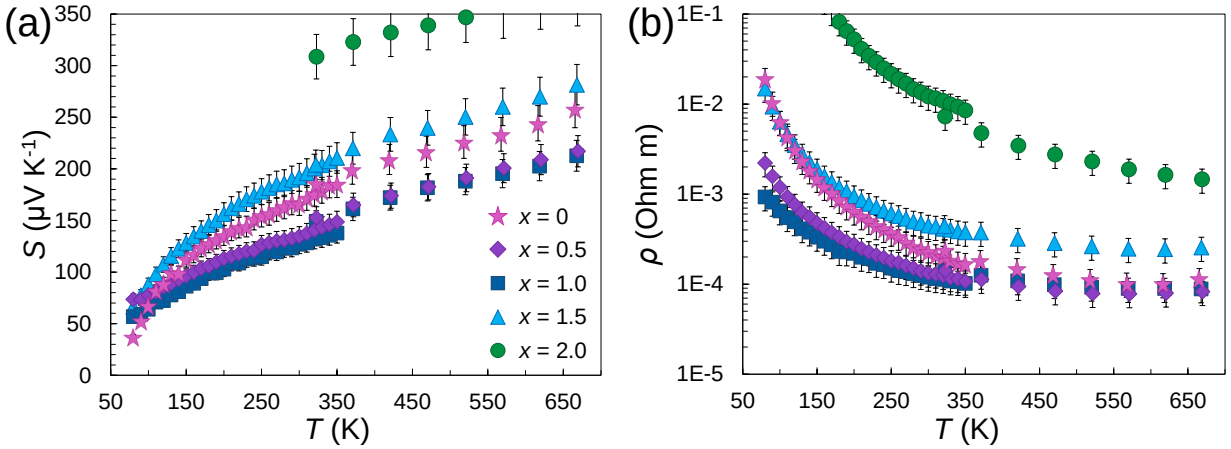

Figure 6.5: Electrical transport data of $Cu_{10}Ni_{2-x}Zn_xSb_4S_{13}$ ($x = 0$, 0.5, 1.0, 1.5, and 2.0) synthesized by reactive spark plasma sintering, where data for thermopower (S) and electrical resistivity (ρ) are shown in (a) and (b), respectively. Low-temperature thermopower for the $x = 2$ sample has been excluded for visual clarity, since the signal is erratic and noisy.

In alignment with thermopower results, the electrical resistivity data (Figure 6.5b) generally demonstrate increasing resistivity with increasing Zn content. At low temperatures, the electrical resistivity data have the shape of a classical semiconductor, before adopting more metallic characteristics at higher temperatures. As expected, the highest electrical resistivity is exhibited by $Cu_{10}Zn_2Sb_4S_{13}$. In turn, the $x = 2$ composition would not make an effective TE material because of its abysmally low power factor. The $x = 1.5$ sample also demonstrates a high resistivity, representing a systematic shift to insulating behavior

with the addition of Zn dopant. At high temperatures, our resistivity values (10^{-4} Ωm) are on a similar order of magnitude as those reported by Lu et al. (5×10^{-5} Ωm) for similar compositions.[66]

Some of the reactive SPS and mechanical alloying (Chapter 5) tetrahedrites ($x = 0$ and 0.5) demonstrate extremely similar electrical properties between the two syntheses. Contrastingly, $Cu_{10}NiZnSb_4S_{13}$ and $Cu_{10}Ni_{0.5}Zn_{1.5}Sb_4S_{13}$ do not agree between the two methods. Discrepancies between the different approaches for samples of the same target stoichiometry are attributable to variations in chemical composition and the presence of secondary phases. Impurities contribute to charge carrier scattering, and it is also possible that particle size is affecting the material properties as well. Differences in particle size are expected for samples prepared by procedures involving milling times of 1 h (reactive SPS) versus 48 h (mechanical alloying).

Thermal transport data for $Cu_{10}Ni_{2-x}Zn_xSb_4S_{13}$ ($0 \leq x \leq 2$) fabricated by reactive SPS are displayed in Figure 6.6. Low-temperature data require a stronger radiation correction to match data in the overlapping temperature region, and little insight is to be gained from cryostat thermal conductivity data. Nevertheless, in the high-temperature regime, exceptionally low thermal conductivity data ($\kappa_{total} < 0.7$ $Wm^{-1}K^{-1}$) are obtained for all samples. After removing the electronic component, lattice thermal conductivities (Figure 6.6b) converge to similar values, indicating little difference in the lattice contribution for these compositionally similar materials. Lattice thermal conductivities demonstrate a decreasing linear temperature dependence, consistent with enhanced phonon-phonon scattering at higher temperatures. All samples made by reactive SPS demonstrate higher lattice thermal conductivities than those of mechanically alloyed samples. Again, this is likely due to differences in chemical composition, particle size, and phase homogeneity.

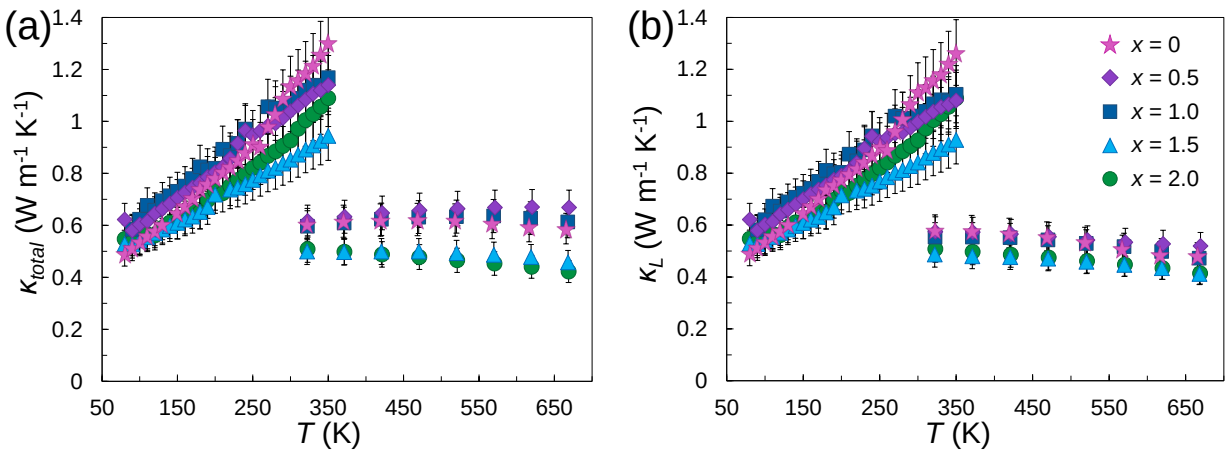

Figure 6.6: Thermal transport data of $Cu_{10}Ni_{2-x}Zn_xSb_4S_{13}$ (x = 0, 0.5, 1.0, 1.5, and 2.0) synthesized by reactive spark plasma sintering, where data for total thermal conductivity (κ_{total}) and lattice thermal conductivity (κ_L) are shown in (a) and (b), respectively.

Figure of merit (ZT) data for co-doped tetrahedrites synthesized by reactive SPS are shown in Figure 6.7. A systematic trend of decreasing ZT with increasing Zn content is observed. This is mostly a manifestation of the poor electrical properties of Zn-doped tetrahedrites. The highest ZT obtained was for $Cu_{10}Ni_2Sb_4S_{13}$, reaching a value of 0.66 at 673 K. Overall, these data are on par with those obtained previously for similar tetrahedrites made by traditional solid-state methods.[55,89] Comparing to Guler et al., who used open die pressing to prepare Ni and Zn co-doped tetrahedrites, our results are in very good agreement with their findings for $Cu_{11}NiSb_4S_{13}$ (ZT = 0.65 at 673 K). Therefore, reactive spark plasma sintering is shown to be a viable synthetic method for producing high-performance tetrahedrite TEs.

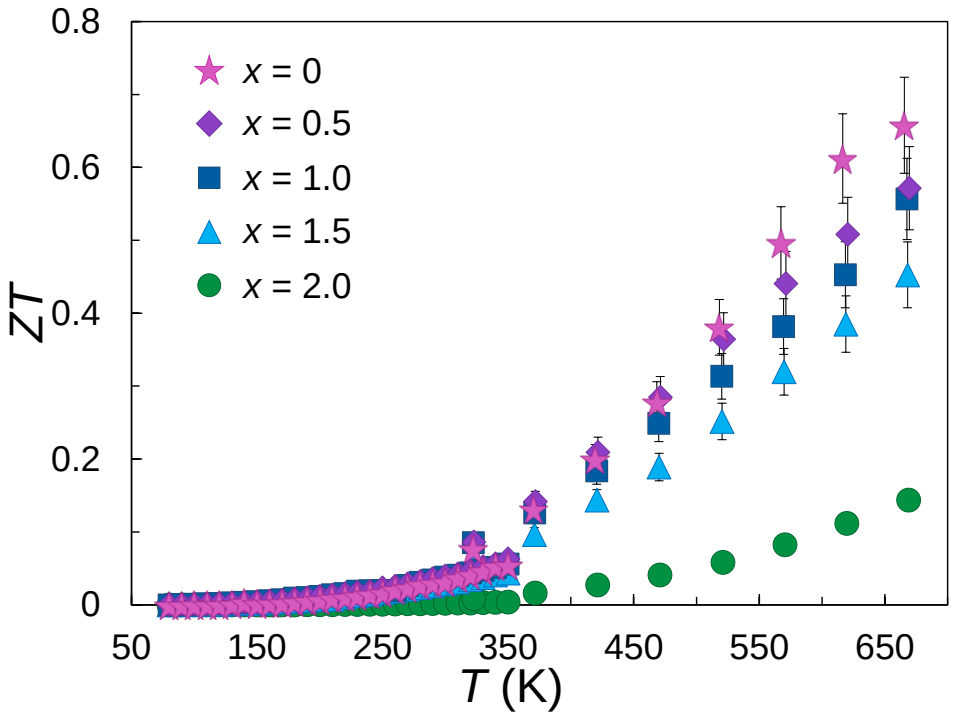

Figure 6.7: Figure of merit (ZT) data of $Cu_{10}Ni_{2-x}Zn_xSb_4S_{13}$ (x = 0, 0.5, 1.0, 1.5, and 2.0) synthesized by reactive spark plasma sintering.

Chapter 7

Conclusions and Future Work

In this dissertation, the author has provided background on inadequacies in energy technology and infrastructure that result in a majority loss of the planet's total energy consumed. A short-term solution to improving global energy efficiency is thermoelectric (TE) technology that generates power through waste heat recovery. TE materials demonstrate fascinating physical properties that enable the flow of electricity with some input of heat. Over the years, TE materials have been researched quite heavily, with many state-of-the-art TEs containing toxic or low-abundance elements. Within the last decade, tetrahedrite materials have received increased attention due to their environmental friendliness, availability, cost-effectiveness, and relatively good TE performance. However, the traditional methods used to produce tetrahedrites are lengthy, involved, and highly energetic.

The experimental approaches investigated in this report provide faster and easier ways of synthesizing a broader range of tetrahedrites than conventional solid-state methods. The modified polyol process synthesizes Cu-based, Zn-doped, and Fe-substituted tetrahedrites structured on the nanoscale. Tetrahedrites doped with Fe, Ni, and Zn may be produced by the rapid, scalable, and highly reproducible mechanical alloying procedure. And reactive spark plasma sintering (SPS) was used to obtain high-performance tetrahedrite TE materials in less than 2 h of total synthesis time. All of these novel methods require less time and less energy than the traditional melt-recrystallization approach, which requires reaction

temperatures up to 650 °C and 2 to 3 weeks of total synthesis time. Accordingly, these new approaches will enable more practical research and effective commercialization of tetrahedrite TE materials.

7.1 Future Work

One of the most important research questions to be addressed is if it is possible to obtain tetrahedrites that conduct with n-type behavior in their operational temperature range (500–700 K). While tetrahedrite has been commercially applied in TE generators as the p-type leg in devices, alternative materials must be used for the n-type leg. The recent generator manufactured by Alphabet Energy, Inc. utilized magnesium silicide stannide as the n-type leg.[191] However, high-performance n-type tetrahedrite would be a desirable alternative for improved manufacturability, enhanced mechanical stability, and reduced thermal expansion mismatch. In this document, n-type conductivity has been demonstrated at low temperatures in Fe-doped tetrahedrites, which is consistent with previous reports from Lu.[192] Alas, this phenomenon remains enigmatic. And it seems possible that with some tactful engineering, one could extend the range over which tetrahedrites demonstrate n-type behavior.

The following subsections will detail some recommendations for future work regarding tetrahedrite materials. First, some suggestions for promising dopants and compositions will be provided. After that, impediments to the practical implementation of tetrahedrites in commercial applications will be addressed. Some of these setbacks include issues with ionic mobility, thermal stability, and mechanical properties.

7.1.1 Unexplored Dopants and Off-stoichiometry Compositions

Despite multitudinous doping studies involving tetrahedrite TEs, there are still numerous dopants that could be explored further. Figure 7.1 illustrates some of the elements which have been studied in tetrahedrite TEs, as well as recommendations for potential candidate substituents to be researched next. Transition metals in the same row as Cu have been explored rampantly as dopants on the metal site, as well as Te on the Sb site. There are very few TE studies involving tetrahedrites substituted on the metal site with Cd, Ge, Sn, or Pb. Similarly, limited research has focused on substituting As or Bi on the Sb site. Unfortunately, while some of these substituents have been shown to provide modest enhancements to ZT, the toxicity of Cd, Pb, and As are disadvantageous for widespread commercial applications. Quite recently, several studies have examined Se substitution [126, 127], Cu-enrichment [100, 166], and S deficiency [94]. With this high degree of chemical variability, a whole new range of multiply doped compounds is producible.

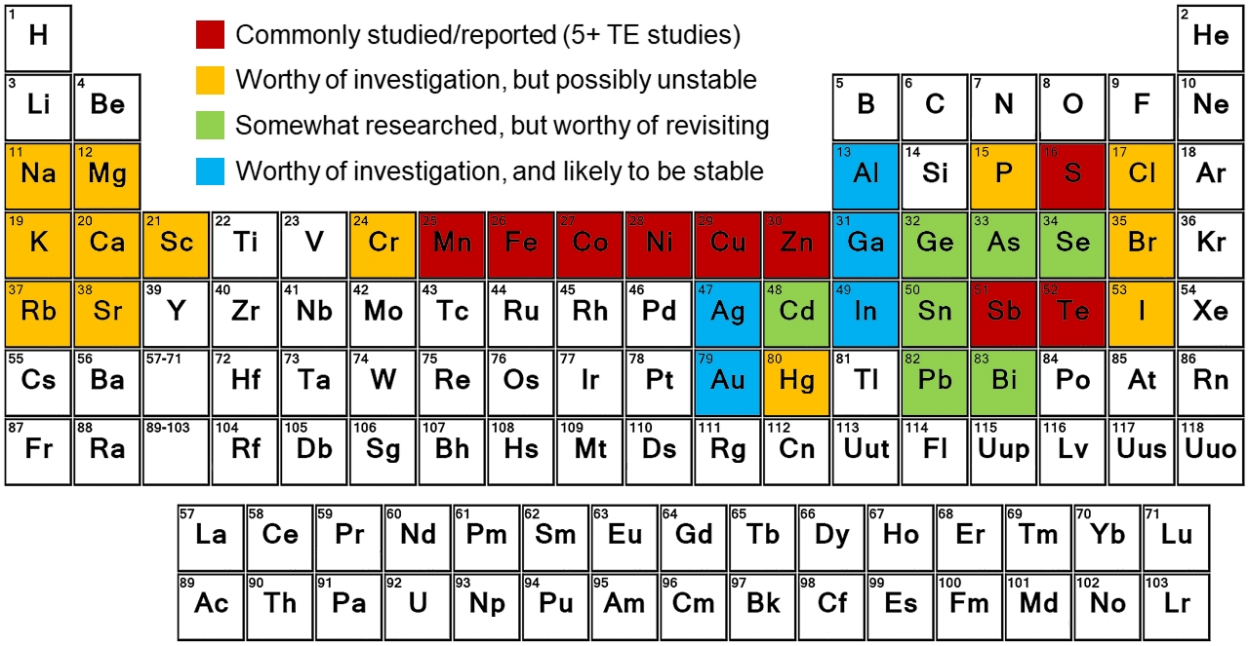

Figure 7.1: Periodic table with elements highlighted that have been studied or would be of interest for future studies regarding the thermoelectric (TE) properties of tetrahedrites.

Given the nascency of tetrahedrite research, the community is seeing rapid development and optimization of novel synthetic approaches for fabricating tetrahedrite TEs. With these developments, it may be possible to incorporate different elements into the crystal structure. The coinage metals below Cu, such as Ag [117] or Au [104], have been shown to be stable in tetrahedrites, and the large mass difference from these atoms is hypothesized to reduce thermal conductivity. However, the cost of these elements is an obstacle for large-scale production. In another case, the group 3B elements (e.g., Al, Ga, and In) seem to be ideal candidates for replacing Cu in the tetrahedrite structure, owing to their similar ionic size and bonding tendencies. One recent study investigated the influence of InSb inclusions in tetrahedrite materials, and their composite material of $Cu_{12}Sb_4S_{12}$ with 3% InSb exhibited massive improvements by achieving ZT of 0.9 at 723 K.[193] Nonetheless, no studies have come out yet for In-doped tetrahedrites, which hold promise for demonstrating n-type conductivity over a large temperature range. The group 3B elements are expected to take a trivalent oxidation state, and in turn, one could potentially achieve n-type behavior by doping with this approach.

In brief, one could speculate that more exotic dopants are possible in tetrahedrites as well. Doping with alkali metals, alkali earth metals, Sc, Cr, or Hg may be achievable on the Cu site. Similarly, the S site could potentially be doped with P or halogens like Cl, Br, or I. Whether or not these substitutions improve TE performance, or are even stable in the tetrahedrite structure, they could provide a wealth of information regarding the various complexities of phase evolution and phonon scattering in tetrahedrites. Interestingly, a silver-phosphide tetrahedrite compound ($Ag_6Ge_{10}P_{12}$) has been shown to exhibit the same bonding and uniquely low thermal conductivity as its Cu-based counterpart.[194] While the speed and quality at which tetrahedrite TEs may be produced are improving, there is still a

large selection of unexplored compounds that should be investigated.

Overall, the synthetic capabilities of the modified polyol process are quite broad, being that this electrochemical reaction relies on the reduction potential of the elements involved. This means that, if a metal ion is easily reduced, it is a good candidate for tetrahedrite synthesis via the modified polyol approach. As a reminder, the modified polyol approach uses a strong reducing agent, sodium borohydride ($NaBH_4$), to reduce metal ions (e.g., Cu^{2+}) to their elemental form so they can undergo a bottom-up reaction on the atomic scale. Conversely, the traditional solid-state melting synthesis is convoluted by the entanglement of thermodynamics and kinetics, which naturally encourage the formation of impurities like copper sulfides ($Cu_{2-x}S$) and famatinite (Cu_3SbS_4). Therefore, the modified polyol synthesis may be employed to synthesize a greater compositional range of tetrahedrites than is attainable by traditional solid-state methods.

7.1.2 Cu Electromigration and Superionic Conductivity

Another important problem regarding the use of tetrahedrite for TE applications involves the issue of copper ion migration. Although many Cu chalcogenides demonstrate excellent TE characteristics, high ionic mobility in these materials leads to irreversible sample degradation over their lifetime.[195–199] As an electric current density is applied, electrically charged ions migrate through the lattice and collect on one side of the material. Over time, the compositional variation begins to detrimentally affect TE performance. This problem is a major obstruction for the practical use of tetrahedrite TEs. The best way to study these effects is by ionic conductivity measurements via impedance spectroscopy, which can determine the mobility of various ions in a material. Therefore, Cu ion diffusion is a significant problem that is holding back Cu semiconducting compounds from being used on a commercial scale.

It is hypothesized that high ionic mobility in tetrahedrite results from Cu atoms partially vacating tetrahedral 12d sites and residing on interstitial sites within the lattice. This connected pathway of vacancies and interstitial sites provides a network for Cu ions to migrate through the lattice.[52, 98] In such situations, mobile Cu ions can constitute 7–28% of the total Cu content depending on the level of Cu-enrichment.[99] In $Cu_{14}Sb_4S_{13}$, up to 4 high-mobility Cu ions may reside on interstitial sites, accompanied by a partial vacating of Cu12d sites.[200] In general, the Cu diffusivity is affected by ionic charge and size. However, the ratio of Cu^{2+} to Cu^{1+} is dependent on chemical composition, and Cu-rich tetrahedrites contain a greater portion of monovalent Cu ions than their Cu-poor counterparts.[65] The network of interstitial sites and vacant tetrahedral sites is believed to be the source for Cu ion mobility in tetrahedrite materials. Overall, high ionic conductivity is the physical origin of the exsolution process in which tetrahedrites phase separate into Cu-rich and Cu-poor tetrahedrite phases, and this phenomenon is not well-understood by the community.

Doping tetrahedrites with transition metals may influence the ionic conductivity of these materials. In doped tetrahedrites, normal semiconducting behavior is observed with virtually non-existent ionic conductivity.[129] This outcome is likely associated with an incorporation of dopants (i.e., Zn and Fe), which exclusively substitute on the tetrahedral site, thus blocking the Cu migration path and stabilizing the tetrahedrite crystal structure.[96, 115] It seems as if these dopants are acting as a plug to stop the flow of liquid-like Cu ions through the tetrahedrite lattice. Accordingly, a study of the relationship between ionic conductivity and chemical composition would be beneficial to shed light on ways of improving the lifetime of tetrahedrite TEs. In general, neutron scattering and impedance spectroscopy are two techniques that may be used to better understand ionic conductivity in doped and undoped tetrahedrite materials.

7.1.3 Thermal Stability and Mechanical Stability

The thermal stability of tetrahedrites remains a relatively unexplored concept, which is surprising given these materials great amount of attention as a prospective TEs. Most ZT data presented for tetrahedrites do not exhibit a peak over the operational temperature range (500–700 K). Instead, ZT is constantly increasing up to the maximum measurement temperature. In practice, the research community understands that some sort of degradation occurs above 700 K, which is noticeable with a drop in thermal conductivity and changes to chemical composition. Nevertheless, the precise dynamics of the thermal break-down of tetrahedrites have yet to be investigated thoroughly. In general, differential scanning calorimetry, thermogravimetric analysis (TGA), temperature-dependent X-ray diffraction (XRD), and neutron diffraction would be useful for better understanding the thermal stability of doped and undoped tetrahedrites.

Several studies have examined thermal stability of tetrahedrites. Barbier et al. used temperature-dependent XRD and TGA to map the phase decomposition of tetrahedrite into chacostibite ($CuSbS_2$) and skinnerite (Cu_3SbS_3), and it was found that Ni-substituted tetrahedrites were stable up to a much higher temperature than the undoped composition.[114] Not long after, many of the same researchers closely examined the decomposition of $Cu_{12}Sb_4S_{13}$ with temperature-dependent neutron diffraction, finding that the undoped compound decomposes in the temperature range of 792 to 836 K.[201] Very recently, Goncalves et al. investigated oxidation and phase evolution as a function of temperature, finding that slow oxidation occurs in tetrahedrites at temperatures as low as 230 °C.[202] Accordingly, a handful of studies have investigated the stability of tetrahedrites at various temperatures, but more exploration is necessary given the large compositional range of these compounds.

Briefly, the mechanical properties of tetrahedrite materials could be explored further. This is important work because the materials will never be amenable to commercial applications if they are mechanically compromised. From personal experience and discussing with researchers around the world, most researchers would agree that tetrahedrites are quite brittle and difficult to handle. In this way, tetrahedrites demonstrate the mechanical characteristics of a ceramic material, which likely arise from the mixture a ionic and covalent bonding.[54] Through process optimization (e.g., reaction temperature, time, pressure) or modifications to the chemical composition, these mechanical issues could be mitigated. Mechanical property measurements, such as resonance ultrasound spectroscopy, would be particularly useful for understanding the dynamics between lattice strain, elasticity, and phonon propagation.

It is worth noting that some studies have involved characterizing the mechanical properties of tetrahedrites. For example, Fan et al. measured hardness, Young's modulus, shear modulus, Poisson's ratio, and bulk modulus in synthetic and natural mineral tetrahedrites.[134] Additionally, Sun et al. investigated brittleness, thermal stability, and microstructure in tetrahedrites.[93] Ultimately, their results indicated that mechanical properties can be improved with additional spark plasma sintering processing, beyond what conventional syntheses require. All in all, mechanical issues impede the application of tetrahedrite materials on a widespread scale, and there is still room for fruitful research involving mechanical characterization of doped and undoped tetrahedrites.

7.2 Closing Remarks

The synthetic techniques described in this report provide a means for studying tetrahedrite thermoelectrics with greater speed and versatility. Additionally, these processes are more

facile, cost-effective, and scalable than the traditional melt-recrystallization synthesis. The modified polyol process is useful for synthesizing a great range of tetrahedrite compounds with nanoscale structuring. Mechanical alloying is a rapid, reproducible, and highly scalable approach for producing high-performance tetrahedrite TEs. And the reactive spark plasma sintering approach requires the least amount of time (1 h ball milling and 30 min sintering) to produce a sample that can undergo full TE characterization. These novel synthetic approaches enable the exploration of new dopants, ionic mobility, and stability properties of tetrahedrite TE materials.

APPENDIX

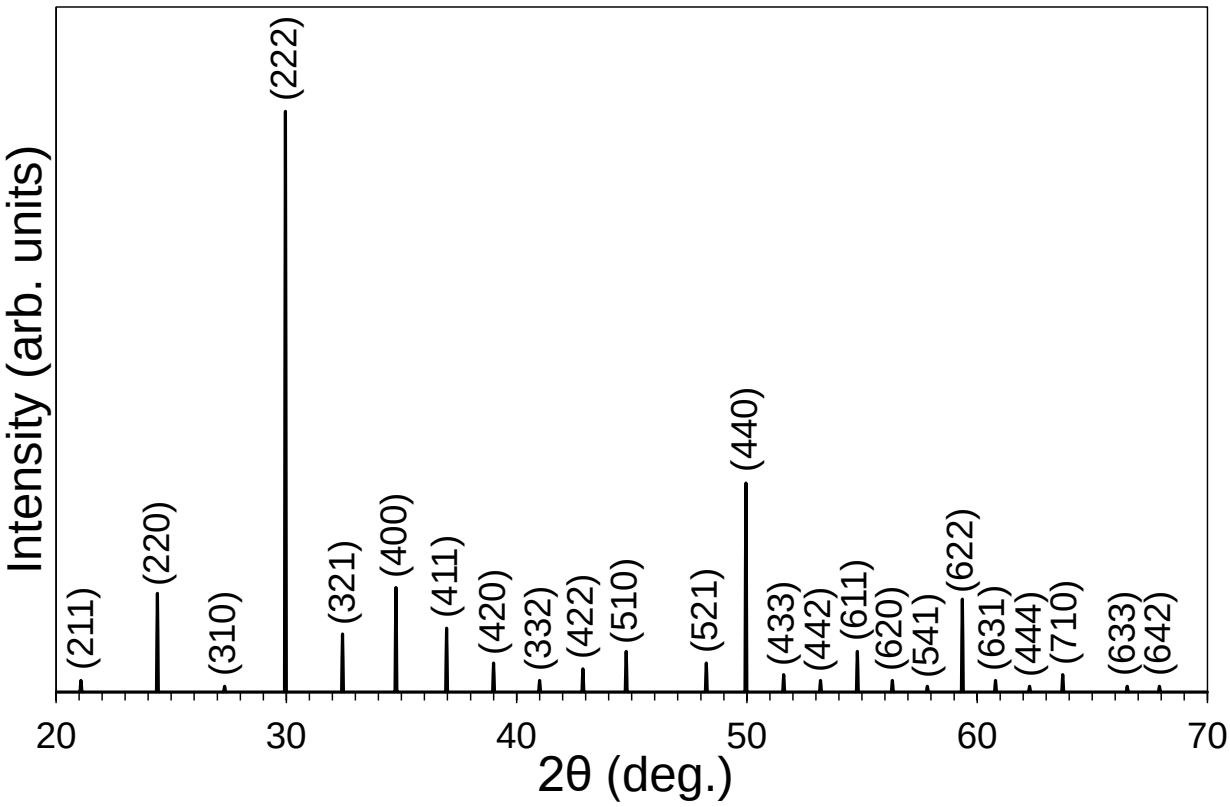

Figure A1: X-ray diffraction profile of Cu-based tetrahedrite, $Cu_{12}Sb_4S_{13}$, from Wuensch.[51]

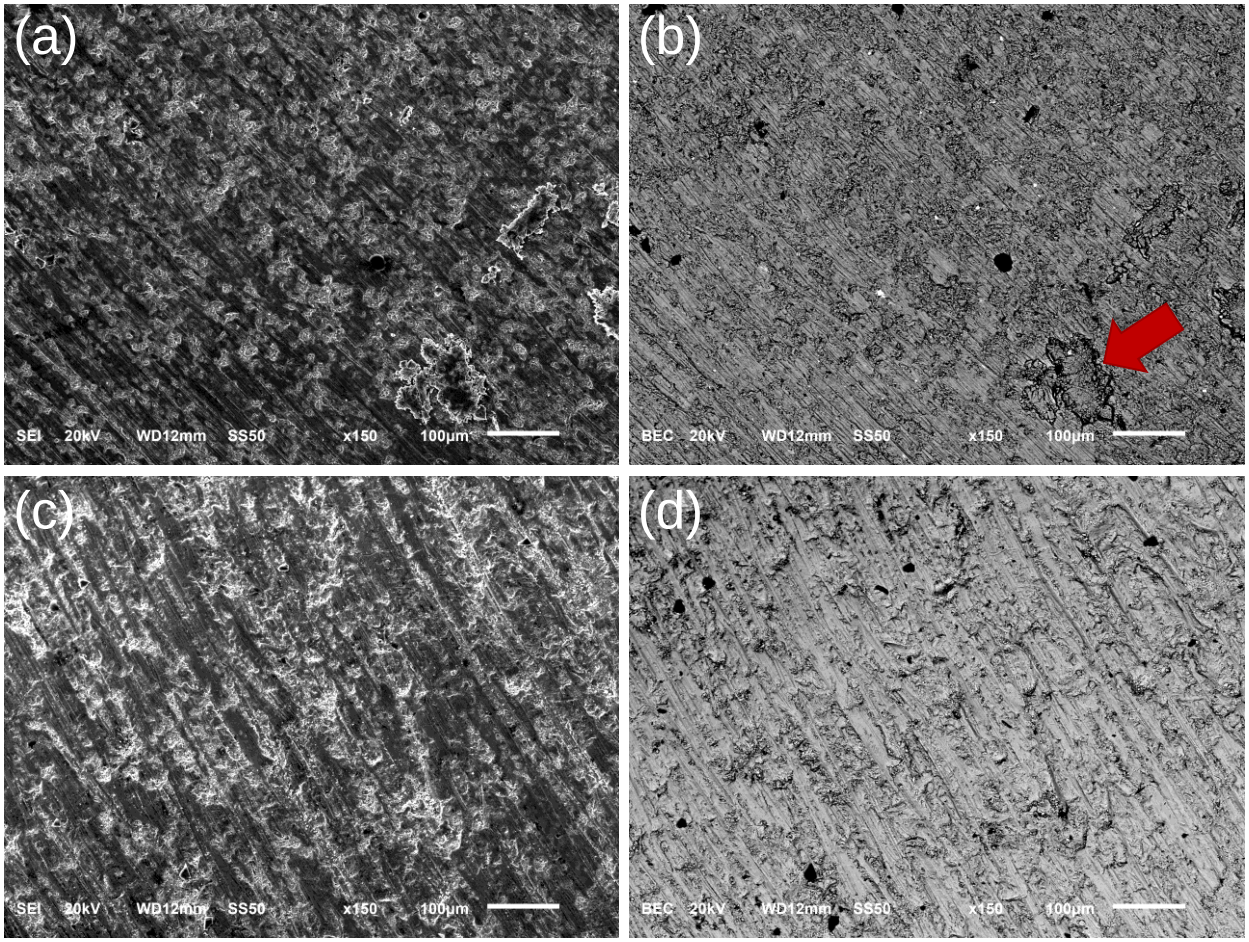

Figure A2: Electron microscopy images of pellet surfaces of (a,b) $Cu_{12}Sb_4S_{13}$ and (c,d) $Cu_{11}ZnSb_4S_{13}$ synthesized by modified polyol process; images were collected via (a,c) secondary electrons and (b,d) backscatter electrons. Miniscule signatures of organic debris (opaque black) and SiC polishing media (pure white) are present in the backscatter images. $Cu_{12}Sb_4S_{13}$ shows a darkened region in the backscatter image (marked by a red arrow) with a slight off-stoichiometry from the majority phase. It is speculated that this is the less prominent Cu-rich tetrahedrite phase of the post-processed Cu-based sample, which is non-existent in the backscatter image of the Zn-doped sample.

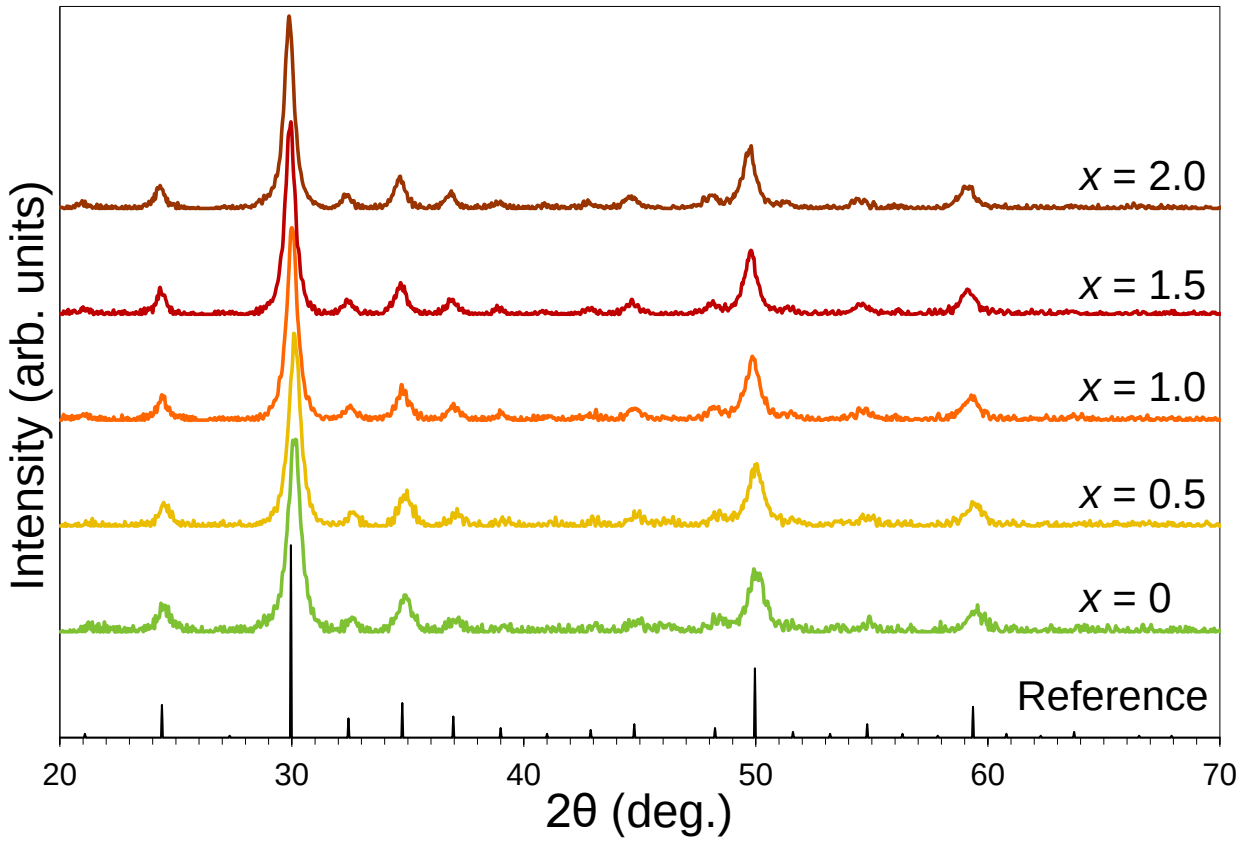

Figure A3: X-ray diffraction profiles of $Cu_{10}Ni_{2-x}Zn_xSb_4S_{13}$ ($x = 0, 0.5, 1.0, 1.5, 2.0$) after 48 h of planetary ball milling (for mechanical alloying synthesis).

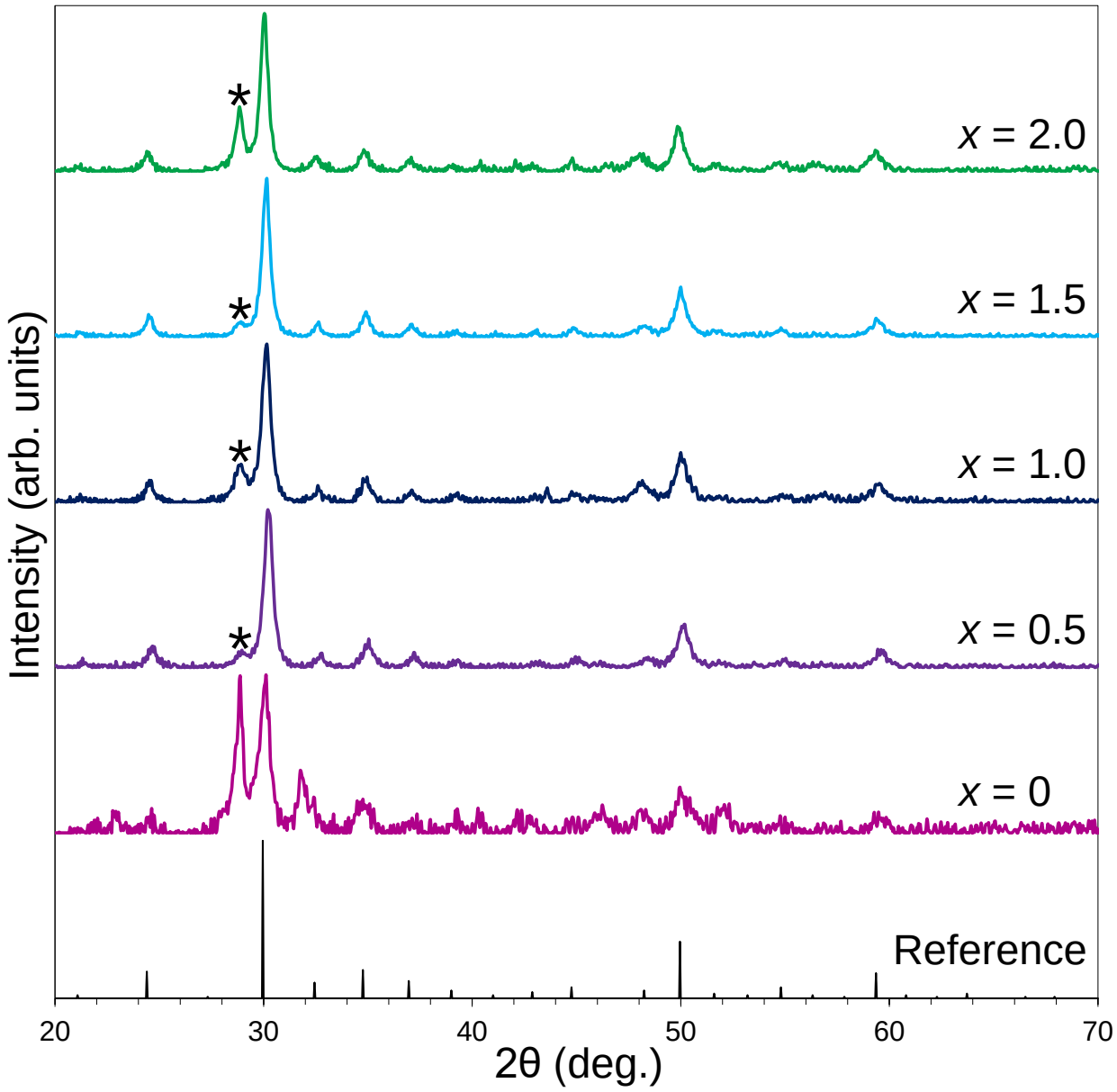

Figure A4: X-ray diffraction profiles of $Cu_{10}Ni_{2-x}Zn_xSb_4S_{13}$ ($x = 0, 0.5, 1.0, 1.5, 2.0$) after 1 h of vibratory ball milling (for reactive spark plasma sintering (SPS) synthesis). Primary peaks of Cu_3SbS_4 impurities are marked by $*$ symbols.

REFERENCES

REFERENCES

[1] J.M. Cullen, J.M. Allwood, and E.H. Borgstein. Reducing energy demand: What are the practical limits? *Environmental Science and Technology*, 45(4):1711–1718, 2011.

[2] S. Solomon, G.K. Plattner, R. Knutti, and P. Friedlingstein. Irreversible climate change due to carbon dioxide emissions. *Proceedings of the National Academy of Sciences*, 106(6):1704–1709, 2009.

[3] D.V. Schroeder. *An Introduction to Thermal Physics*. Addison Wesley Longman, first edition, 2000.

[4] C. Forman, I.K. Muritala, R. Pardemann, and B. Meyer. Estimating the global waste heat potential. *Renewable and Sustainable Energy Reviews*, 57:1568–1579, 2016.

[5] J.M. Cullen and J.M. Allwood. Theoretical efficiency limits for energy conversion devices. *Energy*, 35(5):2059–2069, 2010.

[6] J.M. Cullen and J.M. Allwood. The efficient use of energy: Tracing the global flow of energy from fuel to service. *Energy Policy*, 38(1):75–81, 2010.

[7] U.S. Energy Information Administration. International Energy Statistics, 2017.

[8] The World Bank. Total Population Statistics, 2017.

[9] Lawrence Livermore National Laboratory. U.S. Estimated Energy Use in 2016, 2017.

[10] C. Wu. Analysis of waste-heat thermoelectric power generators. *Appl.Thermal Eng.*, 16(1):63–69, 1996.

[11] S.B. Riffat and X. Ma. Thermoelectrics: A review of present and potential applications. *Appl. Thermal Eng.*, 23(8):913–935, 2003.

[12] K. Ikoma, M. Munekiyo, K. Furuya, M. Kobayashi, T. Izumi, and K. Shinohara. Thermoelectric module and generator for gasoline engine vehicles. *17th Int. Conf. Thermoelectrics*, pages 464–467, 1998.

[13] C.T. Hsu, G.Y. Huang, H.S. Chu, B. Yu, and D.J. Yao. Experiments and simulations on low-temperature waste heat harvesting system by thermoelectric power generators. *Appl. Energy*, 88(4):1291–1297, 2011.

[14] X. Gou, H. Xiao, and S. Yang. Modeling, experimental study and optimization on low-temperature waste heat thermoelectric generator system. *Appl. Energy*, 87(10):3131–3136, 2010.

[15] K. Zeb, S. M. Ali, B. Khan, C.A. Mehmood, N. Tareen, W. Din, U. Farid, and A. Haider. A survey on waste heat recovery: Electric power generation and potential prospects within Pakistan. *Renewable and Sustainable Energy Rev.*, 75(November):1142–1155, 2017.

[16] G.M. Fradkin and V.M. Kodyukov. Radioisotope Thermoelectric Generators. *Atomnaya Energiya*, 26(2):169–175, 1969.

[17] A. Patyk. Thermoelectrics: Impacts on the environment and sustainability. *J. Elec. Mater.*, 39(9):2023–2028, 2010.

[18] S.O. Kasap. *Principles of Electronic Materials and Devices*. McGraw-Hill, New York, NY, 3rd edition, 2006.

[19] R.R. Heikes and R.W. Ure. *Thermoelectricity: Science and Engineering*. Interscience, 1961.

[20] H.J. Goldsmid. *Applications of Thermoelectricity*. John Wiley & Sons, New York, NY, 1960.

[21] I.B. Cadoff and E. Miller. *Thermoelectric Materials and Devices*. Reinhold Publishing Company, New York, NY, 1960.

[22] T.J. Seebeck. Uber den Magnetismus der galvanischen Kette. *Abh. Akad. Wiss. Berlin*, pages 289–346, 1822.

[23] T.J. Seebeck. Ueber die magnetische Polarisation der Metalle und Erze durch Temperatur-Differenz. *Ann. Phys.*, 82(3):133–160, 1826.

[24] J.C. Peltier. Nouvelles experiences sur la caloricite des courants electriques. *Ann. Chim. Phys.*, 56:371–386, 1834.

[25] H.J. Goldsmid. Principles of thermoelectric devices. *Brit. J. Appl. Phys.*, 11(6):209–217, 1960.

[26] G.J. Snyder and E.S. Toberer. Complex thermoelectric materials. *Nature Mater.*, 7(2):105–114, 2008.

[27] G. Benenti, H. Ouerdane, and C. Goupil. The thermoelectric working fluid: thermodynamics and transport. *Comptes Rendus Physique*, 17(10):1072–1083, 2016.

[28] L. Chen, F. Sun, and C. Wu. Effect of heat transfer law on the performance of a generalized irreversible Carnot engine. *J. Phys. D: Appl. Phys.*, 32(2):99–105, 1999.

[29] T.M. Tritt. Thermoelectric Phenomena, Materials, and Applications. *Annual Rev. Mater. Res.*, 41:433–448, 2011.

[30] D.T. Morelli. Potential Applications of Advanced Thermoelectrics in the Automobile Industry. In *15th Int. Conf. Thermoelectrics*, pages 383–386, 1996.

[31] L.D. Zhao, S.H. Lo, Y. Zhang, H. Sun, G. Tan, C. Uher, C. Wolverton, V.P. Dravid, and M.G. Kanatzidis. Ultralow thermal conductivity and high thermoelectric figure of merit in SnSe crystals. *Nature*, 508(7496):373–7, 2014.

[32] X. Zhang and L.D. Zhao. Thermoelectric materials: Energy conversion between heat and electricity. *J. Materiomics*, 1:92–105, 2015.

[33] G.A. Slack and D.M. Rowe. New Materials and Performance Limits for Thermoelectric Cooling CRC Handbook of Thermoelectrics. In D.M Rowe, editor, *CRC Handbook of Thermoelectrics*, chapter 34. CRC Press, 1995.

[34] D.G. Cahill and R.O. Pohl. Lattice Vibrations and Heat Transport in Crystals and Glasses. *Annual Review of Physical Chemistry*, 39(1):93–121, 1988.

[35] M. Beekman, D.T. Morelli, and G.S. Nolas. Better thermoelectrics through glass-like crystals. *Nature Mater.*, 14(12):1182–1185, 2015.

[36] E. Lara-Curzio, A. F. May, O. Delaire, M. A. Mcguire, X. Lu, C. Liu, E. D. Case, and D. T. Morelli. Low-temperature heat capacity and localized vibrational modes in natural and synthetic tetrahedrites. *J. Appl. Phys.*, 115, 2014.

[37] J.Q. Guo, H.Y. Geng, T. Ochi, S. Suzuki, M. Kikuchi, Y. Yamaguchi, and S. Ito. Development of skutterudite thermoelectric materials and modules. *J. Elec. Mater.*, 41(6):1036–1042, 2012.

[38] T. Takabatake, K. Suekuni, T. Nakayama, and E. Kaneshita. Phonon-glass electron-crystal thermoelectric clathrates: Experiments and theory. *Rev. Modern Physics*, 86(2):669–716, 2014.

[39] M.G. Kanatzidis. Nanostructured thermoelectrics: The new paradigm? *Chem. Mater.*, 22(3):648–659, 2010.

[40] J.P. Heremans, M.S. Dresselhaus, L.E. Bell, and D.T. Morelli. When thermoelectrics reached the nanoscale. *Nature Nanotech.*, 8:471–473, 2013.

[41] K. Biswas, J. He, I.D. Blum, C.I. Wu, T.P. Hogan, D.N. Seidman, V.P. Dravid, and M.G. Kanatzidis. High-performance bulk thermoelectrics with all-scale hierarchical architectures. *Nature*, 489:414–418, 2012.

[42] S. LeBlanc. Thermoelectric generators: Linking material properties and systems engineering for waste heat recovery applications. *Sustainable Mater. Tech.*, 1:26–35, 2014.

[43] R. Amatya and R. J. Ram. Trend for thermoelectric materials and their earth abundance. *J. Elec. Mater.*, 41(6):1011–1019, 2012.

[44] J.W. Anthony, R.A. Bideaux, K.W. Bladh, and M.C. Nichols. *Handbook of Mineralogy*. Mineralogical Society of America, Chantilly, VA, 2003.

[45] J. Majzlan, S. Kiefer, J. Herrmann, M. Stevko, J. Sejkora, M. Chovan, T. Lanczos, M. Lazarov, A. Gerdes, F. Langenhorst, A.B. Radkova, H. Jamieson, and R. Milovsky. Synergies in elemental mobility during weathering of tetrahedrite [(Cu,Fe,Zn)12(Sb,As)4S13]: Field observations, electron microscopy, isotopes of Cu, C, O, radiometric dating, and water geochemistry. *Chem. Geol.*, 488:1–20, 2018.

[46] C. Falagan, B.M. Grail, and D.B. Johnson. New approaches for extracting and recovering metals from mine tailings. *Miner. Eng.*, 106:71–78, 2017.

[47] K. Suekuni and T. Takabatake. Research Update: Cu-S based synthetic minerals as efficient thermoelectric materials at medium temperatures. *APL Mater.*, 4(10):104503, 2016.

[48] C. Candolfi, Y. Bouyrie, S. Sassi, A. Dauscher, and B. Lenoir. Tetrahedrites: Prospective Novel Thermoelectric Materials. In *Thermoelectrics for Power Generation - A Look at Trends in the Technology*, chapter Ch. 4, pages 71–90. InTechOpen, 2016.

[49] D.T. Morelli. Thermoelectric Materials. In *Springer Handbook of Electronic and Photonic Materials*, chapter 57, pages 1379–1390. Springer International Publishing, 2017.

[50] R. Chetty, A. Bali, and R.C. Mallik. Tetrahedrites as thermoelectric materials: an overview. *J. Mater. Chem. C*, 3(48):12364–12378, 2015.

[51] B.J. Wuensch. The crystal structure of tetrahedrite, Cu12Sb4S13. *Zeitschrift fur Kristallographie - New Crystal Structures*, 119(5-6):437–453, 1964.

[52] A. Pfitzner, M. Evain, and V. Petricek. Cu12Sb4S13: A Temperature-Dependent Structure Investigation. *Acta Crystallographica Section B Structural Scii.*, 53:337–345, 1997.

[53] R.C. Peterson and I. Miller. Crystal Structure and Cation Distribution in Freibergite and Tetrahedrite. *Mineralogy Magazine*, 50(358):717–721, 1986.

[54] W. Lai, Y. Wang, D.T. Morelli, and X. Lu. From bonding asymmetry to anharmonic rattling in Cu12Sb4S13 tetrahedrites: When lone-pair electrons are not so lonely. *Adv. Functional Mater.*, 25(24):3648–3657, 2015.

[55] K. Suekuni, K. Tsuruta, T. Ariga, and M. Koyano. Thermoelectric properties of mineral tetrahedrites Cu10Tr2Sb4S13 with low thermal conductivity. *Appli. Phys. Express*, 5(5):051201, 2012.

[56] F.D. Benedetto, G. P. Bernardini, C. Cipriani, C. Emiliani, D. Gatteschi, and M. Romanelli. The distribution of Cu(II) and the magnetic properties of the synthetic analogue of tetrahedrite: Cu12Sb4S13. *Phys. Chem. Miner.*, 32(3):155–164, 2005.

[57] D.I. Nasonova, V.Y. Verchenko, A.A. Tsirlin, and A.V. Shevelkov. Low-temperature structure and thermoelectric properties of pristine synthetic tetrahedrite Cu12Sb4S13. *Chem. Mater.*, 28(18):6621–6627, 2016.

[58] T. Suzuki, H. Goto, I. Ishii, Y. Noguchi, S. Kamikawa, K. Suekuni, H.I. Tanaka, and T. Takabatake. Elastic Softening in the tetrahedrite Cu12Sb4S13. *Physics Procedia*, 75:443–446, 2015.

[59] S. Kitagawa, T. Sekiya, S. Araki, T.. Kobayashi, K. Ishida, T. Kambe, T. Kimura, N. Nishimoto, K. Kudo, and M. Nohara. Suppression of nonmagnetic insulating state by application of pressure in mineral tetrahedrite Cu12Sb4S13. *J. Phys. Soc. Japan*, 84(9):1–5, 2015.

[60] A.F. May, O. Delaire, J.L. Niedziela, E. Lara-Curzio, M.A. Susner, D.L. Abernathy, M. Kirkham, and M.A. McGuire. Structural phase transition and phonon instability in Cu12Sb4S13. *Phys. Rev. B*, 93(6):064104, 2016.

[61] H.I. Tanaka, K. Suekuni, K. Umeo, T. Nagasaki, H. Sato, G. Kutluk, E. Nishibori, H. Kasai, and T. Takabatake. Metal-Semiconductor Transition Concomitant with a Structural Transformation. *J. Phys. Soc. Japan*, 85, 2016.

[62] Y. Kosaka, K. Suekuni, K. Hashikuni, Y. Bouyrie, M. Ohta, and T. Takabatake. Effects of Ge and Sn substitution on the metal-semiconductor transition and thermoelectric properties of Cu12Sb4S13 tetrahedrite. *Phys. Chem. Chem. Phys.*, 19:8874–8879, 2017.

[63] M.L. Johnson and R. Jeanloz. A Brillouin-zone model for compositional variation in tetrahedrite. *Am. Miner.*, 68(1-2):220–226, 1983.

[64] R. Jeanloz and M.L. Johnson. A Note on the Bonding, Optical Spectrum and Composition of Tetrahedrite. *Phys. Chem. Miner.*, 11:52–54, 1984.

[65] R.A.D. Pattrick, G. VanDerLaan, D.J. Vaughan, and C.M.B. Henderson. Oxidation state and electronic configuration determination of copper in tetrahedrite group min-

erals by L-edge X-ray absorption spectroscopy. *Phys. Chem. Miner.*, 20(6):395–401, 1993.

[66] X. Lu, D.T. Morelli, Y. Xia, F. Zhou, V. Ozolins, H. Chi, X. Zhou, and C. Uher. High Performance Thermoelectricity in Earth-Abundant Compounds Based on Natural Mineral Tetrahedrites. *Adv. Energy Mater.*, 3(3):342–348, 2013.

[67] K. Suekuni, Y. Tomizawa, T. Ozaki, and M. Koyano. Systematic study of electronic and magnetic properties for Cu12-xTMxSb4S13 (TM = Mn, Fe, Co, Ni, and Zn) tetrahedrite. *J. Appl. Phys.*, 115(14):143702, 2014.

[68] Y. Bouyrie, C. Candolfi, V. Ohorodniichuk, B. Malaman, A. Dauscher, J. Tobola, and B. Lenoir. Crystal structure, electronic band structure and high-temperature thermoelectric properties of Te-substituted tetrahedrites Cu12Sb4-xTexS13 (0.5<x<2.0). *J. Mater. Chem. C*, 3(40):10476–10487, 2015.

[69] C. Tablero. Electronic and Optical Property Analysis of the Cu-Sb-S Tetrahedrites for High-Efficiency Absorption Devices. *J. Phys. Chem. C*, 118:15122–15127, 2014.

[70] S. Tippireddy, R. Chetty, M.H. Naik, M. Jain, K. Chattopadhyay, and R.C. Mallik. Electronic and Thermoelectric Properties of Transition Metal Substituted Tetrahedrites. *J. Phys. Chem. C*, 122:8735–8749, 2018.

[71] C. Uher, editor. *Material Aspects of Thermoelectricity*. CRC Press, 2017.

[72] K. Suekuni, K. Tsuruta, M. Kunii, H. Nishiate, E. Nishibori, S. Maki, M. Ohta, A. Yamamoto, and M. Koyano. High-performance thermoelectric mineral Cu12-xNixSb4S13 tetrahedrite. *J. Appl. Phys.*, 113, 2013.

[73] R. Chetty, P. Kumar, G. Rogl, P. Rogl, E. Bauer, M. Herwig, S. Suwas, S. Puchegger, G. Giester, and R.C. Mallik. Thermoelectric properties of a Mn substituted synthetic tetrahedrite. *Phys. Chem. Chem. Phys.*, 17:1716–1727, 2015.

[74] F. Zhou, W. Nielson, Y. Xia, and V. Ozolins. Lattice anharmonicity and thermal conductivity from compressive sensing of first-principles calculations. *Phys. Rev. Lett.*, 113(18), 2014.

[75] Y. Bouyrie, C. Candolfi, S. Pailhès, M.M. Koza, B. Malaman, A. Dauscher, J. Tobola, O. Boisron, L. Saviot, and B. Lenoir. From crystal to glass-like thermal conductivity in crystalline minerals. *Phys. Chem. Chem. Phys.*, 17(30):19751–19758, 2015.

[76] J. Li, M. Zhu, D.L. Abernathy, X. Ke, D.T. Morelli, and W. Lai. First-principles studies of atomic dynamics in tetrahedrite thermoelectrics. *APL Mater.*, 4(10), 2016.

[77] J. Li, D.P. Weller, D.T. Morelli, and W. Lai. Density-functional theory based molecular dynamics simulation of tetrahedrite thermoelectrics : Effect of cell size and basis sets. *Computational Mater. Sci.*, 144:315–321, 2018.

[78] T.P. Mishra, M. Koyano, and Y. Oshima. Detection of large thermal vibration for Cu atoms in tetrahedrite by high-angle annular dark-field imaging. *Appl. Phys. Express*, 10:045601, 2017.

[79] N. Ghassemi, X. Lu, Y. Tian, E. Conant, Y. Yan, X. Zhou, and J.H. Ross. Structure Change and Rattling Dynamics in Cu12Sb4S13 Tetrahedrite: an NMR Study. *ACS Appl. Mater. Inter.*, 10:36010–36017, 2018.

[80] K. Suekuni, C.H. Lee, H.I. Tanaka, E. Nishibori, A. Nakamura, M. Nakamura, S. Ohira-kawamura, T. Kikuchi, and K. Kaneko. Retreat from Stress: Rattling in a Planar Coordination. *Adv. Energy Mater.*, 30:1706230, 2018.

[81] M.D. Nielsen, V. Ozolins, and J.P. Heremans. Lone pair electrons minimize lattice thermal conductivity. *Energy Environ. Sci.*, 6(2):570–578, 2013.

[82] Y. Dong, A.R. Khabibullin, Kaya Wei, J.R. Salvador, G.S. Nolas, and L.M. Woods. Bournonite PbCuSbS3: Stereochemically Active Lone-Pair Electrons that Induce Low Thermal Conductivity. *Chem. Phys. Chem.*, 16(15):3264–3270, 2015.

[83] E.J. Skoug and D.T. Morelli. Role of lone-pair electrons in producing minimum thermal conductivity in nitrogen-group chalcogenide compounds. *Phys. Rev. Lett.*, 107(23), 2011.

[84] B. Du, R. Zhang, K. Chen, A. Mahajan, and M.J. Reece. The impact of lone-pair electrons on the lattice thermal conductivity of the thermoelectric compound CuSbS2. *J. Mater. Chem. A*, 5:3249–3259, 2017.

[85] C.W. Li, J. Hong, A.F. May, D. Bansal, S. Chi, T. Hong, G. Ehlers, and O. Delaire. Orbitally driven giant phonon anharmonicity in SnSe. *Nature Phys.*, 11(October):1063–1070, 2015.

[86] B. Du, K. Chen, H. Yan, and M.J. Reece. Efficacy of lone-pair electrons to engender ultralow thermal conductivity. *Scripta Materialia*, 111:49–53, 2016.

[87] J.V. Embden, K. Latham, N.W. Duffy, and Y. Tachibana. Near-Infrared Absorbing Cu12Sb4S13 and Cu3SbS4 Nanocrystals: Synthesis, Characterization, and Photoelectrochemistry. *J. Am. Chem. Soc.*, 135:11562–11571, 2013.

[88] P. Vaqueiro, R.A.R. Al-Orabi, S.D.N. Luu, G. Geulou, A.V. Powell, R.I. Smith, J.P. Song, D. Wee, and M. Fornari. The role of copper in the thermal conductivity of

thermoelectric oxychalcogenides: do lone pairs matter? *Phys. Chem. Chem. Phys.*, 17:31735–31740, 2015.

[89] J. Heo, G. Laurita, S. Muir, M.A. Subramanian, and D.A. Keszler. Enhanced thermoelectric performance of synthetic tetrahedrites. *Chem. Mater.*, 26(6):2047–2051, 2014.

[90] X. Lu, D.T. Morelli, Y. Xia, and V. Ozolins. Increasing the thermoelectric figure of merit of tetrahedrites by co-doping with nickel and zinc. *Chem. Mater.*, 27(2):408–413, 2015.

[91] J. Wang, M. Gu, Y. Bao, X. Li, and L. Chen. Quick Fabrication and Thermoelectric Properties of Cu12Sb4S13 Tetrahedrite. *J. Elec. Mater.*, 45(4):2274–2277, 2016.

[92] D.S.S. Prem-Kumar, R. Chetty, P. Rogl, G. Rogl, E. Bauer, P. Malar, and R.C. Mallik. Thermoelectric properties of Cd doped tetrahedrite: Cu12-xCdxSb4S13. *Intermetallics*, 78:21–29, 2016.

[93] F.H. Sun, C.F. Wu, Z. Li, Y. Pan, Asfandiyar, J. Dong, and J.F. Li. Powder metallurgically synthesized Cu12Sb4S13 tetrahedrites: phase transition and high thermoelectricity. *RSC Advances*, 7(31):18909–18916, 2017.

[94] S. Kim, S. Kwak, Ji. Pi, G. Lee, and I. Kim. Preparation of Tetrahedrite Cu12Sb4S13 by Mechanical Alloying and Hot Pressing. *J. Elec. Mater.*, Unreleased:1–7, 2018.

[95] N.E. Johnson, J.R. Craig, and J.D. Rimstidt. Crystal chemistry of tetrahedrite. *Am. Miner.*, 73(2):389–397, 1988.

[96] K. Tatsuka and N. Morimoto. Composition Variation and Polymorphism of Tetrahedrite in the Cu-Sb-S System below 400C. *Am. Miner.*, 58:425–434, 1973.

[97] K. Tatsuka and N. Morimoto. Tetrahedrite Stability Relations in the Cu-Sb-S System. *Econ. Geol.*, 72:258–270, 1977.

[98] E. Makovicky and B.J. Skinner. Studies of the sulfosalts of copper. VI: Low-temperature exsolution in synthetic tetrahedrite solid solution, Cu12+x+Sb4+yS13. *Can. Miner.*, 16:611–623, 1978.

[99] E. Makovicky and B.J. Skinner. Studies of Sulfosalts of Copper. VII: Crstal structures of exsolution products of Cu12.3Sb4S13 and Cu13.8Sb4S13 of unsubstituted Synthetic Tetrahedrite. *Can. Miner.*, 17, 1979.

[100] Y. Yan, H. Wu, G. Wang, X. Lu, and X. Zhou. High thermoelectric performance balanced by electrical and thermal transport in tetrahedrites Cu12+xSb4S12Se. *Energy Storage Mater.*, 13:127–133, 2018.

[101] N.E. Johnson, J.R. Craig, and J.D. Rimstidt. Compositional trends in tetrahedrite. *Can. Miner.*, 24:385–397, 1986.

[102] J. Heo, R. Ravichandran, C.F. Reidy, J. Tate, J.F. Wager, and D.A. Keszler. Design meets nature: Tetrahedrite solar absorbers. *Adv. Energy Mater.*, 5(7), 2015.

[103] D.I. Nasonova, I.A. Presniakov, Al.. Sobolev, V.Y. Verchenko, A.A. Tsirlin, Zheng Wei, E.V. Dikarev, and A.V. Shevelkov. Role of iron in synthetic tetrahedrites revisited. *J. Solid State Chem.*, 242:62–69, 2016.

[104] A. Guler, C. Boyraz, D. A. Shulgin, G. V. Mozzhukhin, and B. Z. Rameev. Synthesis & characterization of tetrahedrite compounds for thermoelectric applications. *9th Int. Kharkiv Symposium on Physics and Engineering of Microwaves, Millimeter and Submillimeter Waves*, 2016:1–4, 2016.

[105] J.W. Andreasen, E. Makovicky, B. Lebech, and S.K. Moller. The role of iron in tetrahedrite and tennantite determined by Rietveld refinement of neutron powder diffraction data. *Phys. Chem. Miner.*, 35(8):447–454, 2008.

[106] A. Guler, S. Ballikaya, C. Boyraz, C. Okay, D. Shulgin, and B. Rameev. Thermoelectric properties and EPR analysis of Fe doped Cu12Sb4S13. *J. Solid State Chem.*, 269:547–552, 2019.

[107] R. Chetty, A. Bali, M.H. Naik, G. Rogl, P. Rogl, M. Jain, S. Suwas, and R.C. Mallik. Thermoelectric properties of Co substituted synthetic tetrahedrite. *Acta Materialia*, 100:266–274, 2015.

[108] Y. Bouyrie, S. Sassi, C. Candolfi, J.B.S. Vaney, A. Dauscher, and B. Lenoir. Thermoelectric properties of double-substituted tetrahedrites Cu12-xCoxSb4-yTeyS13. *Dalton Trans.*, 45(17):7294–7302, 2016.

[109] T. Barbier, S. Rollin-Martinet, P. Lemoine, F. Gascoin, A. Kaltzoglou, Paz Vaqueiro, A.V. Powell, and E. Guilmeau. Thermoelectric Materials: A New Rapid Synthesis Process for Nontoxic and High-Performance Tetrahedrite Compounds. *J. Am. Ceram. Soc.*, 99(1):51–56, 2015.

[110] T. Barbier, P. Lemoine, S. Martinet, M. Eriksson, M. Gilmas, Eric Hug, Gabin Gú, P. Vaqueiro, A.V. Powell, and E. Guilmeau. Up-scaled synthesis process of sulphur-based thermoelectric materials. *RSC Advances*, 6(12):10044–10053, 2016.

[111] A.P. Goncalves, E.B. Lopes, B. Villeroy, J. Monnier, C. Godart, and B. Lenoir. Effect of Ni, Bi and Se on the tetrahedrite formation. *RSC Advances*, 6:102359–102367, 2016.

[112] Y. Bouyrie, C. Candolfi, J.B. Vaney, A. Dauscher, and B. Lenoir. High Temperature Transport Properties Cu12-xMxSb4-yTeyS13 (M=Zn,Ni) Compounds. *J. Elec. Mater.*, 45(3):1601–1605, 2016.

[113] S. Harish, D. Sivaprahasam, M. Battabyal, and R. Gopalan. Phase stability and thermoelectric properties of Cu10.5Zn1.5Sb4S13 tetrahedrite. *J. Alloys and Compounds*, 667:323–328, 2016.

[114] T. Barbier, Pi. Lemoine, S. Gascoin, O.I. Lebedev, A. Kaltzoglou, Paz Vaqueiro, A.V. Powell, R.I. Smith, and E. Guilmeau. Structural stability of the synthetic thermoelectric ternary and nickel-substituted tetrahedrite phases. *J. Alloys and Compounds*, 634:253–262, 2015.

[115] R.R. Seal, E.J. Essene, and W.C. Kelly. Tetrahedrite and Tennantite: Evaluation of Thermodynamic Data and Phase Equilibria. *Can. Miner.*, 28:725–738, 1990.

[116] F.D. Benedetto, G.P. Bernardini, D. Borrini, C. Emiliani, C. Cipriani, Costanza Danti, A.A. Caneschi, D. Gatteschi, and M. Romanelli. Crystal chemistry of tetrahedrite solid-solution: EPR and magnetic investigations. *Can. Miner.*, 40(3):837–847, 2002.

[117] R.A.D. Pattrick and A.J. Hall. Silver Substitution into Synthetic Zinc, Cadmium, and Iron Tetrahedrites. *Mineralogy Magazine*, 47(345):441–451, 1983.

[118] L.L. Huang, Y.S. Wang, C. Zhu, R. Xu, J.M. Li, J.H. Zhang, D. Li, Z.M. Wang, L. Wang, C.J. Song, H.X. Xin, J. Zhang, and X.Y. Qin. Preparation and enhanced thermoelectric performance of Pb-doped tetrahedrite Cu12-x-xPbxSb4S13. *J. Alloys and Compounds*, 769:478–483, 2018.

[119] X. Lu and D.T. Morelli. The effect of Te substitution for Sb on thermoelectric properties of tetrahedrite. *J. Elec. Mater.*, 43(6):1983–1987, 2014.

[120] Y. Bouyrie, C. Candolfi, A. Dauscher, B. Malaman, and B. Lenoir. Exsolution Process as a Route toward Extremely Low Thermal Conductivity in Cu12Sb4-xTexS13 Tetrahedrites. *Chem. Mater.*, 27(24):8354–8361, 2015.

[121] D.S. Prem-Kumar, R. Chetty, O.E. Femi, K. Chattopadhyay, P. Malar, and R.C. Mallik. Thermoelectric Properties of Bi Doped Tetrahedrite. *J. Elec. Mater.*, 46(5):1–7, 2016.

[122] B.J. Wuensch, Y. Takeuchi, and W. Nowacki. Refinement of the crystal structure of binnite, Cu12As4S13. *Zeitschrift fur Kristallographie - New Crystal Structures*, 123:1–20, 1966.

[123] E. Makovicky, L. Karanovic, D. Poleti, T. Balic-Zunic, and W. H. Paar. Crystal structure of Copper-Rich Unsubstituted Tennantite, Cu12.5As4S13. *Can. Miner.*, 43:679–688, 2005.

[124] S. K. Moller and E. Makovicky. Exploratory studies of element substitutions in synthetic tetrahedrite, Part II: Selenium and tellurium as anions in Zn-Fe tetrahedrites. *Neuses Jahrbuch Fur Mineralogie-Monatshefte*, 385, 1999.

[125] Y. Zhang, D. Morelli, V. Ozolins, and C. Wolverton. Prediction of New Stable Compounds and Promising Thermoelectrics in the Cu-Sb-Se System. *Chem. Mater.*, 26(11):3427–3435, 2014.

[126] X. Lu, D.T. Morelli, Y. Wang, W. Lai, Y. Xia, and V. Ozolins. Phase Stability, Crystal Structure, and Thermoelectric Properties of Cu12Sb4S13-xSex Solid Solutions. *Chem. Mater.*, 28(6):1781–1786, 2016.

[127] S. Tippireddy, R. Chetty, K.K. Raut, M.H. Naik, P. Mukherjee, M. Jain, R.C. Nath, K.T. Wojciechowski, and R.C. Mallik. Electronic and Thermoelectric Properties of Zn and Se Double Substituted Tetrahedrite. *Physical Chemistry Chemical Physics*, In-print, 2018.

[128] A.P. Goncalves, E.B. Lopes, J. Monnier, J. Bourgon, J.B. Vaney, A. Piarristeguy, A. Pradel, B. Lenoir, G. Delaizir, M.F.C. Pereira, E. Alleno, and C. Godart. Fast and scalable preparation of tetrahedrite for thermoelectrics via glass crystallization. *J. Alloys and Compounds*, 664:209–217, 2016.

[129] N. Mozgova, V. Miku, V.I. Valiukenas, A. Tsepin, and A. Orliukas. Some Electrical Properties of Fahlore Cu10(Zn,Fe)2(As,Sb)4S13. *Phys. Chem. Miner.*, 15:171–172, 1987.

[130] P. Levinsky, J. B. Vaney, C. Candolfi, A. Dauscher, B. Lenoir, and J. Hejtmánek. Electrical, Thermal, and Magnetic Characterization of Natural Tetrahedrites-Tennantites of Different Origin. *J. Elec. Mater.*, 45(3):1351–1357, 2016.

[131] M. Telkes. Thermoelectric Power and Electrical Resistivity of Minerals. *Am. Miner.*, 35(7):536–555, 1950.

[132] X. Lu and D.T. Morelli. Natural mineral tetrahedrite as a direct source of thermoelectric materials. *Phys. Chem. Chem. Phys.*, 15(16):5762–5766, 2013.

[133] X. Lu and D.T. Morelli. Rapid synthesis of high-performance thermoelectric materials directly from natural mineral tetrahedrite. *MRS Comm.*, 3(03):129–133, 2013.

[134] X. Fan, E.D. Case, X. Lu, and D.T. Morelli. Room temperature mechanical properties of natural-mineral-based thermoelectrics. *J. Mater. Sci.*, 48(21):7540–7550, 2013.

[135] K. Ramasamy, H. Sims, W.H. Butler, and A. Gupta. Selective nanocrystal synthesis and calculated electronic structure of all four phases of copper-antimony-sulfide. *Chem. Mater.*, 26(9):2891–2899, 2014.

[136] K. Chen, J. Zhou, W. Chen, P. Zhou, F. He, and Y. Liu. Size-Dependent Synthesis of Cu12Sb4S13 Nanocrystals with Bandgap Tunability. *Particle & Particle Systems Characterization*, 2015.

[137] S. Suehiro, K. Horita, M. Yuasa, T. Tanaka, K. Fujita, Y. Ishiwata, K. Shimanoe, and T. Kida. Synthesis of Copper-Antimony-Sulfide Nanocrystals for Solution-Processed Solar Cells. *Inorg. Chem.*, 54(16):7840–7845, 2015.

[138] Y. Wu, X. Qiao, X. Fan, X. Zhang, S. Cui, and J. Wan. Facile synthesis of monodisperse Cu3SbSe4 nanoparticles and thermoelectric performance of Cu3SbSe4 nanoparticle based materials. *J. Nanoparticle Res.*, 17(7):1–7, 2015.

[139] S. Bera, A. Dutta, S. Mutyala, D. Ghosh, and N. Pradhan. Predominated Thermodynamically Controlled Reactions for Suppressing Cross Nucleations in Formation of Multinary Substituted Tetrahedrite Nanocrystals. *J. Phys. Chem. Lett.*, 9:1907–1912, 2018.

[140] D. Chen, Y. Zhao, Y. Chen, T. Lu, Y. Wang, J. Zhou, and Z. Liang. Thermoelectric Enhancement of Ternary Copper Chalcogenide Nanocrystals by Magnetic Nickel Doping. *Adv. Elec. Mater.*, 2(6):2–6, 2016.

[141] D.J. James, X. Lu, D.T. Morelli, and S.L. Brock. Solvothermal Synthesis of Tetrahedrite: Speeding Up the Process of Thermoelectric Material Generation. *ACS Appl. Mater. Inter.*, 7(42):23623–23632, 2015.

[142] C. An, Yi. Jin, K. Tang, and Y. Qian. Selective synthesis and characterization of famatinite nanofibers and tetrahedrite nanoflakes. *J. Mater. Chem.*, 13:301–303, 2003.

[143] B. John, G.G. Silvena, and A.L. Rajesh. Influence of reaction time on the structural, optical and electrical performance of copper antimony sulfide nanoparticles using solvothermal method. *Physica B: Condensed Matters*, 537:243–250, 2018.

[144] T. Rath, A.J. Maclachlan, M.D. Brown, and S.A. Haque. Structural, optical, and charge generation properties of chalcostibite and tetrahedrite copper antimony sulfide thin films prepared from metal xanthates. *J. Mater. Chem. A*, 3:24155–24162, 2015.

[145] V. Stavila, D.B. Robinson, M.A. Hekmaty, R. Nishimoto, D.L. Medlin, S. Zhu, T.M. Tritt, and P.A. Sharma. Wet-Chemical Synthesis and Consolidation of Stoichiometric Bismuth Telluride Nanoparticles for Improving the Thermoelectric Figure-of-Merit. *ACS Appl. Mater. Inter.*, 5(14):6678–6686, 2013.

[146] A. Zevalkink, D.M. Smiadak, J.L. Blackburn, A.J. Ferguson, M.L. Chabinyc, O. Delaire, J. Wang, K. Kovnir, J. Martin, L.T. Schelhas, T.D. Sparks, S.D. Kang, M.T. Dylla, G.J. Snyder, B.R. Ortiz, and E.S. Toberer. A practical field guide to thermoelectrics: Fundamentals, synthesis, and characterization. *Appl. Phys. Rev.*, 5:021303, 2018.

[147] D.P. Weller, D.L. Stevens, G.E. Kunkel, A.M. Ochs, C.F. Holder, D.T. Morelli, and M.E. Anderson. Thermoelectric Performance of Tetrahedrite Synthesized by a Modified Polyol Process. *Chem. Mater.*, 29(4):1656–1664, 2017.

[148] D.P. Weller and D.T. Morelli. Rapid synthesis of zinc and nickel co-doped tetrahedrite thermoelectrics by reactive spark plasma sintering and mechanical alloying. *J. Alloys and Compounds*, 710:794–799, 2017.

[149] O. Guillon, J. Gonzalez-Julian, B. Dargatz, T. Kessel, G. Schierning, J. Rathel, and M. Herrmann. Field-Assisted Sintering Technology/Spark Plasma Sintering: Mechanisms, Materials, and Technology Developments. *Adv. Energy Mater.*, 16(7):830–849, 2014.

[150] D.M. Hulbert, A. Anders, D.V. Dudina, J. Andersson, D. Jiang, C. Unuvar, C. Univar, U. Anselmi-Tamburini, E.J. Lavernia, and A.K. Mukherjee. The absence of plasma in "spark plasma sintering". *J. Appl. Phys.*, 104:033305, 2008.

[151] B.D. Cullity. *Elements of X-ray Diffraction*. Addison-Wesley Publishing Company, Reading, MA, 3rd edition, 1956.

[152] H.S. Kim, Z.M. Gibbs, Y. Tang, H. Wang, and G.J. Snyder. Characterization of Lorenz number with Seebeck coefficient measurement. *APL Materials*, 3(4):041506, 2015.

[153] F. Fievet, S. Ammar-Merah, R. Brayner, F. Chau, M. Giraud, F. Mammeri, J. Peron, J. Y. Piquemal, L. Sicard, and G. Viau. The polyol process: a unique method for easy access to metal nanoparticles with tailored sizes, shapes and compositions. *Chem. Soc. Rev.*, 47(14):5187–5233, 2018.

[154] R. Sk, M.M. Shirolkar, B. Dhara, S. Kulkarni, and A. Deshpande. Enhancing the thermopower and tuning the resistivity in Bi2Se3 with Fe-doping. *Chem. Phys. Lett.*, 638:94–98, 2015.

[155] K. Kaspar, U. Pelz, and H. Hillbrecht. Polyol synthesis of nano-Bi2Te3. *J. Elec. Mater.*, 43(4):1200–1206, 2014.

[156] A. Soni, Z. Yanyuan, Y. Ligen, M.K. Khiam-Aik, M.S. Dresselhaus, and Q. Xiong. Enhanced Thermoelectric Properties of Solution Grown Bi2Te3-xSex Nanoplatelet Composites. *Nano Lett.*, 12:1203–1209, 2012.

[157] M.E. Anderson, S.S.N. Bharadwaya, and R.E. Schaak. Modified polyol synthesis of bulk-scale nanostructured bismuth antimony telluride. *J. Mater. Chem.*, 20(38):8362–8367, 2010.

[158] A. Datta, J. Paul, A. Kar, A. Patra, Z. Sun, L. Chen, J. Martin, and G.S. Nolas. Facile chemical synthesis of nanocrystalline thermoelectric alloys based on Bi-Sb-Te-Se. *Crystal Growth and Design*, 10(9):3983–3989, 2010.

[159] C.F. Holder, E.E. Rugen, and M.E. Anderson. Comparative growth mechanism study for two thermoelectric compounds. *Nanomaterials and Energy*, 3(6):206–214, 2014.

[160] L. Yang, H.H. Hng, J. Ma, T.J. Zhu, and X.B. Zhao. Effects of Co:Sb molar ratio on synthesis and properties of undoped CoSb3prepared via a polyol method. *J. Elec. Mater.*, 39(9):1543–1548, 2010.

[161] A. Gharleghi and C.J. Liu. Rapid fabrication and transport properties of n-type Co4-xNixSb12via modified polyol process synthesis combined with evacuated-and-encapsulated sintering. *J. Alloys and Compounds*, 592:277–282, 2014.

[162] A. Gharleghi, H.Z. Chang, Y.C. Chen, Y.W. Yang, and C.J. Liu. Fabrication and thermoelectric power factor of CoSb3prepared using modified polyol process and evacuated-and-encapsulated sintering. *J. Elec. Mater.*, 42(7):1564–1567, 2013.

[163] L. Yang, H.H. Hng, D. Li, Q.Y. Yan, J. Ma, T.J. Zhu, X.B. Zhao, and H. Huang. Thermoelectric properties of p -type CoSb3 nanocomposites with dispersed CoSb3 nanoparticles. *J. Appl. Phys.*, 106(1):013705, 2009.

[164] D.L. Stevens and M.E. Anderson. *ACS Report (Unpublished).* Undergraduate thesis, Hope College, 2016.

[165] J.P. Heremans, D.M. Thrush, and D.T. Morelli. Thermopower enhancement in lead telluride nanostructures. *Phys. Rev. B*, 70(11), 2004.

[166] P. Vaqueiro, G. Guelou, A. Kaltzoglou, R.I. Smith, T. Barbier, E. Guilmeau, and A.V. Powell. The Influence of Mobile Copper Ions on the Glass-Like Thermal Conductivity of Copper-Rich Tetrahedrites. *Chem. Mater.*, 29(9):4080–4090, 2017.

[167] J.F. Li, W.S. Liu, L.D. Zhao, and M. Zhou. High-performance nanostructured thermoelectric materials. *NPG Asia Mater.*, 2(4), 2010.

[168] J.M.O. Zide, D. Vashaee, Z.X. Bian, G. Zeng, J.E. Bowers, A. Shakouri, and A.C. Gossard. Demonstration of electron filtering to increase the Seebeck coefficient in In0.53Ga0.47As/In0.53Ga0.28Al0.19As superlattices. *Phys. Rev. B*, 74(20):1–5, 2006.

[169] E. Makovicky, K. Forcher, W. Lottermoser, and G. Amthauer. The Role of Fe2+ and Fe3+ in Synthetic Fe-substituted Tetrahedrite. *Mineralogy and Petrology*, 43(1):73–81, 1990.

[170] K. Tatsuka and N. Morimoto. Tetrahedrite stability relations in the Cu-Fe-Sb system. *Am. Miner.*, 62(2):1101–1109, 1977.

[171] J.M. Charnock, C.D. Garner, R.A.D. Pattrick, and D.J. Vaughan. EXAFS and Mossbauer spectroscopic study of Fe-bearing tetrahedrites. *Mineralogy Magazine*, 53:193–199, 1989.

[172] K. Friese, A. Grzechnik, E. Makovicky, T. Balic-Zunic, and S. Karup-Moller. Crystal structures of iron bearing tetrahedrite and tennantite at 25 and 250C by means of Rietveld refinement of synchrotron data. *Phys. Chem. Miner.*, 35(8):455–465, 2008.

[173] D.P. Weller, G.E. Kunkel, A.M. Ochs, D.T. Morelli, and M.E. Anderson. Observation of N-type Behavior in Fe-doped Tetrahedrite at Low Temperature. *Materials Today Physics*, 7:1–6, 2018.

[174] S.N. Guin, J. Pan, A. Bhowmik, D. Sanyal, U.V. Waghmare, and K. Biswas. Temperature dependent reversible p–N–p type conduction switching with colossal change in thermopower of semiconducting AgCuS. *J. Am. Chem. Soc.*, 136:12712–12720, 2014.

[175] V.V. Parfenov and R.A. Nazipov. Effect of Synthesis Temperature on the Transport Properties of Copper Ferrites. *Inorg. Mater.*, 38(1):78–82, 2002.

[176] C. Suryanarayana, E. Ivanov, and V.V. Boldyrev. The science and technology of mechanical alloying. *Mater. Sci. Eng. A*, 304-306:151–158, 2001.

[177] A.A. Al-Joubori and C. Suryanarayana. Synthesis of metastable NiGe2 by mechanical alloying. *Materials and Design*, 87:520–526, 2015.

[178] M.F. Gondim, S.C. Maestrelli, E.C.T. Ramos, J.A.J. Rodrigues, and A.S. Ramos. Synthesis of TaAlO4 compound and Al2O3-TaAlO4 composite ceramic by mechanical alloying and their sintering. *Ceram. Int.*, 41(2):2260–2265, 2015.

[179] D.S. Prem-Kumar, M. Ren, T. Osipowicz, R.C. Mallik, and P. Malar. Tetrahedrite (Cu12Sb4S13) thin films for photovoltaic and thermoelectric applications. *Solar Energy*, 174:422–430, 2018.

[180] A.V. Sobolev, I.A. Presniakov, D.I. Nasonova, V.Y. Verchenko, and A.V. Shevelkov. Thermally Activated Electron Exchange in Cu12-xFexSb4S13(x=1.3,1.5) Tetrahedrites: A Mössbauer Study. *J. Phys. Chem. C*, 121(8):4548–4557, 2017.

[181] N.F. Mott. Conduction in non-crystalline systems. *Phil. Mag.*, 17(150):1259–1268, 1968.

[182] R. Orrù and G. Cao. Comparison of reactive and non-reactive spark plasma sintering routes for the fabrication of monolithic and composite Ultra High Temperature Ceramics (UHTC) materials. *Materials*, 6(5):1566–1583, 2013.

[183] F.C. Sahin, H.E. Kanbur, and B. Apak. Preparation of AlON ceramics via reactive spark plasma sintering. *J. Eur. Ceram. Soc.*, 32(4):925–929, 2012.

[184] A.M. Locci, R. Licheri, R. Orrù, and G. Cao. Reactive Spark Plasma Sintering of rhenium diboride. *Ceram. Int.*, 35(1):397–400, 2009.

[185] N.S. Karthiselva, B.S. Murty, and S.R. Bakshi. Low temperature synthesis of dense TiB2 compacts by reaction spark plasma sintering. *Int. J. Refractory Metals and Hard Mater.*, 48:201–210, 2015.

[186] S.K. Sun, G.J. Zhang, W.W. Wu, J.X. Liu, T. Suzuki, and Y. Sakka. Reactive spark plasma sintering of ZrC and HfC ceramics with fine microstructures. *Scripta Materialia*, 69(2):139–142, 2013.

[187] W.W. Wu, G.J. Zhang, Y.M. Kan, P.L. Wang, K. Vanmeensel, J. Vleugels, and O. VanDerBiest. Synthesis and microstructural features of ZrB2-SiC-based composites by reactive spark plasma sintering and reactive hot pressing. *Scripta Materialia*, 57(4):317–320, 2007.

[188] L. Wang, W. Jiang, L. Chen, and S. Bai. Rapid Reactive Synthesis and Sintering of Submicron TiC/SiC Composites through Spark Plasma Sintering. *J. Am. Ceram. Soc.*, 87(6):1157–1160, 2004.

[189] Y. Zhao, L.J. Wang, G.J. Zhang, W. Jiang, and L.D. Chen. Preparation and microstructure of a ZrB2-SiC composite fabricated by the spark plasma sintering-reactive synthesis (SPS-RS) method. *J. Am. Ceram. Soc.*, 90(12):4040–4042, 2007.

[190] S. Battiston, C. Fanciulli, S. Fiameni, A. Famengo, S. Fasolin, and M. Fabrizio. One step synthesis and sintering of Ni and Zn substituted tetrahedrite as thermoelectric material. *J. Alloys and Compounds*, 702:75–83, 2017.

[191] M. Jacoby. Thermoelectrics Rise Again. *Chem. Eng. News*, 93(19):29–31, 2015.

[192] X. Lu. *Thermoelectric Properties of Natural Mineral Based Tetrahedrite Compounds*. Doctoral thesis, Michigan State University, 2014.

[193] L.L. Huang, J. Zhang, Z.M. Wang, X.G. Zhu, J.M. Li, C. Zhu, D. Li, and C.J. Song. High thermoelectric performance of tetrahedrites through InSb inclusion. *Materialia*, In-print, 2018.

[194] J. Nuss, U. Wedig, W. Xie, P. Yordanov, J. Bruin, R. Hubnert, A. Widenkaff, and H. Takagi. Phosphide-Tetrahedrite Ag6Ge10P12: Thermoelectric Performance of a Long-Forgotten Silver-Cluster Compound. *Chem. Mater.*, 29(16):6956–6965, 2017.

[195] H. Liu, X. Shi, F. Xu, L. Zhang, W. Zhang, L. Chen, Q. Li, C. Uher, T. Day, and G.J. Snyder. Copper ion liquid-like thermoelectrics. *Nature Mater.*, 11(5):422–425, 2012.

[196] G. Dennler, R. Chmielowski, S. Jacob, F. Capet, P. Roussel, S. Zastrow, K. Nielsch, I. Opahle, and G.K.H. Madsen. Are binary copper sulfides/selenides really new and promising thermoelectric materials? *Adv. Energy Mater.*, 4(9):1–12, 2014.

[197] D.R. Brown, T. Day, T. Caillat, and G.J. Snyder. Chemical Stability of (Ag,Cu)2Se: A historical overview. *J. Elec. Mater.*, 42(7):2014–2019, 2013.

[198] T.P. Bailey, S. Hui, H. Xie, A. Olvera, P.F.P. Poudeu, X. Tang, and C. Uher. Enhanced ZT and attempts to chemically stabilize Cu2Se via Sn doping. *J. Mater. Chem. A*, 4:17225–17235, 2016.

[199] K.S. Weldert, W.G. Zeier, T.W. Day, M. Panthofert, G.J. Snyder, and W. Tremel. Thermoelectric Transport in Cu7PSe6 with High Copper Ionic Mobility. *J. Am. Chem. Soc.*, 136(64):12035–12040, 2014.

[200] D.W. Bullett. Applications of atomic-oribtal methods to the structure and properties of complex transtion-metal compounds. *Phys. Chem. Miner.*, 14(6):485–491, 1987.

[201] P. Lemoine, C. Bourges, T. Barbier, V. Nassif, S. Cordier, and E. Guilmeau. High temperature neutron powder diffraction study of the Cu12Sb4S13 and Cu4Sn7S16 phases. *J. Solid State Chem.*, 247:83–89, 2017.

[202] A.P. Goncalves, E.B. Lopes, M.F. Montemor, J. Monnier, and B. Lenoir. Oxidation Studies of Cu12Sb3.9Bi0.1S10Se3 Tetrahedrite. *J. Elec. Mater.*, 47(5):2880–2889, 2018.